

# On the Interactions of Ions and Odor Molecules with Nanomaterials in Water and Synthetic Urine

Isabelle Simonsson

Supervised by Dr. Zareen Abbas



UNIVERSITY OF  
GOTHENBURG

A Thesis Presented for the Degree of Doctor of Philosophy

DEPARTMENT OF CHEMISTRY AND MOLECULAR  
BIOLOGY

---

# On the Interactions of Ions and Odor Molecules with Nanomaterials in Water and Synthetic Urine

Isabelle Simonsson

©Isabelle Simonsson

ISBN: 978-91-8009-917-2 (TRYCK)

ISBN: 978-91-8009-918-9 (PDF)

Department of Chemistry and Molecular Biology  
University of Gothenburg  
SE-412 96 Göteborg  
Sweden  
Telephone: +46(0)31-786 00 00

Printed by Stema Specialtryck AB, Box 969, 501 10 Borås

---

*Reality exists in the human mind, and nowhere else.*

George Orwell

# List of Papers

- Paper I: The specific co-ion effect on gelling and surface charging of silica nanoparticles: Speculation or reality?  
Isabelle Simonsson, Christian Sögaard, Mark Rambaran, Zareen Abbas
- Paper II: Experimental investigations into the irregular synthesis of iron(III) terephthalate metal-organic frameworks MOF-235 and MIL-101  
Isabelle Simonsson, Philip Gärdhagen, Moira Andrén, Pui Lam Tam, Zareen Abbas
- Paper III: TiO<sub>2</sub>/AC composites for the adsorption of p-cresol in synthetic urine  
Isabelle Simonsson, Zareen Abbas
- Paper IV: Specific counter-ion effects and the surface charge behavior of sulfate-functionalized cellulose nanocrystals  
Isabelle Simonsson, Amit Sonker, Zareen Abbas, Gunnar Westman
- Paper V: Interactions of ions and odor molecules with graphene-based nanostructures in synthetic urine: A molecular dynamics exploration  
Prasad Rama, Isabelle Simonsson, Zareen Abbas

# Contribution Report

- Paper I: I wrote the first draft of the manuscript, contributed to the experimental planning, and performed the potentiometric titrations.
- Paper II: I wrote the manuscript and performed most of the experiments.
- Paper III: I wrote the manuscript and planned and performed all experiments.
- Paper IV: I performed the titrations, contributed to the experimental planning, and wrote part of the manuscript.
- Paper V: I contributed to the experimental planning and performed the adsorption experiments, ICP analyses, and participated in the analysis and discussions of the results.

# Abstract

Towards the quest of finding materials to be used as adsorbents in real systems, it is crucial to understand the underlying adsorption processes fully. In many applications, adsorption occurs in biological fluids containing a vast range of ions, organic molecules, and biomolecules. Therefore, performing adsorption experiments in ultrapure water, as is the custom in most studies, does not accurately represent the adsorbent-adsorbate interactions.

The main aim of thesis work is to investigate what adsorbent properties are relevant for the adsorption of odor molecules in urine. The model system contains the environmentally and economically friendly porous material activated carbon, whose surface can be readily modified with acid and metal alkoxides to provide new material properties. As the adsorbate, p-cresol is used, a common odor molecule in urine. Synthetic urine, containing the most prevalent ions and molecules in urine and with a constant pH of 6.0, is used as the solvent.

Further steps were taken to investigate the behavior of ions and surfaces in the aqueous environment by studying specific ion effects on silica nanoparticles and crystalline nanocellulose through extensive experimental work. In addition, a molecular dynamics study of the adsorption of p-cresol on graphene and graphene oxide sheets in synthetic urine was performed to provide more information on the relevant interactions on an atomistic scale.

Our results clearly show that ions have a profound effect on both the properties of the adsorbent and the adsorption behavior in synthetic urine. Counter-ions adsorb at the surface of the negatively charged materials to a varying degree according to the extent of their hydration layer, with the trend following the direct Hofmeister series of cations. Although this effect is well-known for the silica surface, we also showed the same type of behavior on crystalline nanocellulose. However, at alkaline pH, the trend was reversed and the  $\text{Li}^+$  adsorbs more strongly to the surface than the less hydrated cations. We also proved that, for the negative silica surface, there is a significant co-ion effect on the surface charge and gelation rate of the nanoparticles. This was attributed to the formation of ion pairs in water, and this effect appears to be enhanced near charged interfaces.

For the adsorption of p-cresol, we used principal component analysis, a type of

---

multivariate statistics, to derive information on the optimal adsorbent properties. The analyses revealed that a large surface area and a hydrophobic surface are beneficial for p-cresol adsorption in both water and synthetic urine. Surprisingly, the adsorption of p-cresol was enhanced in synthetic urine for the most hydrophobic activated carbon, a result of the salting out effect, which decreases the solubility of organic molecules in the presence of strongly hydrated ions ("structure makers"). The synthetic urine contains sodium, magnesium, calcium, and urea, all considered highly hydrated and, therefore, structure making.

Metal-organic frameworks (MOFs) are a group of highly porous materials formed from metal ions and linker molecules forming extensive networks. Their large surface area makes them promising contenders as adsorbents, which is why we chose two of the more economically and environmentally friendly specimens to use for odor capture. The solvothermal synthesis route is the most common way to synthesize MOFs. Two of the most studied examples are MOF-235(Fe) and MIL-101(Fe), both consisting of Fe(III) ions and terephthalic acid linkers. Despite being synthesized in different solvent compositions and temperatures, the formation of both phases in the same product has frequently been observed in the literature. By testing various combinations of synthesis conditions, i.e., reagent ratios, solvent ratios, equilibration times, and vessel types, we discovered that MOF-235 formation is promoted with larger DMF:ethanol solvent ratios. The product with the largest surface area ( $\approx 3300 \text{ m}^2/\text{g}$ ), containing MIL-101, was obtained in the so-called *ex-situ* synthesis using a larger reagent volume (150 mL) in a regular glass bottle. It was believed that the pressure release and cool down during the sampling changed the reagent environment so that no MOF-235 could be formed.

# Abstract in Swedish

Mot sökandet av att hitta och utveckla nya material att använda inom luktadsorption i verkliga system behöver vi kunna förstå hur adsorptionsprocessen fungerar. I många tillämpningar vill vi använda adsorption i biologiska vätskor som innehåller en blandning av joner, organiska molekyler, och biomolekyler. Att genomföra adsorptionsexperiment i rent vatten, som man gör i majoriteten av alla publicerade studier, ger inte en exakt bild av interaktionerna mellan adsorbent och adsorbat.

Huvudmålet med det här projektet var att undersöka vilka materialegenskaper som är viktiga för att ta upp lukt-molekyler i urin. Ett modellsystem bestående av aktivt kol, ett ekonomiskt och miljövänligt material som med lätthet kan funktionaliseras med hjälp av syra och metallalkoxider, användes. p-Kresol, en vanlig lukt-molekyl i urin, utvaldes till adsorbat. Som lösningsmedel användes syntetiskt urin med ett konstant pH på 6.0, innehållandes de vanligaste jonerna och molekylerna i riktigt urin.

För att djupare undersöka hur joner och ytor beter sig i vattenlösning, utfördes omfattande experiment på hur silikananopartiklar och kristallin nanocellulosa påverkas av jonspecifika effekter. Som ett komplement till våra resultat, utfördes molekyldynamiska simuleringar på adsorptionen av p-kresol på ytor av grafen och grafenoxid i syntetiskt urin. Detta gjordes med förhoppningen att studera adsorptionen på en atomär skala.

Våra resultat påvisar att det finns en direkt effekt av närvaron av joner på adsorbenters egenskaper och adsorptionsprocesser i syntetiskt urin. Motjoner adsorberar på laddade ytor med olika affinitet enligt deras hydratiseringsgrad, vilket följer den direkta Hofmeisterserien för katjoner. Detta är känt sedan innan för silikaytor, men vi kunde även visa att samma fenomen sker för kristallin nanocellulosa. Dessutom påvisade vi att, för den negativa silikaytan, det finns en betydelsefull medjonseffekt som påverkar ytladdningen och gelningstiden på nanopartiklar av silika. Detta kunde härledas för bildandet av jonpar i vatten, en effekt som verkar förstärkas nära laddade ytor.

För adsorptionen av p-kresol användes principalkomponentanalys, en typ av multivariat statistik, för att härleda information över vilka materialegenskaper som är optimala. Analyserna visade att en stor ytarea och hydrofob yta är viktigt för ad-

---

sorptionen av p-kresol i vatten och syntetiskt urin. Något överraskande, visade det sig att p-kresol adsorberades mer i syntetiskt urin på det mest hydrofoba aktiva kolet. Detta är ett resultat av utsaltningseffekten, som sänker lösligheten av organiska molekyler i närvaro av strukturfrämjande joner. Det syntetiska urinet innehåller natrium, magnesium, kalcium, och urea, som alla anses vara starkt hydratiserade och därmed strukturfrämjande.

Metallorganiska strukturer är en grupp av extremt porösa material bestående av metalljoner och länkande molekyler som bildar stora nätverk. Deras höga ytarea gör att de anses vara lovande material inom adsorption. De kan syntetiseras på olika sätt, men den solvotermiska metoden är absolut vanligast. Två av de mest studerade metallorganiska strukturerna är MOF-235(Fe) och MIL-101(Fe), som båda innehåller Fe(III)-joner och tereftalsyra som länkande molekyl. Trots att de vanligtvis syntetiseras i helt olika temperaturer och lösningsmedel kan man i litteraturen observera att båda faserna bildas i många synteser. Genom att testa olika kombinationer av lösningsmedelsammansättningar, reagentproportioner, jämviktstider, och synteskärl, kunde vi uppdaga att bildning av MOF-235 främjas av större DMF:etanolkvoter i lösningsmedlet. Produkten med störst ytarea ( $\approx 3300 \text{ m}^2/\text{g}$ ) innehållandes MIL-101 erhöles i den så-kallade *ex-situ*-syntesen, där vi använde en större reaktionsvolym (150 mL) i en standardglasflaska. Vår hypotes är att tryckutjämningen och nedkylningen som skedde när vi tog ut provlösningar för analys ändrade miljön i reagenslösningen så att MOF-235 inte kunde bildas.

# Abbreviations

2SIP	Solvent-separated ion-pair
AC	Activated carbon
ACF	Activated carbon fiber
BET	Brunauer-Emmer-Teller
BJH	Barrett-Joyner-Halenda
CCC	Critical coagulation concentration
CIP	Common interception point OR contact ion-pair
CN	Coordination number
CNC	Crystalline nanocellulose
DLA	Diffusion-limited aggregation
DLVO	Derjaguin-Landau-Verwey-Overbeek
DMA	Dimethylamine
DMF	N,N-Dimethylformamide
EDL	Electric double layer
EDX/EDS	Energy-dispersive X-ray spectroscopy
EtOH	Ethanol
GO	Graphene oxide
ICP-OES	Inductively coupled plasma optical emission spectroscopy
IEP	Isoelectric point
MAXS	Middle-angle X-ray scattering
MCC	Microcrystalline cellulose
MB	Methylene blue
MC	Monte-Carlo
MD	Molecular dynamics
MO	Methyl orange
MOF	Metal-organic framework
MQ	Milli-Q water
PCA	Principal component analysis
PZC	Point of zero charge
RDF	Radial distribution function
RLA	Reaction-limited aggregation

---

SA	Surface area
SCD	Surface charge density
SCNC	Sulfate-functionalized crystalline nanocellulose
SEM	Scanning electron microscopy
SIP	Solvent-shared ion-pair
SSA	Specific surface area
SU	Synthetic urine
TGA	Thermogravimetric analysis
TLM	Triple layer model
TPA	Terephthalic acid
TTIP	Titanium(IV) tetraisopropoxide
UV-Vis	Ultraviolet-visible
vdW	van der Waals
XPS	X-ray photoelectron spectroscopy
XRD	X-ray diffraction
XRF	X-ray fluorescence
ZIF	Zeolitic imidazolate framework
ZP	Zeta potential

# Mathematical Expressions

$a$	Particle radius
$e$	Electron charge = $1.602176634 \cdot 10^{-19}$ coulomb
$c_m$	Mass concentration
$\eta$	Dynamic viscosity
$E_x$	Electric field strength
$\epsilon$	Permittivity
$F$	Faraday constant = $96\,485$ s A mol <sup>-1</sup>
$G$	Gibbs free energy
$\Gamma$	Surface excess
$\gamma_{\pm}$	Mean ion activity coefficient
$H$	Enthalpy
$I$	Ionic strength
$\kappa$	Debye length
$K_F$	Freundlich constant
$K_L$	Langmuir constant
$M$	Molar concentration
$\mu$	Viscosity
MW	Molar weight
$\nu$	Frequency
$N_A$	Avogadro's constant = $6.0221408 \cdot 10^{23}$ mol <sup>-1</sup>
$\Psi$	Surface potential
$R$	Gas constant = $8.3144626$ J K <sup>-1</sup> mol <sup>-1</sup>
$S$	Entropy
$T$	Temperature
$u_E$	Electrophoretic mobility
$V_P$	Particle velocity
wt%	Weight %
$Z_{ib}$	Effective solvation number

# Contents

<b>1</b>	<b>Introduction</b>	<b>1</b>
<b>2</b>	<b>Background</b>	<b>3</b>
2.1	The physical chemistry of surfaces . . . . .	3
2.2	Solution chemistry . . . . .	11
2.2.1	Ion hydration . . . . .	11
2.2.2	Ion pairing and activity coefficients . . . . .	12
2.3	Adsorption theory . . . . .	13
2.3.1	Aqueous phase adsorption. . . . .	14
2.4	Nanomaterials . . . . .	17
2.4.1	Activated carbon . . . . .	17
2.4.2	TiO <sub>2</sub> /AC composites . . . . .	18
2.4.3	Metal-organic frameworks. . . . .	19
2.4.4	Functionalized nanocellulose . . . . .	22
2.5	Odor molecules . . . . .	23
2.5.1	p-Cresol . . . . .	23
2.6	Synthetic urine . . . . .	24
<b>3</b>	<b>Experimental Methods</b>	<b>26</b>
3.1	Chemicals and instruments . . . . .	26
3.2	Potentiometric titrations . . . . .	27
3.3	Gel-time determinations . . . . .	28
3.4	Nanomaterials synthesis . . . . .	29
3.4.1	MOF-235(Fe) and MIL-101(Fe) . . . . .	29
3.4.2	Activated carbon . . . . .	34
3.5	Characterization methods . . . . .	35
3.5.1	Nitrogen adsorption . . . . .	35
3.5.2	X-ray diffraction . . . . .	36
3.5.3	X-ray fluorescence . . . . .	37
3.5.4	X-ray photoelectron spectroscopy . . . . .	37
3.5.5	Zeta potential . . . . .	38

---

3.5.6	Inductively coupled plasma spectroscopy . . . . .	40
3.6	Adsorption experiments . . . . .	41
3.6.1	p-Cresol adsorption . . . . .	41
3.6.2	Ion adsorption in synthetic urine . . . . .	41
3.7	Principal component analysis . . . . .	43
3.8	Molecular dynamics . . . . .	43
<b>4</b>	<b>Summary of Papers</b>	<b>45</b>
4.1	Paper I: The co-ion effect on the surface charge and gelling of silica nanoparticles . . . . .	46
4.2	Paper II: Fe(III) TPA MOF synthesis . . . . .	49
4.3	Paper III: p-Cresol adsorption on TiO <sub>2</sub> /AC composites . . . . .	54
4.3.1	Material characterization . . . . .	54
4.3.2	p-Cresol adsorption . . . . .	61
4.4	Paper IV: Surface characterization of SCNC . . . . .	65
4.5	Paper V: <i>In-silico</i> studies on p-cresol adsorption in synthetic urine . .	71
4.5.1	ICP-OES ion adsorption study . . . . .	75
<b>5</b>	<b>Concluding Discussion and Outlook</b>	<b>76</b>
5.1	Ion interactions . . . . .	77
5.2	Odor capture in synthetic urine . . . . .	79
5.3	The iron(III) TPA MOF synthesis enigma . . . . .	81

# Chapter 1

## Introduction

The field of interface science covers the physicochemical properties and behavior at the boundary between two phases. It is an integral part of a vast range of research topics, such as adsorption, catalysis, electrochemistry, biochemistry, and geochemistry. It is an extensively studied field and covers the chemistry of colloids, metals, semiconductors, micelles and surfactants, cells and proteins, soils and minerals, aerosols, and more.

Adsorption involves the attachment of chemical species (adsorbates) at an interface (adsorbent), often solid-liquid or solid-air. The theory of adsorption of ions and molecules on solid surfaces in the aqueous phase has not yet been fully elucidated. It is a complex process since not only the adsorbate-adsorbent interactions have to be taken into account, but also the interactions between adsorbate, ions, water molecules, and the surface. In addition, the properties of the double layer located at the solid-liquid interface depend not only on the type of surface material but also on the presence of adsorbate ions and molecules. These can be specifically adsorbed at the interface due to net attractive potentials originating from forces such as van der Waals, electrostatic, and hydrophobic interactions.

The development of large surface area materials has spurred the research related to adsorption, and its possible field of use has increased significantly. Examples of these kinds of materials include nanoparticles, activated carbon (AC), zeolites, and metal-organic frameworks (MOFs). The three latter examples have large surface areas due to their porous structures. Other surface properties relevant for effective adsorption are hydrophobicity/hydrophilicity, the presence of chemical groups, and surface charge. The behavior of the double layer in porous materials is not easily predicted, as the curvature of the pores affects the local distribution of charge. This gives us a further incentive to study the adsorption behavior of porous materials in aqueous suspension.

One potential field of application for adsorption is odor capture; most odorants have high vapor pressures and low odor thresholds, making them especially difficult

---

to separate. Effective odor capture could improve the living standards of hundreds of millions of people with urinary incontinence worldwide. Both urine itself and used incontinence products are known to emit foul-smelling odorants [1]. Besides being effective at adsorbing odor molecules, a material used in disposable hygiene products must be cheap, chemically stable, non-toxic, and environmentally friendly.

The focus of this thesis work is to investigate what is happening at and around the surface of a solid particle suspended in aqueous media in the presence of various ions and molecules. Specifically, this work investigates the impact of different material properties on the adsorption of the organic odor molecule p-cresol, as well as the effect of ions on the surface charge of silica nanoparticles and nanocellulose suspended in aqueous electrolytes. The hope is to provide further insight into the adsorption process in water and biological fluids for developing materials to be used in industries such as hygiene and food.

# Chapter 2

## Background

This section covers the theory behind the experimental and theoretical results obtained in this Ph.D. project, more specifically, the fundamentals of surface chemistry and adsorption, ionic effects on surfaces in solution, and common odor molecules in urine. A section regarding the concept of ion pairing is included, as it has been recently theorized to have an indirect influence on the electrostatic charging of surfaces in aqueous electrolytes. The topic of ion hydration is grazed upon to explain the ion-specific effects observed for the materials in this study. There is also a section on the different materials studied in this project, explaining their chemical and physical properties and some of their applications.

### 2.1 The physical chemistry of surfaces

Irving Langmuir wrote in his paper [2] from 1918:

*In the surface layer, because of the asymmetry of the conditions, the arrangement of the atoms must always be slightly different from that in the interior. These atoms will be unsaturated chemically and thus they are surrounded by an intense field of force.*

In other words, when a solid, such as a particle, is dispersed in a medium, the interface between the solid and the liquid carries different properties than the two bulk phases. For colloidal systems, perhaps the most important effect of this is the development of charge separation at interfaces, forming an electric double layer (EDL), which contributes to electrostatic stability as well as to the potentially impactful physicochemical properties of nanoparticles.

The charge developed at an interface between two phases could occur due to several reasons [3]. If the two phases have different electron or ion affinities, this creates an imbalance in the electron/ion distributions. The ionization of surface groups is another cause of charge separation, which is common for metal oxides in

protic solvents (e.g., water). An example is the silica-aqueous solution interface, containing amphoteric silanol groups:  $-\text{Si}-\text{OH}_2^+ \leftrightarrow -\text{Si}-\text{OH} \leftrightarrow -\text{Si}-\text{O}^-$ . One of the phases could also contain immobile charged groups, like montmorillonite's negatively charged sheets.

### The electric double layer

In order to neutralize the surface charge developed at a solid-liquid interface, counter-ions (ions with the opposite charge as the surface) in the solution accumulate close to the surface. This layer, together with the diffuse layer, which contains both counter- and co-ions (ions with the same charge as the surface), forms the electric double layer. The EDL can be modelled in several different ways; examples include the Helmholtz double layer, the Gouy-Chapman double layer, and the triple layer model (TLM, see Figure 2.1) [4]. The TLM model includes protons ( $\text{H}^+$ ) adsorbed adjacent to the surface in the inner Helmholtz plane (also called the Stern layer), and counter-ions are adsorbed in the outer Helmholtz plane. Both counter-ions and co-ions are located in the diffuse layer, where the potential ( $\psi$ ) eventually drops to 0. The double layer thickness ( $\kappa^{-1}$ ), also called the Debye length and the electrostatic screening distance, is a characteristic of the electrolyte and depends on temperature (T), the permittivity of the liquid medium ( $\epsilon$ ), and ionic strength (I). For the calculation of  $\kappa$ , see Equation 2.1, where  $N_A$  is Avogadro's constant, R is the gas constant,  $\epsilon_0$  is the vacuum permittivity, and e is the elementary charge. As expected, at a higher salt content,  $\kappa$  is increased, meaning that the Debye screening length is decreased due to more counter-ions accumulating near the surface.

$$\kappa = \sqrt{\frac{2000e^2N_A^2I}{\epsilon\epsilon_0RT}} \quad (2.1)$$

### Interactions between colloids

Charged particles in solution (colloids) experience forces from each other. Repulsive forces, such as electrostatic repulsion between like-charged particles contribute to a major part of the stability of colloids. Attractive forces include van der Waals (vdW) forces, calculated by Equation 2.3, where A denotes the Hamaker constant and a equals the particle radius. The Hamaker constant is a material property, and the effective Hamaker constant includes both the particles' constants and the suspending medium's constant. According to the DLVO (Derjaguin-Landau-Verwey-Overbeek) theory, which was established in the 1930s and the 1940s, the net potential ( $\phi_{\text{net}}$ ) between two surfaces is calculated by adding the attractive potential ( $\phi_A$ ) and the repulsive potential ( $\phi_R$ ), both as a function of distance (D) between the surfaces:

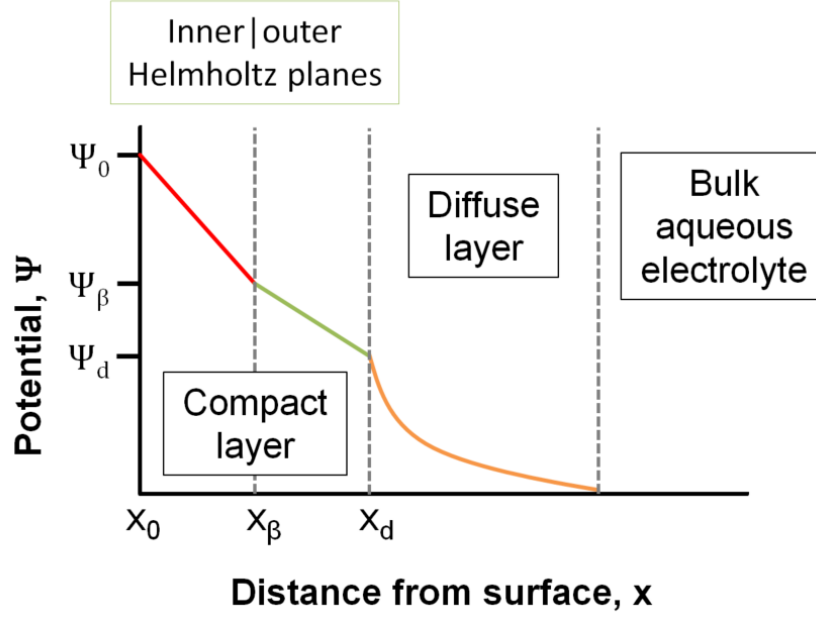


**Figure 2.1:** The triple layer model showing how the potential changes with distance from the surface. Protons are adsorbed at the 0-plane, while the larger counter-ions adsorb at the  $\beta$ -plane (and the d-plane to some extent).

$$\phi_{\text{net}} = \phi_A + \phi_R \quad (2.2)$$

$$\phi_A = \phi_{\text{vdW}} = -\frac{Aa}{12D} \quad (2.3)$$

$$\phi_R = \frac{64\pi n_\infty k_B T \gamma_\delta^2}{\kappa^2} \exp(-\kappa D) \quad (2.4)$$

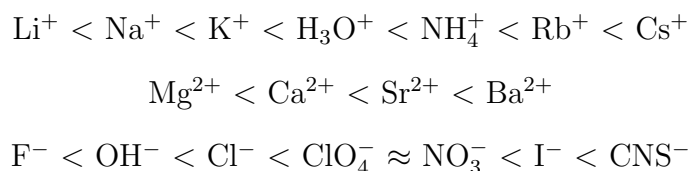
When plotting  $\phi_{\text{net}}$  against the distance between two particles, a curve containing two local minima and one local maximum will be formed (see Figure 2.2). The primary minimum has a deep potential well and constitutes irreversible aggregation, while the secondary is significantly more shallow and represents reversible aggregation (flocculation) between the particles. A potential energy barrier is created due to the repulsive electrostatic forces, see eq. 2.4;  $n_\infty$  equals the bulk ion concentration,  $k_B$  equals the Boltzmann constant,  $T$  is the temperature in Kelvin degrees,  $\gamma_\delta$  equals  $\tanh(ze\psi_\delta/4k_B T)$ , where  $\psi_\delta$  is the Stern potential. Brownian motion ( $\approx k_B T$ ) by the particles provides the energy to overcome this barrier. The energy required for rapid and irreversible aggregation is commonly a few multiples of  $k_B T$  [4].

Analysing Equation 2.4, the larger  $\kappa$  is, the smaller the electrostatic repulsion potential energy will be. Since  $\kappa$  is proportional to the ionic strength of the medium that the particles are suspended in, a higher salt concentration will decrease the energy required for irreversible aggregation to take place. This explains the phe-

nomenon of surface charge screening by counter-ions at the inner Helmholtz plane. The salt concentration required to overcome the potential energy barrier is called the critical coagulation concentration (CCC) and can be determined experimentally. Since it is the counter-ion that shields the electrostatic repulsion energy, the CCC depends on its valency; i.e., for a negatively charged particle, the CCC is smaller for a divalent salt (e.g.,  $\text{CaCl}_2$ ) than a monovalent (e.g.,  $\text{NaCl}$ ) [4].

### Ion-specific effects

Besides valency, another counter-ion property affecting the CCC is its extent of surface hydration. In the 19th century, Franz Hofmeister discovered that the ability of a salt to salt out (coagulate) egg white protein depends on its ion composition [5]. This led to the foundation of the Hofmeister series presented below. Later on, it was found that this theory also could be applied to other systems, such as charged particles.



Direct series:

More chaotropic  $\rightarrow$

Smaller hydration shell  $\rightarrow$

Closer adsorption  $\rightarrow$

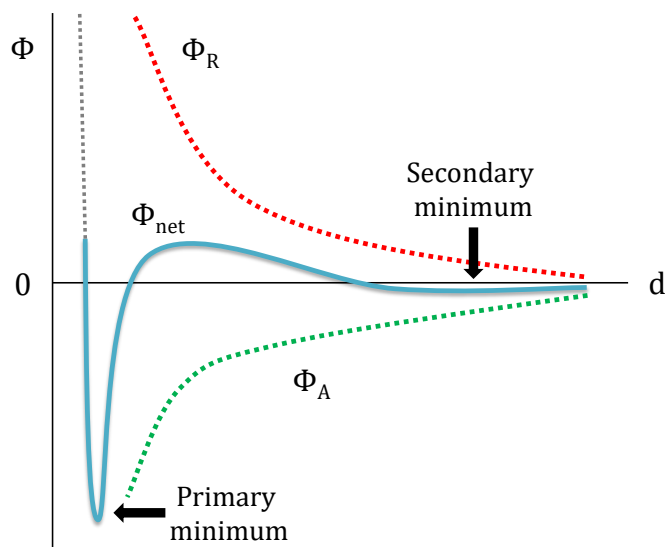


**Figure 2.2:** Schematic graph showing how the net potential between two surfaces ( $\phi_{\text{net}}$ , blue solid line) depends on the separation distance ( $d$ ). Repulsive ( $\phi_{\text{R}}$ ) and attractive ( $\phi_{\text{A}}$ ) potentials are shown as dotted lines in the plot.

Depending on the surface type, a counter-ion's tendency to adsorb and, consequently, screen the surface charge follows either the direct or the indirect Hofmeister series. For example, the behavior of the negatively charged silica surface follows the direct series; a chaotropic (water-disturbing) cation such as  $K^+$  disrupts the ordered water structure at the silica surface and readily induces aggregation. The size of an ion's hydration shell is inversely proportional to its crystallographic radius. The highly kosmotropic (water-stabilizing) ion  $Li^+$ , with a crystallographic radius of 0.069 nm, has an estimated hydrated radius of 0.210 nm [6] - an increase by over 200%!

The effect of the counter-ion has been widely studied for many different surfaces, but so far, little attention has been given to the effect of the co-ion. An example where the co-ion directly affects the surface charge of metal oxides is in concentrated electrolytes with strong specific adsorption of counter-ions. In this case, "over-charging" occurs, where an excess of counter-ions accumulates at the surface, reversing the sign of the surface charge. Suddenly, the former co-ions become new counter-ions and dictate the surface potential [7]. However, there has been little evidence of any co-ion effect in dilute salt solutions until recently.

### Potentiometric titrations

Due to the difficulty in directly measuring the potential at a surface ( $\phi_0$ ), techniques have been developed to obtain other quantitative values related to a surface's charge. By titrating a colloidal suspension with acid and/or base while monitoring the change in pH of the solution, the surface charge density (SCD, unit: Coulomb/m<sup>2</sup>, 1 Coulomb =  $6.242 \times 10^{18}$  electron charge) of the particles can be obtained (see Figure 2.3). Some of the conditions of the colloidal system are that the particle surface should contain amphoteric groups and that the total surface area is large enough to detect the loss/gain of protons ( $H^+$ ) in the bulk.

The calculation of SCDs from potentiometric titrations involves determining the amount of protons that have been taken up or released from the amphoteric surface groups (in the inner Helmholtz layer, see Figure 2.1) of the particles upon a change in pH. In practice, a known amount of  $H^+$  or  $OH^-$  is added to the system, and a pH electrode measures the pH after equilibrium has been reached. The difference between the "expected", determined from blank titrations, and the measured proton concentration yields the SCD of the colloids as a function of pH [8], see Equation 2.5.

$$SCD = \frac{F}{s C_m} \left[ \left( [H^+]_{dispersion} - [H^+]_{blank} \right) - \left( [OH^-]_{dispersion} - [OH^-]_{blank} \right) \right] \quad (2.5)$$

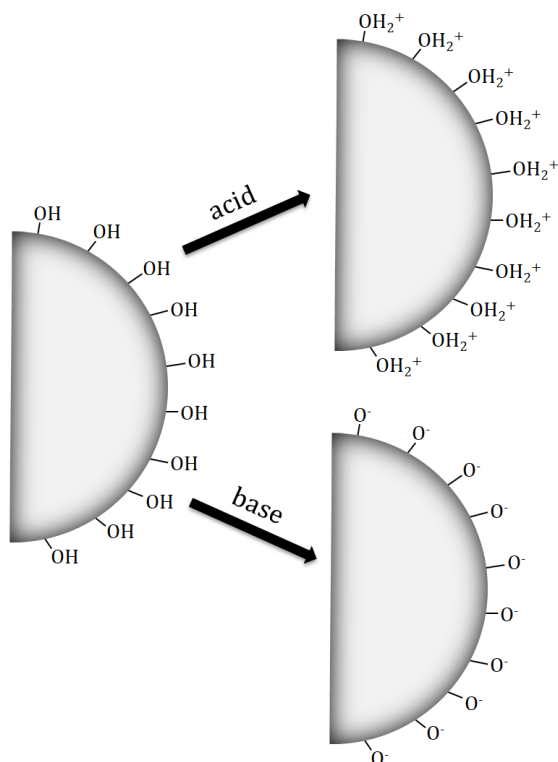


**Figure 2.3:** Image depicting the effect of adding acid or base to an amphoteric surface; the initially neutrally charged particle surface obtains either a positive (top right) or a negative (bottom right) surface charge.

$F$  is the Faraday constant ( $96\,485\text{ s A mol}^{-1}$ ),  $s$  is the specific surface area ( $\text{m}^2/\text{g}$ ) and  $c_m$  is the mass concentration of particles. The blank titrations are performed in the presence of background electrolyte only and in the same pH range as the particle titrations. This is done to subtract the effects of the background electrolyte on the pH electrode and the effect of any dissolved  $\text{CO}_2$  in the suspension.

Usually, the titrations of a particular colloidal system are run with at least three different electrolyte concentrations. If no specific adsorption of counter-ions is prevalent, the intersection between the curves will reveal the particles'  $\text{pH}_{\text{PZC}}$  ( $\text{PZC} = \text{point of zero charge}$ ), see Figure 2.4. This common interception point (CIP) is located where the curves intercept and at  $\text{SCD} = 0$  since the counter-ion's screening is no longer effective when there is no surface charge. As the pH increases or decreases, away from the  $\text{pH}_{\text{PZC}}$ , the absolute value of the surface charge density increases as more and more amphoteric sites are deprotonated or protonated, respectively.

At higher ionic strengths, more counter-ions will be available to adsorb in the outer Helmholtz plane (see Figure 2.1), which will extrude protons from the inner plane, increasing the surface potential and, consequently, also the SCD (see Figure 2.5).

### Particle aggregation and gel formation.

Once the salt concentration is high enough to decrease the energy of the potential barrier sufficiently, particle aggregation is initiated. Two processes are involved in the aggregation: Brownian motion and convection (bulk movement of fluid) [4]. In most cases, only one of them is important, e.g., convection for large particles and Brownian motion for nanoparticles. Regarding kinetics, aggregation is either diffusion-limited (DLA) or reaction-limited (RLA). The former occurs when the probability of aggregation upon a collision between particles is 1. The latter occurs when the probability is less than 1 due to a significant potential barrier which leads to difficulty for the particle to approach close enough for them to stick to each other. DLA is more rapid than RLA.

To put it simply, there are three stages of aggregation: Early stage, middle stage, and late stage. Early-stage involves the formation of particle doublets. If these doublets continue to aggregate, fractal structures are formed in the middle stage. If the fractals are dense enough, sedimentation occurs. In the late-stage aggregation, further phase separation occurs, but there is also the possibility of gel formation (see Figure 2.6). A gel is a three-dimensional network consisting of aggregated particles in contact with each other without sedimentation. Gelation is induced by charge screening by counter-ions, and the time it takes for a gel to form depends on the particle type (surface charge, roughness, size, etc.) and the electrolyte (ion composition and concentration). Despite the extensive aggregation of particles in the gel, the resulting volume is not much smaller than the initial colloidal suspension's. Experiments have shown that the gel contains both aggregated and primary particles detached from the network structure [9].

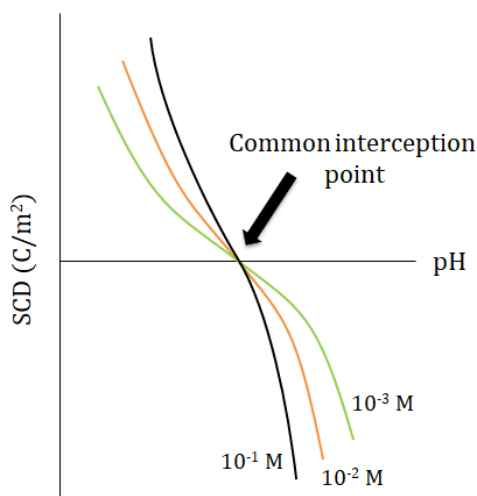


**Figure 2.4:** Schematic graph of three titrations of suspensions of particles at ionic strengths of  $10^{-1}$ ,  $10^{-2}$ , and  $10^{-3}$  M showing the CIP.

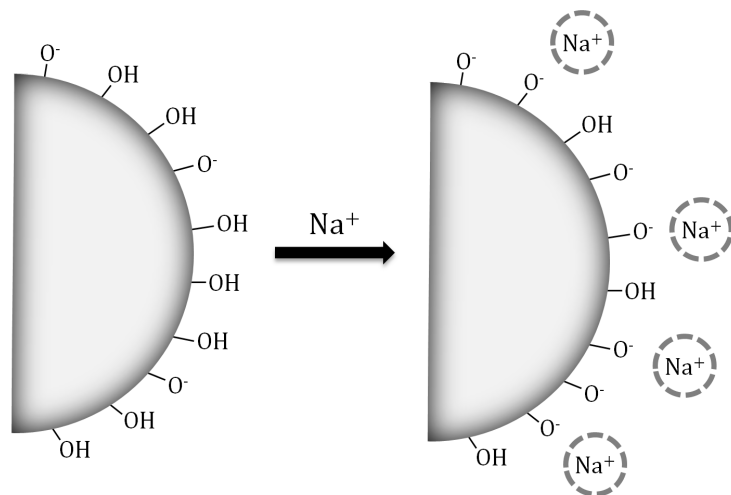


**Figure 2.5:** Schematic image demonstrating the effect of adding sodium ions to an already negatively charged surface, further increasing the surface potential and SCD. The rest of the EDL has been omitted for clarity.

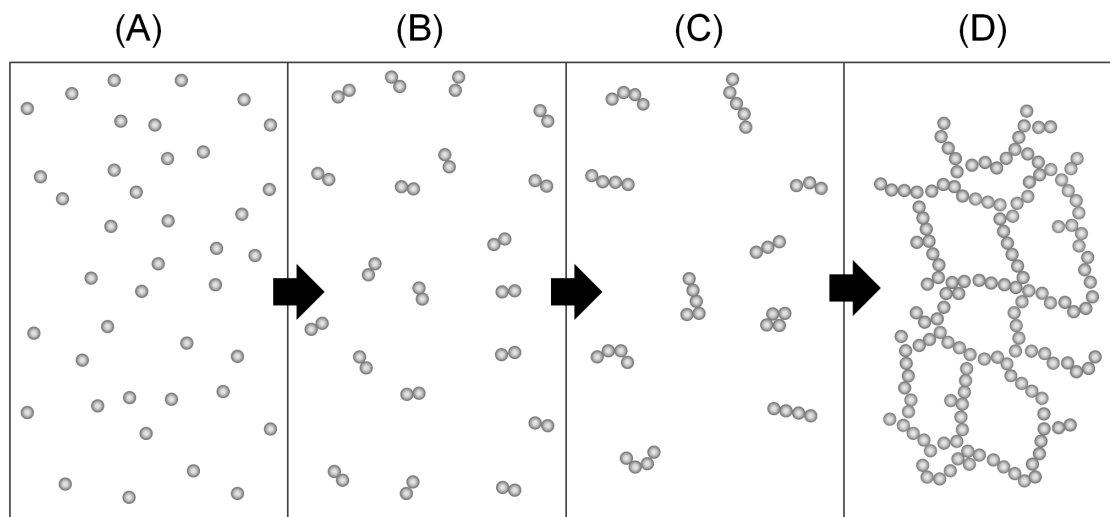


**Figure 2.6:** Image depicting the various stages of aggregation for a monodisperse colloidal system (A) to the formation of a gel in the late-stage of aggregation (D). Inbetween are the early-stage (B) with the formation of doublets and the middle-stage (C) where fractals have started to form. Note that additional particles have been added to (D) for clarification of the structure of the 3D network.

## 2.2 Solution chemistry

In the realm of solution chemistry, topics such as solvation, colloidal interactions, diffusion, dielectric permittivity, complex formation, hydrogen bonding, and pH are of importance. When the solvent is water, the dipole moments of the H<sub>2</sub>O molecules and the relatively strong hydrogen bonds make the interactions between solute and solvent molecules further complex.

### 2.2.1 Ion hydration

Depending on their size and charge, ions dissolved in water will have a hydration layer around their surface. As a general rule, the extent of surface hydration increases with decreasing ion radius and increasing net charge. Besides determining the size of the hydration shell, other types of quantities of the extent of hydration of an ion are water molecule exchange rates, Gibbs activation energies of the water exchange ( $\Delta G_{\text{exchange}}^\ddagger$ ), water molecule residence times, and self-diffusion coefficients [10]. In addition, the dynamic viscosity ( $\eta$ ) of an electrolyte solution can be used to obtain information on ionic hydration in the form of viscosity  $B_\eta$  coefficients derived from the Jones-Dole expression [11]:

$$\left[\frac{\eta}{\eta_{\text{water}}} - 1\right] = A_\eta c^{1/2} + B_\eta c + \dots \quad (2.6)$$

Ionic  $B$  coefficients can also be determined by NMR relaxation experiments. If  $B > 0$ , the ion is considered hydrated, i.e., surrounded by more or less immobile water molecules, and vice versa. Examples of values of  $B$  are shown in Table 2.1. As mentioned above,  $B$  coefficients can be correlated to whether the ions are structure makers or structure breakers [12, 13]. Structure maker ions interact strongly with the water molecules surrounding their surfaces, i.e., they have  $B$  coefficients larger than 0.

Dielectric relaxation spectroscopy (DRS) is a useful technique to obtain information of ion hydration. The polarization of a species in response to a time-dependent external electric field is measured and plotted in the form of relative permittivity ( $\epsilon'(\nu)$ ) and loss ( $\epsilon''(\nu)$ ) spectra as a function of frequency [14]. DRS of aqueous electrolytes can provide information on the hydrogen bonding properties around the ion surface. Small and highly charged ions will interact strongly with the surrounding solvent, slowing down the dynamics of the water molecules nearest to the ion surface. The effect of these interactions are visible in the dielectric permittivity spectra of electrolytes at different ionic strengths;  $\epsilon'(\nu)$  decreases with increasing salt concentration. The number of irrotationally bonded water molecules can be calculated from DRS data, yielding an "effective solvation number" ( $Z_{\text{ib}}$ ) of the analyzed electrolyte.

**Table 2.1:** Ionic B coefficients and solvation numbers for some common cations and anions, as determined by  $^1\text{H}$  NMR relaxation [10] and dielectric relaxation spectroscopy [14], respectively.

Ion	Li <sup>+</sup>	Na <sup>+</sup>	K <sup>+</sup>	Rb <sup>+</sup>	Cs <sup>+</sup>	Mg <sup>2+</sup>	Ca <sup>2+</sup>	Sr <sup>2+</sup>
<b>B coefficient</b>	0.14	0.06	-0.01	-0.04	-0.05	0.50	0.27	0.23
<b>Z<sub>ib</sub>(0)</b>	8-12	4.5	0	-	0	14	-	-
<b>CN</b>	4	6	8	-	8	6	-	-
Ion	Ba <sup>2+</sup>	SO <sub>4</sub> <sup>2-</sup>	F <sup>-</sup>	Cl <sup>-</sup>	Br <sup>-</sup>	I <sup>-</sup>	CO <sub>3</sub> <sup>2-</sup>	NO <sub>3</sub> <sup>-</sup>
<b>B coefficient</b>	0.18	0.12	0.14	-0.01	-0.04	0.08	0.25	-0.05
<b>Z<sub>ib</sub>(0)</b>	-	10	-	0	0	0	0	13
<b>CN</b>	-	7-12	-	6	6-8	8-9	6-9	-

Values of  $Z_{\text{ib}}$  and first-shell coordination numbers (CN) of some inorganic ions at infinite dilution are shown in Table 2.1. The CN values were obtained from computer simulations and scattering experiments. Buchner [14] attributed the difference in  $Z_{\text{ib}}$  and CN to that the former is more affected by the ion-solvent interaction strength, while the latter heavily depends on the water packing around the ions.

### 2.2.2 Ion pairing and activity coefficients

When a so-called strong salt is dissolved in water, it is often assumed that the ions are fully dissociated at dilute concentrations. This assumption has been debated, and Yizhak Marcus (2006) [15] has written an extensive review on the concept of ion pairing. An ion pair is generally defined as two oppositely charged ions that are located within a certain distance to each other due to long-ranged electrostatic attractive forces. The lifetime of an ion pair has been estimated to be around 1 nanosecond.

The extent of ion pairing in a strong electrolyte is related to the dissolved salt's mean ion activity coefficient ( $\gamma_{\pm}$ ), which corresponds to ion-ion interactions. Ion pairs are categorized into solvent-separated (2SIP), solvent-shared (SIP), and contact (CIP), depending on the extent of solvation left around the ions. Figure 2.7 illustrates the different types of ion pairs.

The mean ion activity coefficients of electrolytes can be determined by both experimental and computational methods. One common experimental method is measuring vapor pressure as a function of salt concentration using the isopiestic method [16]. Another alternative is to use ion-selective electrodes. By performing extensive Monte Carlo simulations, thermodynamic data can be obtained from electrolyte systems which can be further converted to ion activity coefficients [6].

Indications of ion pairing prevalence even at dilute concentrations have been

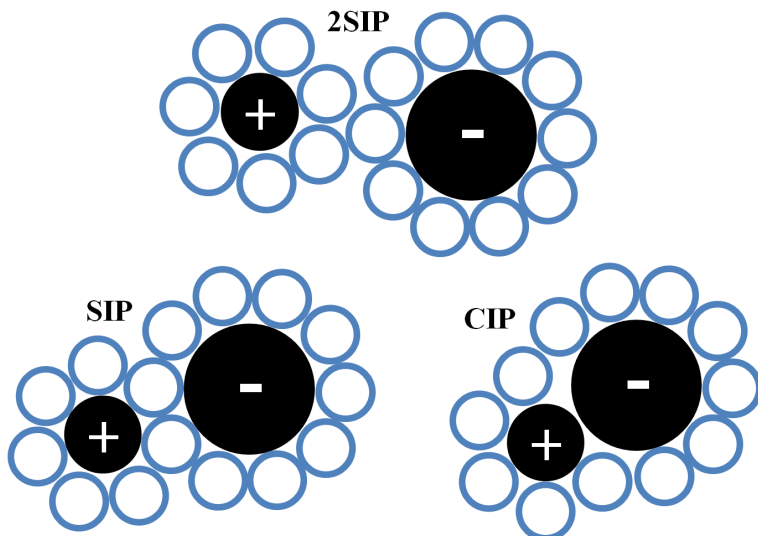


**Figure 2.7:** The different types of ion pairs: Solvent-separated (2SIP), solvent-shared (SIP) and contact ion pairs (CIP). The blue circles represent solvent molecules.

found using MC simulations by adjusting the parameter regarding the hydration radius of the ions, [17, 18]. More evidence of ion pairing near charged surfaces has been published recently. Adar et al. (2017) [19] found by non-linear Poisson-Boltzmann calculations that ion pairs are accumulated at charged interfaces, depleting the number of free ions both in the bulk and at the interface, which affects the Debye screening length in the solution.

## 2.3 Adsorption theory

Two different adsorption mechanisms can be active during the adsorption process: chemisorption and physisorption. During physisorption, the adsorbing molecule is intact during the interaction, for example, by van der Waals or attractive electrostatic forces. A layer of adsorbates physically adsorbed to a solid material acts similarly to a two-dimensional gas and is therefore very mobile, and the process is considered fully reversible. Chemisorption has a larger heat of adsorption than physisorption, meaning that a significant amount of energy is released upon adsorption. This leads to irreversible adsorption due to the formation of strong chemical bonds. Chemisorption is highly specific and involves electron transfer between adsorbate and adsorbent. For many sorbates and surfaces, both adsorption types are of importance [20].

Considering the adsorption of molecules from the gaseous or liquid phase, it is generally an exothermic process. This is due to the adsorption process decreasing the translational and rotational freedom of the sorbate, leading to a loss in entropy.

For the adsorption to be spontaneous,  $\Delta G$  has to be negative ( $\Delta G = \Delta H - T\Delta S$ ), and therefore the heat of adsorption ( $\Delta H$ ) is required to be negative as well. For some small and polar adsorbates, for example, water and ammonia, physisorption through electrostatic attractions to an ionic surface may be so large (approximately 105-125 kJ/mol) that the heat of adsorption reaches values normally only reached by chemisorption [20].

### 2.3.1 Aqueous phase adsorption.

Adsorption in the aqueous phase is different from the gas phase. First of all, the occupation of water molecules at the surface of the adsorbent induces competition for adsorption sites. Therefore, liquid phase adsorption can be seen as an exchange process. If the adsorbate concentration is dilute, the extent of adsorption is often readily investigated and modelled. The Langmuir isotherm, shown in Figure 2.8, is one of the most common isotherms and relates the surface excess of adsorbate ( $\Gamma$ ) with the adsorbate concentration. In general, it is valid for both the gas phase and liquid phase adsorption. Other common forms of isotherms are Freundlich, Sigmoidal, linear, high affinity, and step isotherm [21].

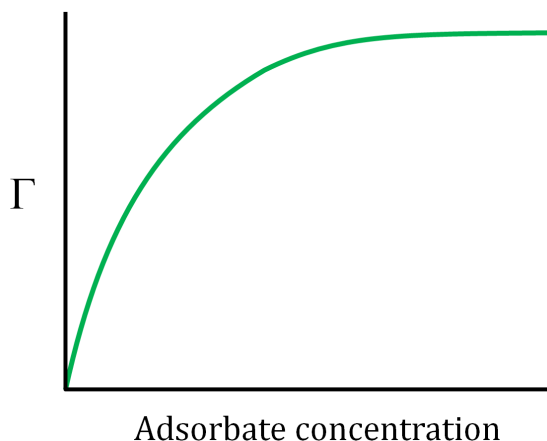


**Figure 2.8:** A conventional Langmuir isotherm curve showing the surface excess  $\Gamma$  of an adsorbate as a function of its concentration.

Strictly speaking, the Langmuir isotherm is valid for surfaces that are clean, smooth, and non-porous and where the adsorption is reversible and purely physical. The adsorbate has to adsorb in a uniform layer and behave as simple hard spheres. The adsorbate must be non-interacting and adsorb uniformly in a single layer. The linearized Langmuir equation provides a way to obtain the maximum adsorption capacity ( $q_{\max}$ ) by dividing both terms in Equation 2.7 by  $C_e$  and plotting  $1/q_e$  vs.  $1/C_e$ .

$$\frac{C_e}{q_e} = \frac{1}{q_{max}K_L} + \frac{C_e}{q_{max}} \quad (2.7)$$

$C_e$  equals the total adsorbate concentration,  $q_e$  is the concentration of adsorbed molecules on the surface, and  $K_L$  is a constant related to the interactions between the adsorbate and adsorbent.

For heterogeneous surfaces, the empirical Freundlich isotherm model [22] is commonly more accurate than the Langmuir model and therefore provides a better fit to the adsorption data obtained from experiments. By taking the logarithm of Equation 2.8, Equation 2.9 is created, and plotting the  $\log(q_e)$  term against  $\log(C_e)$  yields a straight line with the slope  $1/n$  and Y-intercept  $\log(K_F)$ .

$$q_e = K_F C_e^{\frac{1}{n}} \quad (2.8)$$

$$\log(q_e) = \log(K_F) + \frac{1}{n} \log(C_e) \quad (2.9)$$

In the equations above,  $1/n$  represents the fraction of adsorption sites that are occupied ( $0 < 1/n < 1$ ), and  $K_F$  is related to the adsorbate-adsorbent affinity [23]. Although the Freundlich model often is more suitable to use than the Langmuir model, it does not provide a maximum adsorption capacity since the model does not allow saturation of the surface by adsorbate molecules to be reached [24].

### The role of surface charge in adsorption

To characterize the electric charge of a solid particle suspended in water, zeta potential (ZP) measurements are commonly performed. This potential is affected by the presence of ions located in-between the surface and the slip plane of the colloids in the suspension. Therefore, it is often smaller in magnitude than the true surface charge/potential ( $\Psi_0$ ). The ZP will still indicate the electric field's strength around the surface of the particle. This quantification is important when considering both Coulombic interactions and dispersion forces between adsorbates and material surfaces. The ZP also gives a clue on the stability of the nanoparticles with respect to aggregation, as a high charge will make their surfaces repel each other. At a certain pH, the ZP equals 0, and this point is called the isoelectric point (IEP). The  $\text{pH}_{\text{IEP}}$  varies with the type of surface. Typical values of  $\text{pH}_{\text{IEP}}$  [25] are 6-8 for iron oxides, 7-10 for aluminium oxides and 7-10 for zinc oxides. Silica has got an unusually low  $\text{pH}_{\text{IEP}}$  of 2-3, sometimes even lower.

The ZP is not only a measurement of a colloidal system's stability towards aggregation but can also indicate whether a material would be a suitable adsorbent. The most apparent adsorption mechanism would be an electrostatic attraction between

a charged surface and an oppositely charged molecule. In addition, a highly charged surface has got the potential to induce a dipole moment in a neutral molecule, enabling adsorption by dipole-induced dipole attractive forces. The latter mechanism is especially relevant for adsorbates with large polarizabilities.

## 2.4 Nanomaterials

A material that has at least one dimension (including pores) on the nanoscale is called a nanomaterial. Depending on the diameters of the pores, they are divided into micropores ( $< 2$  nm), mesopores (2-50 nm), and macropores ( $> 50$  nm). Pores can also be classified according to their availability (Figure 2.9) [26]. In addition, the geometry of the pore can be used for classification, such as cylinder shape, cone shape, slit shape, and ink bottle shape.

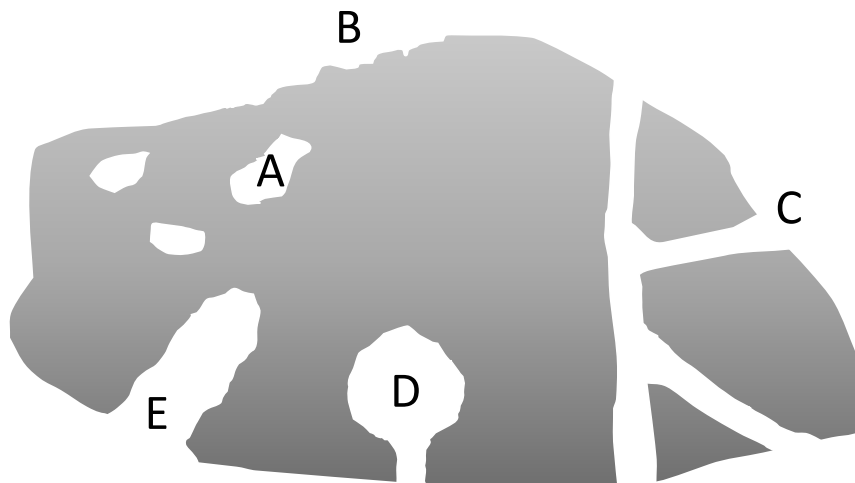


**Figure 2.9:** Schematic image of the different types of pores according to their availability. (A): Closed pores. (B), (D), and (E): Open pores. (C): Pores open at  $\geq 2$  ends.

The enhanced reactivity of nanoparticles and porous materials stem from their large surface area to volume ratio. A single grain of sand has got a typical diameter of 1 mm, resulting in a specific surface area (SSA) of approx.  $4.2 \cdot 10^{-3}$  m<sup>2</sup>/g. In comparison, an amorphous silica nanoparticle with a diameter of 22 nm has got an SSA of about 140 m<sup>2</sup>/g, and activated carbon has got SSAs of several hundreds square meters per gram owing to their porosity. Even more impressive, MOFs and zeolites have calculated SSAs of several thousands [27], depending on chemical composition, pore structure (related to the crystal structure) and crystallinity.

### 2.4.1 Activated carbon

Using intense heat treatment of biological materials, activated carbon (AC, also called functionalized carbon/charcoal) can be synthesized. This produces high-surface area porous materials with different chemical surface properties depending on factors such as burning temperature and treatment conditions. Typical starting materials include coconut shells [28], sawdust [29], banana peel [30], paper mill sludge [31], and agricultural waste [32].

The carbon atoms located at the surface of AC are predominantly  $sp^2$  hybridized [33] and much more reactive than the  $sp^3$  hybridized graphene sheets located in the bulk material. Other chemical species on the surface include a varying amount of heteroatoms (e.g., N, O, H), which to a large extent determine its chemical nature and hence its reactivity towards adsorption. The oxygens originate from exposure of AC to air, while nitrogen and hydrogen have been present in the precursor organic material from the beginning. Oxygen-containing functional groups on AC's surface are lactones (ester rings), carboxylic acids, quinones (an unsaturated cyclic compound with two carbonyl groups), carboxyl anhydrides ( $R-CO-O-CO-R$ ), cyclic peroxides (ring with  $O-O$  bond), phenols, etc. [34].

Due to the many types of AC originating from their various synthesis routes, the surface of functionalized carbon in aqueous solution can be either positively or negatively charged at physiological, near-neutral pH. A negative surface charge stems from dissociated chemical groups on the surface, while a positive surface charge originates from alkaline chemical groups and electron-donating graphene sheets acting as Lewis-bases towards water, forming alkaline complexes [35].

The chemical treatment of AC is popular for research purposes since it alters the chemistry of the surface, possibly enhancing its adsorption efficiency. For example, treatment with aqueous solutions of either NaOH or  $HNO_3$  significantly modifies the surface chemistry of AC [34]. The alkaline treatment increases the surface area and pore volume, while the acid treatment does the opposite, possibly due to newly formed surface nitrate groups blocking some of the pores. Another consequence of the acid treatment is the oxidation of the graphene sheets located on the AC surface, which introduces oxygen-containing acidic groups. This lowers the  $pH_{PZC}$  of the surface and increases the negative surface charge the AC carries around neutral pH.

### 2.4.2 $TiO_2/AC$ composites

Doping titanium(IV) oxide ( $TiO_2$ ) crystals on the surface of AC is a relatively simple way to alter the surface properties of the AC. As mentioned in the above section, the AC can have a varying degree of hydrophobicity/hydrophilicity depending on the surface composition. By adding  $TiO_2$  to the AC, it will become more hydrophilic and, in addition, will alter its electrostatic properties. The  $TiO_2/AC$  composite can be considered a type of Janus particle, i.e., it contains more than one type of physically and chemically diverse surfaces [36]. This could potentially be advantageous for the adsorption in solutions containing several different adsorbates, common in most natural systems, such as biological fluids, wastewater, etc.

The adsorption properties of  $TiO_2/AC$  composites have been studied before. Kang et al. (2018) [37] tested the desalination performance on  $TiO_2$ -doped AC

fibers (ACF) in aqueous NaCl. They found that the ACF doped with 15 vol% titanium(IV) tetraisopropoxide (TTIP) increased the NaCl adsorption efficiency by 72%, compared to the raw ACF. The authors claimed that the enhanced efficiency was due to the increased wettability of the ACF surface, which promotes ion transport in the pores, and the presence of Ti-OH surface groups, contributing to additional "electrosorption" sites. The TiO<sub>2</sub> crystals on AC can be used as photocatalysts, as proven by Ao (2008) [38], where the adsorption and subsequent photodegradation of phenol on TiO<sub>2</sub>-coated AC. The coating increased the apparent quantum yield by 166% for the composite compared to pure TiO<sub>2</sub> nanoparticles.

### 2.4.3 Metal-organic frameworks.

Metal-organic frameworks (MOFs) are a group of relatively new hybrid materials with large surface areas due to their porous structure. Recorded specific surface areas lie between 100 and 10 000 m<sup>2</sup>/g, and the porosity is normally > 50% [27]. They consist of metal cations, acting as Lewis acids, linked with various organic ligands, Lewis bases, through coordination bonds. MOFs are crystalline nanostructures with a wide range of potential applications, such as catalysis, ion exchange, drug delivery, gas storage, separation and purification, polymerization, sensors, etc. Many MOFs are considered chemically stable, thanks to significant bond strengths and the number of coordination bonds, but depending on the conditions (e.g., solvent, water content, pH), some can morph into amorphous structures or decompose back to metal ions and organic ligands [39].

**MOF-235(Fe):** [Fe<sub>3</sub>O(1,4-BDC)<sub>3</sub>(DMF)<sub>3</sub>][FeCl<sub>4</sub>].

One of the iron MOFs synthesized and tested in this work is MOF-235. MOF-235 is an iron(III) terephthalic acid (TPA, also called 1,4-BDC: C<sub>6</sub>H<sub>4</sub>(COOH)<sub>2</sub>, Figure 2.10) metal-organic framework that is considered non-toxic [40]. It consists of hexagonally coordinated Fe<sub>3</sub>O clusters that are connected to each other by the carboxylic groups in the TPA ligands. The porosity of MOF-235 originates from hexagonal channels (diameter = 6.7 Å) spanning the crystal structure (Figure 2.11). The orange-colored material was first synthesized via a solvothermal route [40], but a microwave-assisted method [41] has also been successful. The BET surface area of the microwaved assisted product was 148 m<sup>2</sup>/g (vs. 135 m<sup>2</sup>/g for the solvothermal product) and the size of the crystals, as analyzed by SEM, was slightly smaller than the solvothermally synthesized particles; 3-4.5 μm. The surface of MOF-235 is positively charged due to an unbalanced ratio of Fe<sup>3+</sup>:TPA<sup>2-</sup> ions in the crystal structure and, therefore, FeCl<sub>4</sub><sup>-</sup> counter-ions are situated in the pores.

As mentioned, liquid phase adsorption on MOFs has been scarcely reported

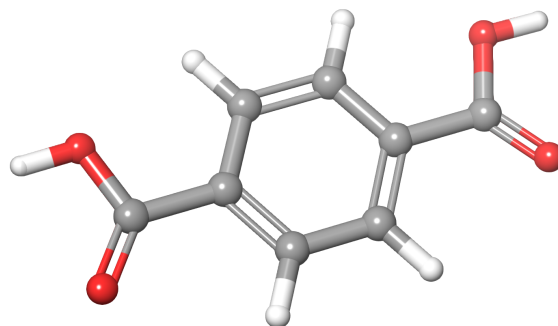


**Figure 2.10:** Structure of terephthalic acid, the linker molecules in MOF-235 and MIL-101. The model was drawn in Maestro 11.2.

in literature. Haque et al. (2011) tested the adsorptive ability of solvothermally synthesized MOF-235 [42] in aqueous solutions of methylene blue (MB), a cationic dye, and methyl orange (MO), an anionic dye. UV-vis spectroscopy was used for quantification of MB and MO and different solution pH, adsorbate concentrations and temperatures were tested. The negatively charged MO adsorbed at the surface to a greater extent than the positively charged MB and MOF-235 was significantly more effective than the reference AC adsorbent.

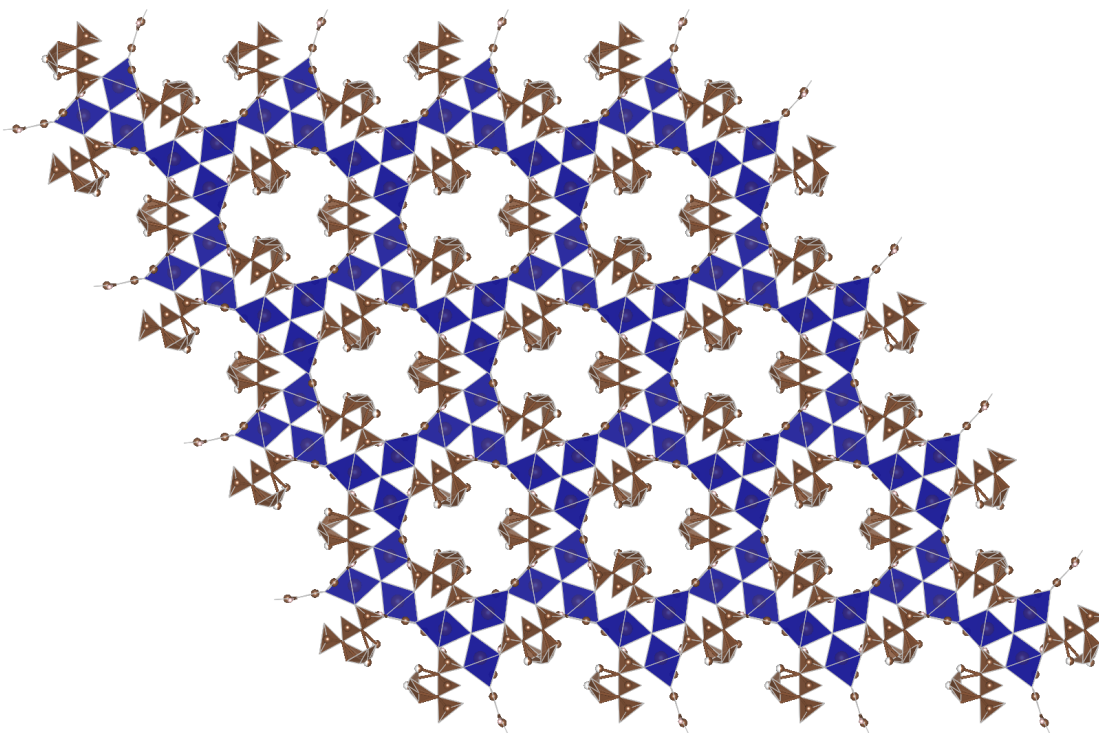


**Figure 2.11:** Structure of MOF-235, depicting its 2D hexagonal channels. Blue tetrahedra:  $\text{Fe}_3\text{O}$  clusters, brown: TPA linker molecules. The  $\text{FeCl}_4^-$  counter-ions have been omitted for clarity. The image [43] was made using the VESTA software and the crystallographic image file from Sudik, 2005 [40].

**MIL-101(Fe)** [ $\text{Fe}_3\text{O}(\text{OH})(\text{H}_2\text{O})_2(1,4\text{-BDC})_3$ ].

The other iron(III) terephthalate MOF used in this project is MIL-101, which has got an octahedral crystal structure [44] and is brown-orange colored. Besides oxygen from the carboxylic groups of TPA, each iron(III) oxide cluster is also coordinated to a hydroxyl group. Water molecules are located in the pores of the MOF, which can be exchanged for other molecules, indicating that the material could be suitable for liquid phase adsorption. MIL-101 contains two different near-spherical cages with diameters of 29 and 34 Å, respectively [45] (Figure 2.12).

MIL-101(Fe) has been successfully used to catalyze coupling reactions of pyrroles in liquid phase [45]. It was found to be more effective than other iron MOFs (MIL-88B and MIL-53), likely due to its larger surface area and pores. MIL-101 has been amino-functionalized by Barbosa et al. (2017) [47] to investigate its catalytic efficiency (ring-opening of cyclohexene oxide using aniline). Both the original and

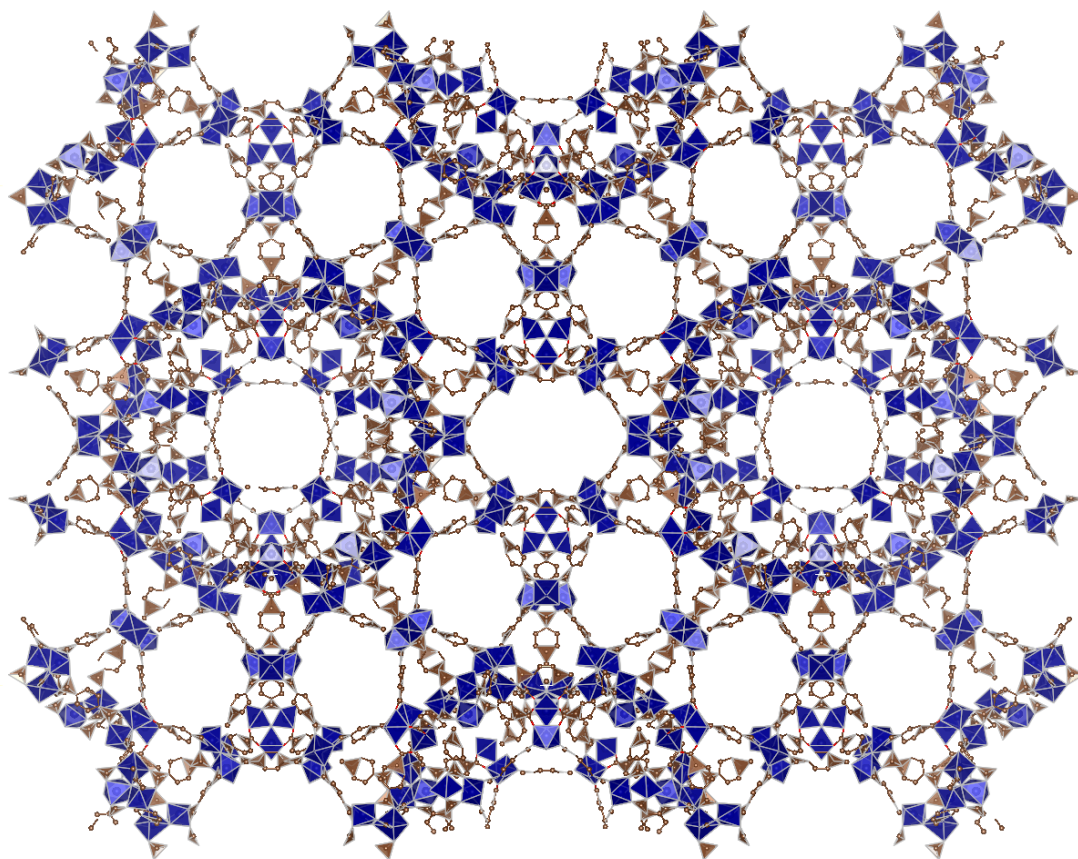


**Figure 2.12:** Structure of MIL-101 showing its 3D cage structure. Blue tetrahedra:  $\text{Fe}_3\text{O}$  clusters, brown atoms: TPA linker molecules. The image [43] was made using the VESTA software and the crystallographic image file from [46].

the functionalized material showed good catalytic properties. The catalyses were performed in acetonitrile.

#### 2.4.4 Functionalized nanocellulose

Cellulose is a natural polymer material mainly found in plants composed of  $\beta$ -linked D-glucose units [48] (Figure 2.13). Examples of major cellulose sources include wood and cotton. Professor Hermann Staudinger [49] was the first to discover and describe polymers, including cellulose, in the 1920s. He remarked on the high molecular weight of some natural substances and stated the cause to be the covalent linkage of a high number of monomers into macromolecules.

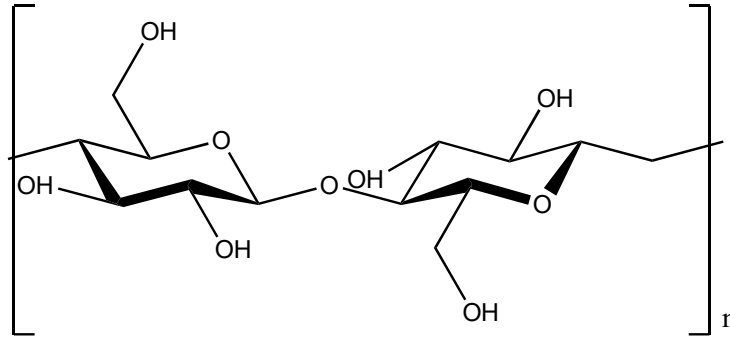


**Figure 2.13:** Molecular structure of the cellulose polymer.

The very first synthesis procedure of nanocellulose, in the form of microfibrillated cellulose (MFC), was first published in 1983 [50]. The MFC had an increased surface area and was readily made into a stable gel. Wood pulp was homogenized in different polar solvents in 2 wt% batches, resulting in an opaque MFC sol similar in consistency to mayonnaise with 25-100 nm wide and several micrometer long fibrils.

Since then, more types of nanocellulose have been synthesized, and among the most popular is crystalline nanocellulose (CNC), also called microcrystalline cellulose (MCC). CNC consists of smaller and more crystalline cellulose fibers than MFC and is produced by acid hydrolysis of cellulose. The acid dissolves the amorphous regions of the cellulose, resulting in nanocrystals with dimensions of  $5\text{-}70 \times 100\text{-}250 \text{ nm}^2$  (width  $\times$  length) [51]. The type of acid hydrolysis agent used governs the surface properties of the CNCs, e.g.,  $\text{H}_2\text{SO}_4$  yields a more strongly negative surface charge than, for example,  $\text{HCl}$ . The former also functionalizes the surface with  $-\text{OSO}_3$  groups ( $\text{pK}_a \approx 1.9$ ), resulting in sulfate-functionalized CNCs (SCNCs). The higher surface charge contributes to enhanced colloidal stability and more reactive sites for further functionalization.

The high aspect ratio, i.e., the length:width ratio of the fibers, of MFC and CNC make them prone to aggregate and form gels, but also give them interesting mechan-

ical properties. In combination with their biocompatibilities, they have wide range of applications, both on their own and as part of composite materials. Examples include canvas consolidation [52], biosensors [53], cartilage substitution [54], wound healing [55], and transparent nanopapers [56].

## 2.5 Odor molecules

Odor stems from certain organic molecules with high vapor pressures, giving them low odor detection thresholds. In some instances, such as in industries [57], agriculture [58], and used hygiene articles, the concentration of odor molecules can be high enough to cause a problem for the people living in the surrounding environment. It is therefore of utmost importance to develop adsorbent materials than can capture the odorants at the source.

Several odorants have been identified in used incontinence products, such as trimethylamine, cresols, guaiacol, 3-methylbutanal, and dimethyltrisulfide [1]. While some of these substances are developed in the body, there is also the potential for odor molecules to be bacterial metabolic products outside of the body, e.g., in the hygiene articles themselves.

### 2.5.1 p-Cresol

One of the most prevalent odor molecules in both urine and agriculture is p-cresol. In gas form, it has an odor threshold of 0.000054 ppm [59], corresponding to a molar concentration of 0.50 nM. This odor threshold is exceptionally low, for example acetic acid and ammonia have corresponding values of 0.0060 and 1.5 ppm, respectively.

The adsorption of o- and p-cresol on activated carbon was studied by Tamon et al. (1996) [60] at 35°C. Adsorption-desorption hysteresis was observed for both cresol types, suggesting that they bind irreversibly to the surface of AC. Other substances studied were found to adsorb reversibly. The major difference between the two groups of compounds is their functional groups. The irreversibly adsorbed molecules contained electron-donating groups (-OH and -NH<sub>2</sub>), while the reversibly adsorbed contained electron-withdrawing groups (-COOH, -NO<sub>2</sub>, and C=O). The same study found that the oxidation of the AC diminished the hystereses, benefitting the solvent regeneration as the adsorption was no longer irreversible. Whether the adsorption is reversible or irreversible is attributed to the LUMO and HOMO energy gap between the adsorbent and adsorbate, respectively. A small gap favors irreversible adsorption and vice versa. Since the electronic state of the adsorbate is fixed, the oxidation of AC must increase its LUMO energy level as the HOMO-LUMO energy gap has

increased.

## 2.6 Synthetic urine

Human urine contains a large number of ions and molecules. Since it is a so-called biological waste material, its composition can vary greatly between individuals; over 3000 different metabolites have been identified in total (as of 2013) [61]. The reason for this diversity is that urine originates from the kidney, whose role in the body is to regulate fluids and remove toxins from the blood system. Water-soluble waste products are effectively disposed of through urination through the kidneys. This enables the usage of urine as a diagnostic tool, e.g., for the detection of cancer, drug use, disease, infections, diabetes, and toxic exposure. Besides water, the chemical of the highest concentration in urine is urea (range: 110-390 mM, Figure 2.15), which is the main metabolic product of amino acids.

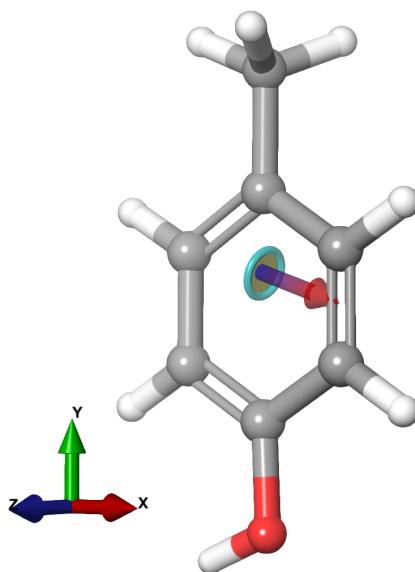


**Figure 2.14:** Molecular structure of p-cresol, showing its dipole moment as calculated using DFT. The model was made in Maestro.

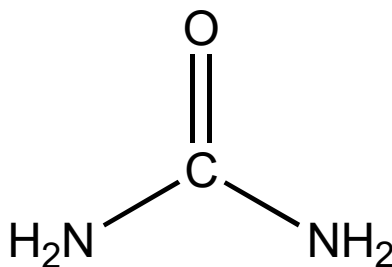


**Figure 2.15:** Urea.

The complexity of real urine makes it more practical to use synthetic urine (SU) in experiments where a urine-like environment is desirable. In literature, the composition and concentrations of the species in SU can vary significantly. Sarigul et al. [62] suggested a new protocol of a SU that is very similar to real urine. Besides the typical ions ( $\text{Na}^+$ ,  $\text{K}^+$ ,  $\text{NH}_4^+$ ,  $\text{Mg}^{2+}$ ,  $\text{Ca}^{2+}$ ,  $\text{Cl}^-$ ,  $\text{SO}_4^{2-}$ ,  $\text{PO}_4^{3-}$ ), the SU also contains urea (250 mM), uric acid (1.5 mM), creatinine (7.8 mM), and potassium oxalate (0.20 mM). The urea reduces the shelf-life of the SU, as it is readily hydrolyzed into ammonia and bicarbonate ions in water [63].

# Chapter 3

## Experimental Methods

This chapter consists of descriptions of the experimental methods utilized in this work, including the synthesis and functionalization of nanomaterials and their characterization methods, the adsorption experiments and the statistical method used in the analysis of the results, and a brief section of how the simulations were conducted.

### 3.1 Chemicals and instruments

All chemicals used were commercially obtained, of analytical grade, and used without further purification, unless stated otherwise.

For the titrations and gel-time determinations of silica, commercially available Ludox<sup>®</sup> TM nanoparticles were used, which are spherical, amorphous silica (SiO<sub>2</sub>) particles with an average diameter of 22 nm and a SSA of approximately 140 m<sup>2</sup>/g. The titrations were performed using a Titrando 905 (Metrohm) automatic titration device with a Unitrode easyClean (Pt1000, pH range: 0-14; temperature range: 0-100°C) pH electrode. The sulfate-functionalized crystalline nanocellulose (SCNC) were synthesized by another group according to references [64, 65].

The solvothermal MOF syntheses were performed in 100 mL PTFE liners in stainless steel autoclaves purchased from Boshi Electronic Instrument. The *ex-situ* products were synthesized in larger batches and were therefore kept in heat-resistant 250 mL glass bottles during the solvothermal syntheses. The heat treatments took place in a convection oven (Mettler UF30 Plus). The *ex-situ* MAXS analyses were done in narrow glass capillaries.

The nitrogen gas adsorption measurements were performed using a TriStar3000 instrument from Micromeritics, yielding BET surface areas and porous properties of each material. A Bruker AXS D8 Advance with Cu-K $\alpha$  laser source ( $\lambda = 1.54 \text{ \AA}$ ) and a PSD LynxEye detector was used for most of the XRD analyses. A selection of the MOF products were also analyzed using a Cr-K $\alpha$  source ( $\lambda = 2.29 \text{ \AA}$ ). The X-ray photoelectron spectroscopy (XPS) analyses were performed using a

PHI5000 VersaProbe III instrument with a monochromatic Al X-ray source ( $E = 1486.6$  eV) with a beam size of  $100\ \mu\text{m}$ . For the MOF products, SEM analyses were conducted using a FEI Quanta200 ESEM. SEM images of the  $\text{TiO}_2/\text{AC}$  composites were obtained by a Zeiss Ultra 55 FEG. Both of the SEM instruments were operated in high vacuum mode using a  $10.0$  kV operating voltage. Middle-angle X-ray scattering (MAXS) and wide-angle X-ray scattering (WAXS) were performed in vacuum using a Mat:Nordic instrument (SAXSLAB) with a Rigaku 003 +  $\text{Cu-K}\alpha$  X-ray source and a Pilatus (300 K/100 K) detector. XRF was performed with a SPECTRO XEPOS spectrometer. A Thermo Fisher iCAP Pro XP was used for the ICP-OES analyses. For the zeta potential measurements, a Malvern Nano ZetaSizer in backscattering mode ( $173^\circ$ ) with DTS1070 folded capillary cells were used.

## 3.2 Potentiometric titrations

In the titrations, the pH was adjusted by adding acid ( $0.10$  M) or base ( $0.10$  M) in small increments. The corresponding acid/base to the salt studied was used to avoid the influence of other ions. A maximum voltage drift of  $5$  mV/min was used. The maximum waiting time after each addition was set to  $10$  min with a maximum dosage of  $50\ \mu\text{L}$ . A thermostatic bath was used to keep the temperature of the system at  $25.0\ ^\circ\text{C}$ . To expel  $\text{CO}_2$ , the colloidal sol was bubbled by a flow of nitrogen gas for  $10$  min before the titration began. Each titration was performed in triplicate, and blank titrations were performed containing only salt solution. Since the salts have no buffering capacities on their own, they required a lower maximum voltage drift ( $1$  mV/min) and therefore took longer time to run. Calibrations of the pH electrode (pH =  $4.0$ ,  $7.0$ ,  $9.0$ ) were performed weekly.

The mass concentration of silica was  $2$  wt%, and the electrolyte concentrations were  $0.05$ ,  $0.10$ , and  $0.20$  M with respect to the cation, i.e., a  $0.10$  M salt concentration of  $\text{Na}_2\text{SO}_4$  was equivalent to a cation concentration of  $0.20$  M. As mentioned in the background section, both the SCD and gel-time of a colloidal system depend on the hydrated radius of the counter-ion, but the effect of the co-ion has not been studied as extensively. Since we wanted to investigate the co-ion effect, we chose the following salts:  $\text{NaCl}$ ,  $\text{NaNO}_3$ ,  $\text{Na}_2\text{SO}_4$ , and  $\text{KCl}$ ,  $\text{KNO}_3$ ,  $\text{K}_2\text{SO}_4$ . In the gel-time determinations,  $\text{NaClO}_3$  and  $\text{NaClO}_4$  were also included. To obtain SCDs of the silica in the different salt solutions, the pH was decreased from  $10$  to  $3$ .

Regarding the SCNC titrations, since the cellulose nanofibrils rapidly aggregate at higher salt concentrations and solid content, a mass concentration of  $0.6$  wt% and salt concentrations ( $\text{LiCl}$ ,  $\text{NaCl}$ ,  $\text{KCl}$ ) of  $1$  and  $5$  mM were used. The initial pH of the dispersions were  $\approx 3.2$ , so acid ( $0.1$  M  $\text{HCl}$ ) had to be added to reach pH  $< 2.5$  before initiating the titrations with base ( $0.1$  M  $\text{LiOH}$ ,  $\text{NaOH}$ ,  $\text{KOH}$ ) to pH  $10$ .

The blanks were treated the same way, negating any effect of the added acid on the pH measurements.

### 3.3 Gel-time determinations

Gel-times of silica nanoparticles with different counter- and co-ions in the solution was obtained by adding a certain amount of stock salt solution to the colloidal sol (Ludox<sup>®</sup> TM, 40 wt%) in a 50 mL Falcon tube before mixing thoroughly. The point of gelation was determined as the time it took for the silica to form a rigid gel (see Fig. 3.1). Final concentrations of the silica depended on the amount of salt solution added and ranged from 24 to 38 wt%. The cation concentrations of the salts studied were 0.13, 0.24, 0.33, 0.42, and 0.50 M. Since different volumes of the stock salt solutions had to be added to obtain the different cation concentrations, the final pH varied slightly between the concentrations.

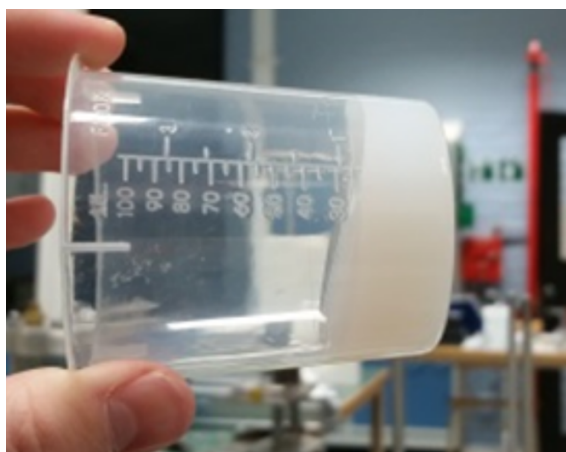


**Figure 3.1:** Picture of a silica gel, showing its rigidity.

## 3.4 Nanomaterials synthesis

### 3.4.1 MOF-235(Fe) and MIL-101(Fe)

Previously reported synthesis methods of MOF-235(Fe) almost exclusively use 3:5 Fe(III):TPA reagent ratios and 1:1 DMF:EtOH solvent ratios. This has shown to result in MOFs with inconsistent XRD patterns (Figure 3.2) and highly varying surface areas (Table 3.1), indicating that the references' products differ in the crystal phase. Another Fe(III) TPA MOF, MIL-101(Fe), has got a similar-looking XRD pattern, with the exception of the presence of diffraction peaks at low ( $4-6^\circ$ )  $2\theta$  angles. These peaks can be difficult to distinguish due to the strong background signal from the fluorescence of Fe(III) when using Cu  $K\alpha$  radiation. Since not all references use a knife edge to reduce the background signal, which can be especially prominent at low  $2\theta$  angles, it can be considered inaccurate to determine the end product from solely the XRD results. The most significant differences between MOF-235 and MIL-101 are their porosities and, consequently, surface areas. The results of previously published MIL-101(Fe) syntheses are summarized in Table 3.2, also showing a variation in BET surface area in the obtained products. These ambiguous results indicate that the conventional synthesis protocols for both MOF-235 and MIL-101 often yield mixed-phase products.

In order to clarify the influence of the synthesis conditions on the crystal phase, i.e., whether MOF-235 or MIL-101 is formed, extensive experimental work was conducted. More specifically, the conventional solvothermal synthesis protocol of

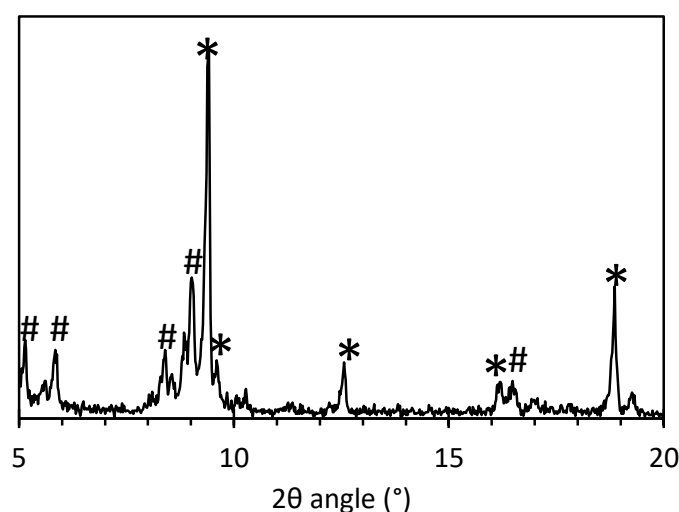


**Figure 3.2:** XRD pattern of a mixed-phase MOF-235/MIL-101 product obtained using the conventional solvothermal synthesis protocol by Haque et al. (2011) [42]. \* depicts MOF-235 peaks, # depicts MIL-101 peaks.

**Table 3.1:** Summary of the MOF-235(Fe) solvothermal syntheses from literature. All the syntheses were conducted in a 1:1 DMF:EtOH solvent.

Authors	Fe(III):TPA	T (°C)	t (h)	SA <sub>BET</sub> (m <sup>2</sup> /g)
Haque, 2011 [42]	0.6	80	24	25
Sudik, 2005 [40]	0.6	85	24	-
Duo, 2019 [66]	0.6	80	24	9.6
Li, 2016 <sup>1</sup> [41]	0.6	100	0.5	148
Li, 2016 [41]	0.6	80	24	135
Anbia, 2012 [67]	0.6	85	24	974
Le, 2016 [68]	1.0	85	48	540
DeSmedt, 2015 [69]	0.6	85	24	8.1
Wang, 2017 [70]	0.6	80	24	918
Simsek, 2017 [71]	0.6	85	24	-
Ge, 2019 <sup>1</sup> [72]	0.6	-	0.42	729

<sup>1</sup>Microwave-assisted synthesis**Table 3.2:** Summary of the MIL-101(Fe) solvothermal syntheses from literature. All the syntheses used DMF as solvent, unless stated otherwise.

Authors	Fe(III):TPA	T (°C)	t (h)	SA <sub>BET</sub> (m <sup>2</sup> /g)
Taylor-Pashow, 2009 <sup>1</sup> [73]	1	150	0.17	2500
Maksimchuk, 2012 [74]	2	110	20	3200
Wu, 2013 <sup>2</sup> [75]	1.33	150	24	-
Barbosa, 2017 [47]	2	110	20	-
Xie, 2017 [76]	2	110	20	2350
Simsek, 2017 [71]	2	110	24	-
He, 2019 [77]	1	110	20	601
Gegel, 2019 [78]	2	110	20	2865
Li, 2019 [79]	2	110	20	1173

<sup>1</sup>Microwave-assisted synthesis<sup>2</sup>TPA-NH<sub>2</sub> linker and 1:1 DMF:water solvent

MOF-235(Fe) was modified to test three different Fe(III):TPA ratios, three different DMF:EtOH solvent ratios, and three different post-heating equilibration times. The products were characterized by XRD, XPS, N<sub>2</sub> adsorption for BET surface area and BJH pore size distribution, and SEM. *Ex-situ* X-ray analyses were performed, where aliquots of the synthesis solution were sampled at certain time intervals during the solvothermal synthesis. The sampled products were analyzed by XRD to investigate the time-dependent crystallization of both MOFs. In addition, *in-situ* X-ray analyses using medium-angle X-ray scattering (MAXS) enabled us to study the crystallization process directly.

### Standard solvothermal synthesis

In the conventional solvothermal synthesis of MOF-235/MIL-101, iron(III) chloride hexahydrate (FeCl<sub>3</sub>\*6 H<sub>2</sub>O, 99.4%, VWR Chemicals) and terephthalic acid

(TPA,  $C_6H_4(COOH)_2$ , >98%, Alfa Aesar) were dissolved in N,N-dimethylformamide (DMF) during stirring. For the 0.6 reagent ratio, 0.738 mmol of Fe(III) and 1.23 mmol of TPA were used, respectively. The reagent solution was mixed with ethanol (95%), added to a PTFE-lined autoclave, and kept at 80°C for 24 h. The DMF solvent volume was kept constant at 30 mL, regardless of DMF:EtOH ratio. The product was vacuum filtrated and washed three times with a 1:1 mixture of DMF:EtOH before washing with EtOH only. The orange-colored powder products (Figure 3.3) were dried in a vacuum oven at 70°C and <50 mbar for 24 h and stored in a desiccator.

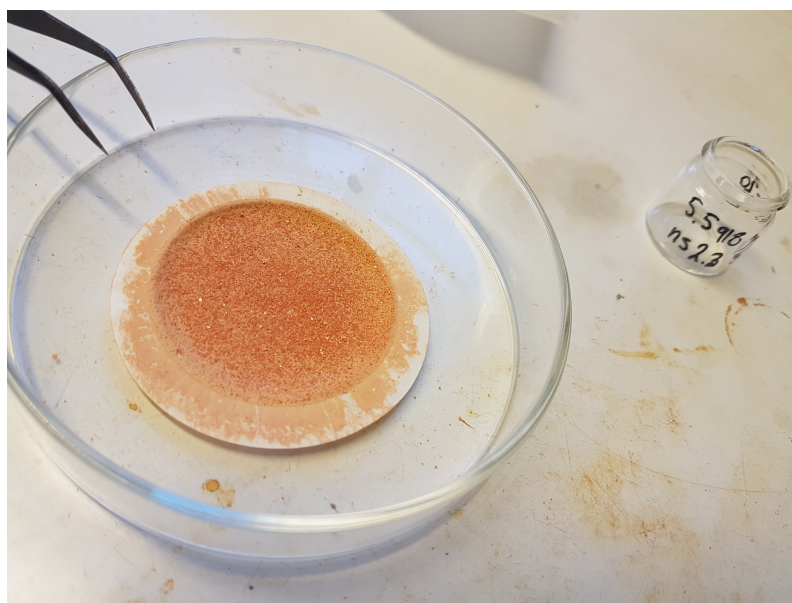


**Figure 3.3:** Photo of one of the Fe(III) TPA MOF products on a filter paper after filtration.

### ***Ex-situ* synthesis**

The *ex-situ* syntheses were performed using 1:1 and 3:1 DMF:EtOH ratios with a total solvent volume of 150 mL. Each three Fe(III):TPA ratios was tested, yielding six different syntheses. After 6, 12, and 24 hours, aliquots of 50 mL were extracted from the batch using a glass pipette. The aliquots were filtered, washed, and dried according to the standard procedure. The dried products were characterized using XRD and  $N_2$  adsorption isotherms.

### ***In-situ* synthesis**

Direct observations of the MOF crystallization process were enabled using time-resolved *in-situ* MAXS. Reagent solutions were prepared according to the ns2.2 synthesis procedure, i.e., a 4:3 Fe(III):TPA reagent ratio and a 1:1: DMF:EtOH

**Table 3.3:** Synthesis conditions of the conventional solvothermal Fe(III) TPA MOFs.

Synthesis	Fe(III):TPA	DMF:EtOH	$t_{\text{eq}}$ (days)
ns1.1	1	1:1	1
ns2.1	1.3	1:1	1
ns3.1	0.6	1:1	1
ns1.2	1	1:1	0
ns2.2	1.3	1:1	0
ns3.2	0.6	1:1	0
ns1.3	1	2:1	1
ns2.3	1.3	2:1	1
ns3.3	0.6	2:1	1
ns1.4	1	2:1	0
ns2.4	1.3	2:1	0
ns3.4	0.6	2:1	0
ns1.5	1	3:1	1
ns2.5	1.3	3:1	1
ns3.5	0.6	3:1	1
ns1.6	1	3:1	0
ns2.6	1.3	3:1	0
ns3.6	0.6	3:1	0
ns1.7	1	1:1	2
ns2.7	1.3	1:1	2
ns3.7	0.6	1:1	2

solvent ratio. Three temperatures were tested: 80, 85, 90°C. A scan in the 0-10  $\text{\AA}^{-1}$   $q$  range was conducted every 15 min for  $\approx 20$  h. A small amount of the reagent solution was carefully added to a thin glass capillary and sealed with glue before starting the synthesis and simultaneous MAXS analysis. The X-ray beam was focused at the bottom of the capillary, as the solid product should have a higher density than the solution. However, the production of gas during the synthesis sometimes lead to a separation of phases and push the solid upwards (Figure 3.4 (A)), making the X-ray beam miss the MOF phase. The (B) and (C) photos in Figure 3.4 show the solution capillary before and after a successful experiment.

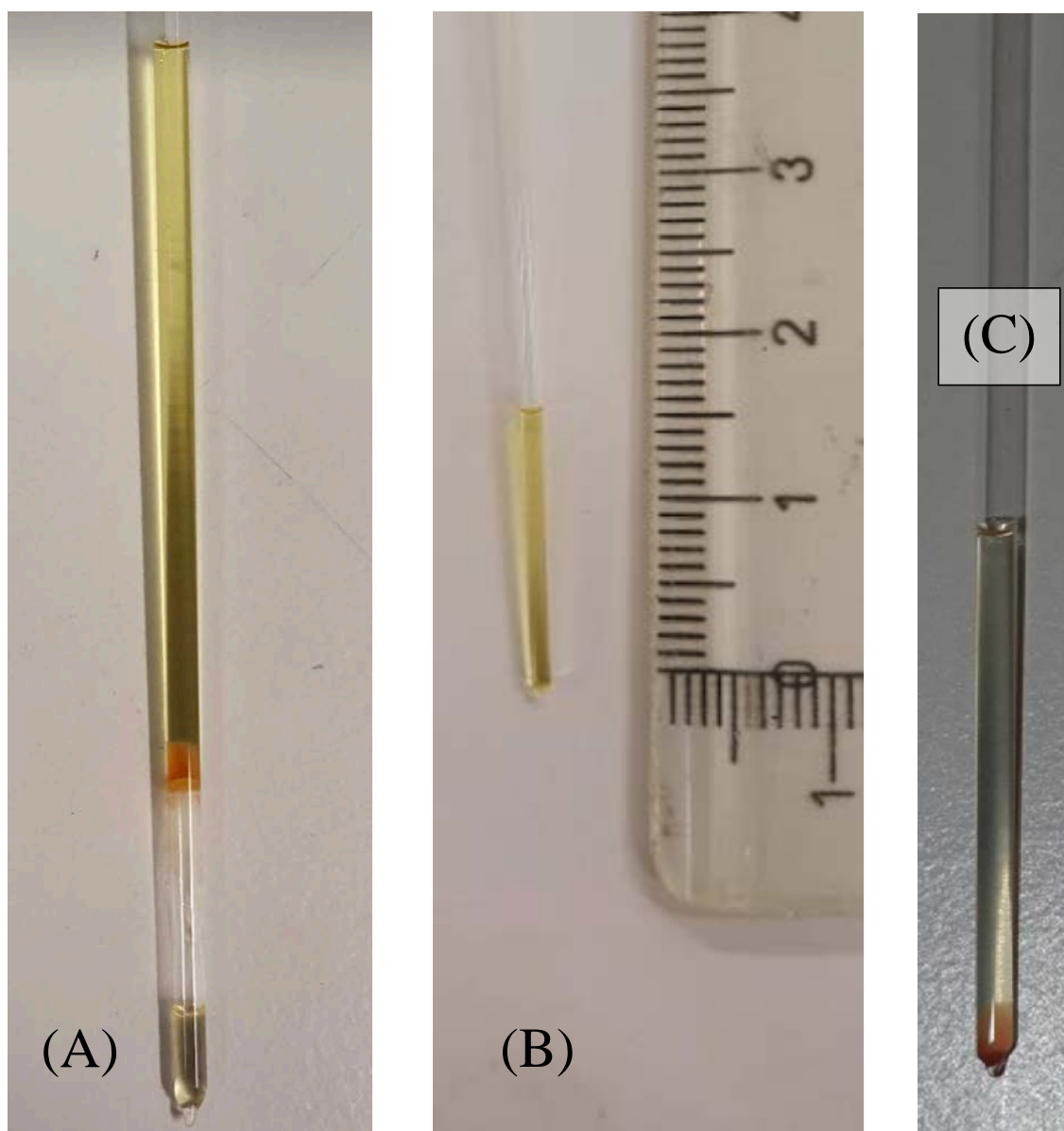


**Figure 3.4:** Photos of the glass capillaries used in the *in-situ* MAXS experiments. (A) shows a capillary where the analysis had failed due to phase separation. (B) and (C) show a capillary before and after a successful synthesis and analysis at 90°C.

#### 3.4.2 Activated carbon

In order to compare the adsorption efficiencies of mesoporous materials with different surface properties, commercial activated carbon ( $AC_0$ ) and its oxidized version ( $AC_{ox}$ ) were used.  $TiO_2$  grafting further altered the surface chemistry of the materials. To confirm the degree of  $TiO_2$  grafting and the implications of introducing  $TiO_2$  crystals on the AC surface, the products were characterized by XPS, XRF, XRD, water wetting angles, zeta potential, and nitrogen adsorption measurements.

##### AC oxidation

Activated charcoal in powder form was purchased from Merck (catalogue number: 1.02186.0250). In an attempt to alter the material's surface chemistry, 10 g of  $AC_0$  was oxidized using 6 M nitric acid [80] by boiling under reflux at  $100^\circ C$  for 3 h. After cooling, the material was washed with MQ water during vacuum filtration until the filtrate came out neutral ( $pH \approx 7$ ). The resulting oxidized material was dried at  $150^\circ C$  for  $>24$  h and called  $AC_{ox}$ . This procedure was taken and adapted from Figueiredo et al. (1999) [81].

##### $TiO_2$ grafting on AC

The crystallization of  $TiO_2$  on  $AC_0$  and  $AC_{ox}$  was done by adding the AC to titanium(IV) tetraisopropoxide in isopropanol according to the procedure by Kang et al. (2018) [37]. Three different concentrations of TTIP were tested: 5, 15, 25 vol%. The grafting was done by adding 1 g of AC to 20 mL of TTIP solution for 1 h at room temperature. The solid was filtered and washed with MQ water, isopropanol, and ethanol and dried at  $100^\circ C$ . This yielded the "raw" products. Each material was dispersed in MQ water (100 mL) and ultrasonicated for 30 min at 50% amplitude. An ice bath and the pulse mode (1 s + 1 s) were used to avoid overheating the sonicator probe.

## 3.5 Characterization methods

A brief summary of the theory behind the characterization techniques used in this work will be presented here.

### 3.5.1 Nitrogen adsorption

The adsorption isotherm of  $N_2$  near its condensation point, i.e., 77 K (-196.15°C), at different partial pressures ( $p/p_0$ , with  $p_0$  being the saturation pressure of the gas) yields, after some calculations and approximations, the surface area and pore size distribution of a porous material. Other gases can be used to obtain the surface area of a solid, such as Argon. The most important properties of a gas used in these types of experiments are inertness and size. The vdW radius of  $N_2$  is 320 pm [82], making it small enough to penetrate narrow pores. It is also chemically inert due to its triple bond between the two nitrogen atoms. Since  $N_2$  is the most common gas in the atmosphere and therefore cost-efficient, it is the standard gas to be used in BET surface area determinations.

From the BET theory, named after Brunauer-Emmett-Teller [83], the partial pressure region of 0.05-0.35 is used to calculate the BET surface area of a solid. Often a more narrow region of 0.05-0.20 is chosen to avoid the influence of more than one layer of gas molecules.

$$\frac{p}{V(p_0 - p)} = \frac{1}{V_m c} + \frac{c - 1}{V_m c} \frac{p}{p_0} \quad (3.1)$$

With  $V$  being the volume of adsorbed  $N_2$  gas as a function of partial pressure,  $V_m$  being the required volume of  $N_2$  to form one layer of gas molecules on the entire surface of the material, and  $c$  being a constant equal to  $e^{E_1 - E_L/RT}$ .  $E_L$  is the heat of liquefaction, and  $E_1$  is the heat of adsorption of the first gas layer. Using Equation 3.1, one can plot the left-hand term vs.  $p/p_0$  and obtain a straight line with a slope of  $(c-1)/V_m c$  and an intercept of  $1/V_m c$ . From  $v_m$ , the BET surface area ( $SA_{BET}$ ) can be calculated using the known area ( $A_{N_2} = 16.2 \cdot 10^{-20}$  m<sup>2</sup>/molecule) and molecular volume of a  $N_2$  molecule (22.414 L/mol, Equation 3.2).

$$SA_{BET} = \frac{V_m N_A}{22.414} A_{N_2} \quad (3.2)$$

For micro- and mesoporous materials, it is possible to determine their pore size and volumes using the equations and models presented by Barrett-Joyner-Halenda (BJH) in 1951 [84]. The BJH theory relates the amount of adsorbed gas molecules at large  $p/p_0$  values with the pore size of a material. As  $p/p_0$  approaches 1, capillary condensation fills the pores with gas, according to the Kelvin theory. In summary,

the Kelvin effect states that the phase equilibrium for a curved surface is different from a planar surface. The curvature makes it more favorable for gas molecules to condense inside of small pores than stay in the gas phase. For many types of porous materials, isotherm hysteresis occurs due to the presence of pores that are more narrow at the top than the bottom, leading to a higher energy requirement for desorption than for adsorption [4].

By making a t-plot, pore areas and volumes can be determined from N<sub>2</sub> adsorption isotherms of porous materials [85]. The adsorbed volume of gas is plotted against the "average thickness of the adsorbed layer" on a flat surface, i.e., the t-values calculated from  $p/p_0$ . The calculation of t(P) can be done with several different models, one example is the Harkins-Jura equation [86] (Equation 3.3). For a porous material, the curve will contain several domains with different slopes. At lower t values, the Y-intercept will provide information on the micropore volume, while at higher t values, the Y-intercept will yield the total porous volume [87].

$$t = \sqrt{\frac{13.99}{0.034 - \log(p/p_0)}} \quad (3.3)$$

### 3.5.2 X-ray diffraction

XRD is used to obtain information on the crystal structure of solids. It utilizes the scattering of radiation when it reaches a particle, such as an atom in a crystal lattice. The electrons around an atom scatter the X-rays elastically, i.e., without any energy loss. Constructive interference occurs when the scattered X-ray waves are in phase with each other due to the solid's ordered structure. This creates intensity maxima that can be detected at certain  $2\theta$  angles, depending on the material's crystal structure. According to Bragg's equation:

$$2d \sin\theta = n\lambda \quad (3.4)$$

Where n is an integer (often 1), d is the spacing between the atomic planes, and  $\lambda$  is the wavelength of the radiation ( $\lambda_{\text{Cu-K}\alpha} = 1.54 \text{ \AA}$ , for example). Using this relationship, it is possible to translate the angle of diffraction peaks into interplanar distances in the crystal lattice for the respective diffraction planes. Each diffraction peak's scattering intensity is related to the number of electrons in the scattering plane, making it possible to distinguish between materials with similar crystal structures but different chemical compositions.

For samples containing crystals of varying sizes (polycrystalline samples), such as powders, powder-XRD (PXRD) is used. Despite the crystals being of different sizes, constructive scattering occurs in diffraction cones, which can be recorded as a two-

dimensional diffraction pattern [88]. In modern PXRD instruments, it is possible to choose between recording 2D and 1D diffraction patterns.

### 3.5.3 X-ray fluorescence

X-ray fluorescence (XRF) is a non-destructive method, similar to XPS, that is used to obtain information on the elemental composition of a solid sample. However, it does not provide any information on the chemical state of the elements. XRF is not a surface technique, as the signal can be obtained from depths of several tenths of  $\mu\text{m}$  [89]. High-energy X-rays are targeted at the sample, exciting electrons in the inner electron orbitals of the atoms, causing electrons in the outer orbitals to delapse into the now vacant inner orbitals (Figure 3.5). The energy gap between the inner and outer electron causes a fluorescent photon to be emitted, which has a wavelength (= energy) characteristic for each element. The peak intensity in the XRF spectrum can be directly translated to the number of elements in the sample.

Several fluorescent electron transitions are possible for most elements, but the most probable one will give the strongest signal. This is the  $K\alpha$  transition, i.e.,  $L \rightarrow K$ , in physical terms, while the second most intense signal originates from the  $K\beta$  transition:  $M \rightarrow K$ , and so on.

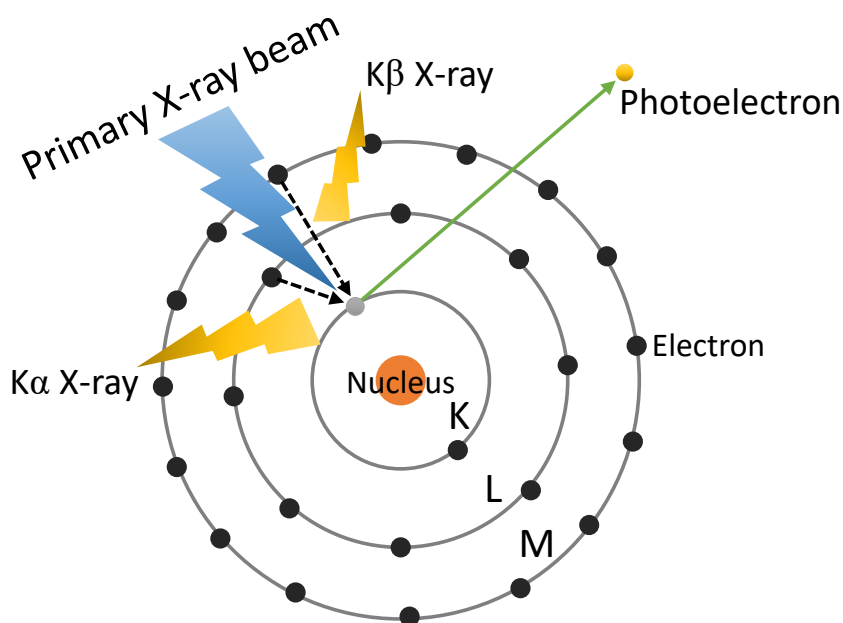


**Figure 3.5:** Schematic image of the generation of the  $K\alpha$  and  $K\beta$  X-ray radiation used in XRF analysis.

### 3.5.4 X-ray photoelectron spectroscopy

X-ray photoelectron spectroscopy (XPS) utilizes X-ray photons to excite electrons, creating so-called photoelectrons with kinetic energies specific to each element and

their respective electron shell. It is a surface technique, as the detectable photoelectrons are limited to the top  $\approx 20$  atomic layers. The Swedish physicist Kai Siegbahn earned the Nobel Prize in Physics in 1981 for his work in developing the XPS method [90, 91].

Since the exact bonding energy of an electron depends on the local environment (chemical state) around the atom, different oxidation states, nearby atoms, and bonding hybridizations can be distinguished by XPS [92]. There are two common types of scans used in XPS: Broad survey scan and high resolution scan. The former is useful for determining what elements are present in the sample, while the latter yields the chemical states for each element.

### 3.5.5 Zeta potential

A popular technique to determine surface charge is measuring the zeta potential (ZP, denoted  $\zeta$ ), which is the surface potential at the slip plane in the EDL. The exact location of the slip plane varies with surface potential, electrolyte concentration, and solvent composition, making it difficult to determine precisely. The ZP of a suspension of particles is measured by subjecting it to a voltage using two electrodes. This will induce electrophoresis and make the particle flow towards either the cathode or the anode, depending on their surface charge (Figure 3.6).

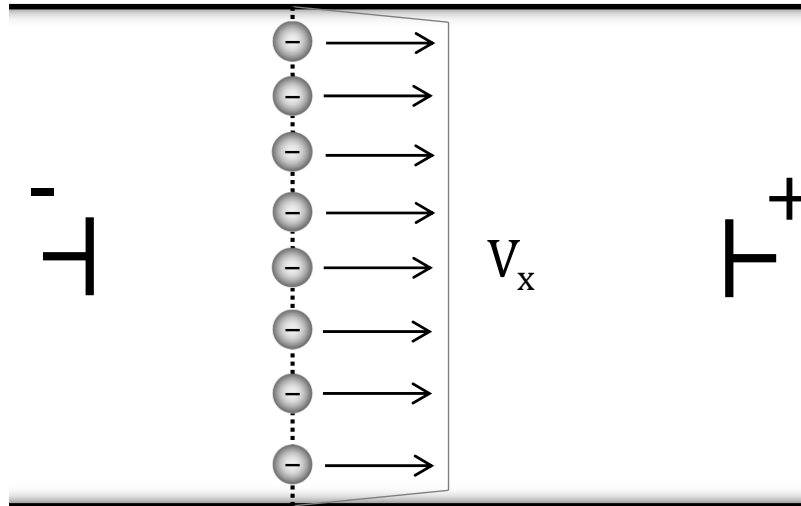


**Figure 3.6:** Demonstration of the electrophoretic movement of negatively charged particles towards a positively charged anode in a capillary.

If the velocity of the particles undergoing electrophoresis is monitored, the electrophoretic mobility ( $u_E$ ) can be determined, which is the particle velocity divided by the magnitude of the applied electric field strength (see eq. 3.5).

$$u_E = \frac{V_p}{E_x} \quad (3.5)$$

Note that the particle velocity ( $V_p$ ) does not always equal the measured particle velocity in the x direction ( $V_x$  in Figure 3.6). If the capillary walls are charged, i.e., a negative quartz capillary, counter-ions at the wall's surface will migrate towards the cathode or anode and drag fluid with them (electro-osmotic flow). Since the cell is a closed system, a back-pressure will be developed in the opposite direction. This will affect the net flow of the particles, depending on how far from the cell wall they are located. Nowadays, plastic ZP cells are often used, which eliminates this problem.

The ZP can be calculated using a suitable equation from the measured electrophoretic mobility. The ZP is often approximated to equal the Stern potential and can be considered a quantification of a colloidal system's stability; a large absolute value of ZP implies a large enough electrostatic repulsion to prevent aggregation. The equation below (eq. 3.6) shows the Helmholtz-Smoluchowski equation, which is used for systems where  $\kappa a > 200$ , i.e., for large particles ( $> 1 \mu\text{m}$  in diameter) in combination with ionic strengths of at least 1 mM.  $\epsilon$  and  $\epsilon_0$  are the relative dielectric permittivity and the vacuum permittivity, respectively, and  $\mu$  equals the viscosity of the solution.

$$u_E = \frac{\epsilon\epsilon_0\zeta}{\mu} \quad (3.6)$$

Another equation, for  $\kappa a$  values smaller than 0.1, to calculate ZP from electrophoretic mobility is the Hückel equation (eq. 3.7). This equation is suitable to use for nanoparticles and/or solutions with low ionic strengths.

$$u_E = \frac{2\epsilon\epsilon_0\zeta}{3\mu} \quad (3.7)$$

Note that only a constant of  $2/3$  has been added, corresponding to the difference in particle movement through the liquid medium. When the thickness of the double layer is small (large  $\kappa a$ ), retardation by counter-ions that want to move in the opposite direction to the particle is the major cause of movement resistance. In the case of a large double layer thickness (small  $\kappa a$ ), the resistance is dominated by the hydrodynamic friction force between the particle and the solvent [4]. To account for intermediate cases, Henry came up with a factor that is a function of  $\kappa a$ :  $C(\kappa a)$  (see eq. 3.8). An equation for this factor was given by Ohshima [93] (see eq. 3.9).

$$u_E = \frac{2}{3}C(\kappa a)\frac{\epsilon\epsilon_0\zeta}{\mu} \quad (3.8)$$

$$C(\kappa a) = 1 + \frac{1}{2} \left[ 1 + \frac{2.5}{\kappa a (1 + 2e^{-\kappa a})} \right]^{-3} \quad (3.9)$$

Electrokinetic titrations of a colloidal suspension involve measuring the ZP at various pH. As for the potentiometric titrations mentioned previously, a pH can be found where the measured net potential is zero. This yields the  $\text{pH}_{\text{IEP}}$  (IEP = isoelectric point). If the  $\text{pH}_{\text{IEP}}$  is indifferent to electrolyte concentration, no specific ion adsorption occurs. If it is shifted towards a higher value, there is specific adsorption of cations, and for lower values, of anions. In the case of an indifferent electrolyte, the  $\text{pH}_{\text{PZC}}$  and  $\text{pH}_{\text{IEP}}$  should coincide.

### 3.5.6 Inductively coupled plasma spectroscopy

Inductively coupled plasma optical emission spectroscopy (ICP-OES) is a detection technique for quantifying atomic concentrations in solution. It utilizes the emission of electromagnetic radiation of atoms after their excitation from the ground state to the excited state. The emitted radiation has a wavelength of 120-900 nm and is characteristic of each element. The lighter non-metals H, N, C, and O cannot be detected with this technique, and there is no way to determine an ion's oxidation state. ICP-OES typically has a limit of detection of 2 ppb, although the value is highly dependent on the element [94].

For a successful ICP-OES analysis, the following steps are required: Sample preparation, nebulization (liquid  $\rightarrow$  aerosol), volatilization (water evaporation), atomization (bond breaking, i.e., molecules  $\rightarrow$  atoms), excitation, emission, separation and subsequent detection of emission radiation. A plasma source is used for the atomization and excitation of the sample. The plasma itself is an ionized gas that carries no electrical charge and requires high temperatures (4000-8000 K) and an inert atmosphere (pure Ar or He) to prevent combustion.

## 3.6 Adsorption experiments

Two different sets of adsorption experiments were conducted: p-Cresol adsorption on AC and TiO<sub>2</sub>/AC composites in water and synthetic urine and the adsorption of the ions in SU on the same materials. The former was performed to investigate both the influence of the surface properties of the adsorbent on the odor capture capacity. The latter was to investigate whether the ions in SU prefer to adsorb to the surface or remain in solution.

### 3.6.1 p-Cresol adsorption

The adsorption of p-cresol was conducted using AC<sub>0</sub>, AC<sub>ox</sub>, AC<sub>0</sub>-T25, and AC<sub>ox</sub>-T25 as adsorbents at a mass concentration of 0.1 mg/mL and a total volume of 10 mL. 15 mL single-use Falcon tubes were used, and syringe filters (Nylon, 0.45 μm mesh size) were used to filter the suspensions after adsorption. Three p-cresol concentrations were used ( $C_e = 10, 25, 50$  ppm), in two different solvents (MQ water and SU), and at 37°C and 250 rpm. Each combination of adsorption tests was conducted in triplicate. At such low adsorbate concentrations, the adsorption is expected to be rapid, and therefore only one adsorption time was used: 1 h. This also ensures that the entire solution has a constant temperature of 37°C, the physiological temperature, and simulates the conditions if the adsorbent was to be integrated into a hygiene product.

For quantification, UV-vis spectroscopy at  $\lambda_{\max} = 277$  nm was used, and a scan between 210 and 310 nm was conducted for each sample to enable a correct background subtraction. Every data point from each UV-vis analysis was subtracted by the absorbance at 310 nm, as  $A_{\lambda_{310nm}} = 0$ . Response factors (RF) without adsorbent were used in each set of experiments to account for any loss of the volatile p-cresol during the 1 h adsorption and filtration. The linear range of the UV-vis quantification of p-cresol was found to be limited, so the samples had to be diluted to a final concentration of 1 to 10 ppm. Calibration curves were made in the same range. The adsorption tests in MQ water were performed without pH control, i.e.,  $\text{pH} = \text{pH}_0$ . Naturally, this leads to varying pH in the solutions (Table 3.4), as the adsorbents contain differing amounts of amphoteric surface groups.

### 3.6.2 Ion adsorption in synthetic urine

To further study the influence of the SU on the adsorption behavior of AC<sub>0</sub>, AC<sub>ox</sub>, AC<sub>0</sub>-T25, and AC<sub>ox</sub>-T25, adsorption tests similar to the odor adsorption experiments were performed, but without the p-cresol. Quantification of the ions remaining in solution after adsorption (1 h, 37°C, 250 rpm) was done using ICP-OES after dilution

### 3.6. ADSORPTION EXPERIMENTS

**Table 3.4:** Determined pH values post-adsorption and post-filtering in MQ water and synthetic urine at p-cresol concentrations 10, 25, and 50 ppm in MQ water and SU.

[p-Cresol] (ppm)	<u>Water</u>			
	$AC_0$	$AC_0$ -T25	$AC_{ox}$	$AC_{ox}$ -T25
10	6.03	5.99	5.75	5.18
25	5.91	5.52	5.26	4.89
50	5.86	6.13	5.26	5.05
[p-Cresol] (ppm)	<u>Synthetic urine</u>			
	$AC_0$	$AC_0$ -T25	$AC_{ox}$	$AC_{ox}$ -T25
10	6.08	5.99	6.08	5.99
25	6.08	6.00	6.08	6.00
50	6.10	6.00	6.08	5.98

by 100. The dilutions were performed by adding 0.1 mL of analyte solution to 6.4 mL of 0.5 M HCl containing 2 ppm Yttrium standard and 3.5 mL HNO<sub>3</sub>. A calibration curve was done with ion concentrations of 10, 25, and 50 ppm for all ions except Na<sup>+</sup>, which had twice the concentration (20, 50, 100 ppm). The composition of the SU is shown in Table 3.5, and was obtained from Sarigul et al. (2019) [62]. Not all ions were detectable by the method; only Na<sup>+</sup>, K<sup>+</sup>, Mg<sup>2+</sup>, Ca<sup>2+</sup>, and PO<sub>4</sub><sup>3-</sup> could be accurately quantified by ICP-OES.

**Table 3.5:** The concentration of salts of the synthetic urine used in the adsorption experiments.

Salt	Concentration (mM)	Mass concentration (ppm)
Na <sub>2</sub> SO <sub>4</sub>	12.0	1700
Urea	250	15000
KCl	31.0	2310
NaCl	30.0	1760
CaCl <sub>2</sub>	1.66	184
NH <sub>4</sub> Cl	23.7	1290
MgSO <sub>4</sub> *7H <sub>2</sub> O	4.39	528
NaH <sub>2</sub> PO <sub>4</sub> *H <sub>2</sub> O	18.7	2910
Na <sub>2</sub> HPO <sub>4</sub>	4.67	831

### 3.7 Principal component analysis

PCA is a type of multivariate statistics that is readily used to find correlations between observables in large data sets. This is done by formulating new variables ("principal components",  $z_1, z_2, \dots, z_m$ ) from the original variables ( $x_1, x_2, \dots, x_p$ ) by using linear functions of  $x$  ( $\alpha_1, \alpha_2, \dots, \alpha_p$ ), as shown in Equation 3.10. This reduces the amount of data to analyze as only a few PCs are required to describe the variance in data [95].

$$z = \alpha_1 x_1 + \alpha_2 x_2 + \dots + \alpha_p x_p \quad (3.10)$$

By the design of the PCs, they are all uncorrelated and perpendicular to each other. PC1 contains the most amount variance and is, therefore, the best fit for all original variables. To correct the difference in units between the observables, they are all standardized by subtracting the mean and division of the standard deviation, yielding  $z$  values between -1 and +1. The new variables form a correlation matrix to describe their correlations to each other, from which eigenvectors are extracted for each variable-PC combination. The eigenvectors are used to make loading plots with the relevant PCs on the axes. In the loading plots, variables grouped together are considered highly correlated. PCA was performed using the OriginPro<sup>®</sup> v9.70 software from OriginLab [96]

### 3.8 Molecular dynamics

Molecular dynamics (MD) simulations is a method used to study interactions on an atomistic scale. In this work, it was used to study the adsorption of p-cresol on graphene and graphene oxide sheets, as well as the interactions of ions and urea with each other and the graphene (Figure 3.7 (A)). By adding 8 hydroxyl groups, 6 epoxy groups, and 10 carboxyl groups to the graphene, it is transformed into graphene oxide (GO, Figure 3.7 (B)), which is a surface more similar to the activated carbons used in the adsorption studies described in Section 3.6. To ensure the correct p-cresol, urea, and ion concentrations in the simulation box, the following number of molecules/ions were used: 3 p-cresols, 3 urea, 2  $\text{NH}_4$ , 2  $\text{PO}_4^{3-}$ , 2  $\text{SO}_4^{2-}$ , 7  $\text{Na}^+$ , 4  $\text{K}^+$ , 2  $\text{Ca}^{2+}$ , 3  $\text{Mg}^{2+}$ , and 13  $\text{Cl}^-$ .

Figure 3.7 shows the full setup of the MD simulations, including an example of a unit cell containing p-cresol, urea, and the ions in SU (Table 3.5). The dimensions of the graphene and GO sheets were  $1.7 \times 1.3 \text{ nm}^2$  and the unit cell dimension was  $4 \times 4 \times 4 \text{ nm}^3$ . The sheets were fixed in position in the middle of the box, but only the carbon atoms were position-estrained; the oxygen-containing functional groups could freely follow the dynamics of the system. Water as a solvent was included in

the simulations by using the TIP4P water model [97]. Periodic boundary conditions were used to make an "infinite" system with no interference from the simulation box walls. GROMACS 2021.5 [98] was used for the MD simulations with CHARMM force fields [99]. To generate the structural coordinated and topologies, CHARMM-GUI [100, 101] was used.

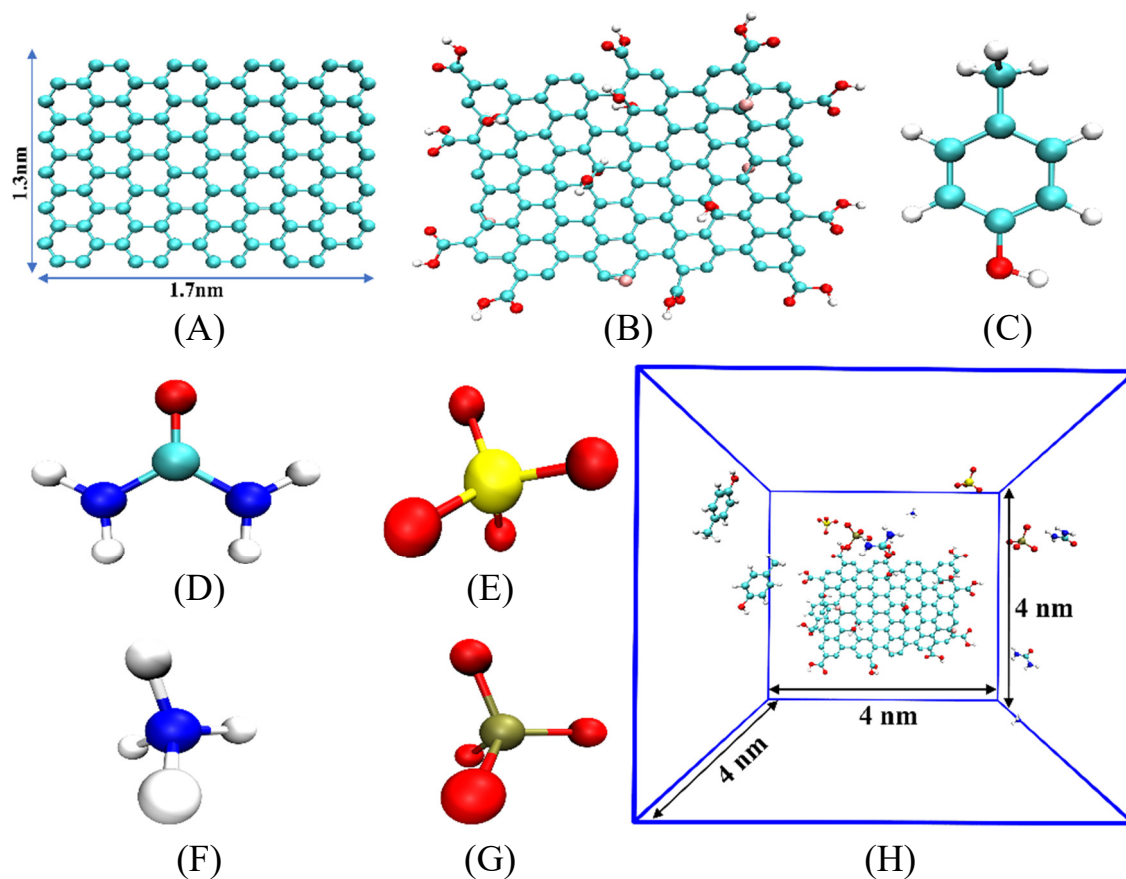


**Figure 3.7:** Experimental setup of the MD simulations: (A) Bare graphene sheet, (B) Graphene oxide functionalized with hydroxyl and carboxyl groups, (C) p-cresol, (D) urea, (E) sulfate ion, (F) ammonium ion, (G) phosphate ion, (H) the unit cell used, showing all chemical species included except for water.

# Chapter 4

## Summary of Papers

This chapter is divided into sections summarizing the most relevant results of each paper separately. In paper I, potentiometric titrations and gel-time determinations were used to investigate the co-ion (anionic) effect on the surface charge and gelling of silica nanoparticles. Paper II presents the results of the iron(III) TPA MOF synthesis experiments, with the aim to use the largest surface area product as an odor adsorbent. The TiO<sub>2</sub> grafting on AC to make composite materials and their use as adsorption materials for p-cresol are included in paper III. The counter-ion effect on the surface charge development of sulphate-functionalized nanocellulose was investigated by potentiometric titrations, and the results are presented in Paper IV. Finally, paper V shows the results from the molecular dynamics simulations of synthetic urine solutions to examine the effect of the ions and urea on the adsorption of p-cresol on bare and oxygen-functionalized graphene nanosheets.

## 4.1 Paper I: The co-ion effect on the surface charge and gelling of silica nanoparticles

The main finding of the first article was the unexpected influence of the anions on the surface charge density and gel-times of silica nanoparticles. The SCD curves (Figure 4.1) revealed that the silica surface is negatively charged above pH 4 and that the SCD of silica increased in the order:  $\text{Na}_2\text{SO}_4 < \text{NaNO}_3 < \text{NaCl}$ . For the counter-ions, the SCDs followed the Hofmeister series, i.e.,  $\text{NaCl} < \text{KCl}$ .

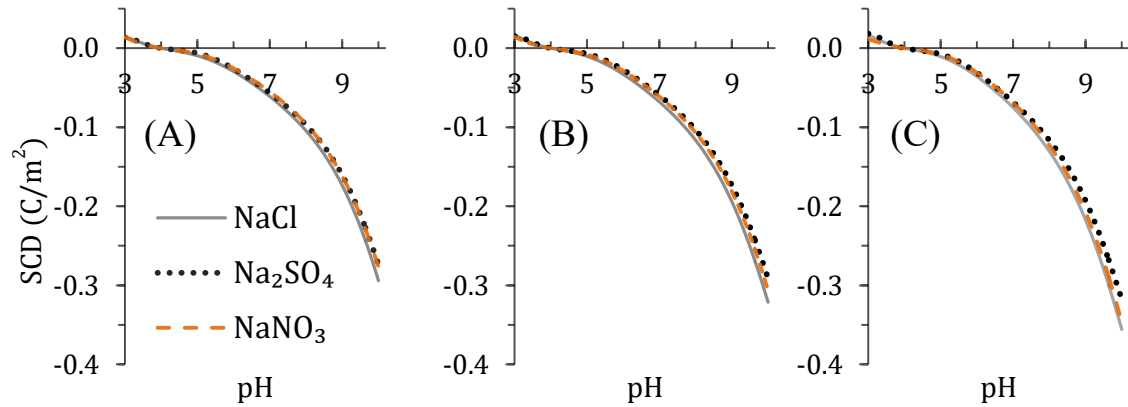


**Figure 4.1:** SCD curves of 2 wt% silica at salt concentrations (with respect to the cation) of (A) 0.05 M, (B) 0.10 M, (C) 0.20 M. Reprinted from Paper I [18] with permission from Elsevier.

The gel-times showed a significant influence of the co-ion (Figure 4.2). The fastest gelling was induced by NaCl; at the lowest cation concentration (0.235 M), the gelling took less than 300 minutes, while for  $\text{Na}_2\text{SO}_4$ , no gelling was observed within 24 h at the same concentration.

The results of this study were explained by the mean ionic activity coefficients ( $\gamma_{\pm}$ ) of the salt solutions as reported in the literature (Figure 4.3). The chloride salts show the typical behavior of dissociated salts, i.e., activity coefficients bend upward at increasing salt concentrations showing that ion-ion repulsions dominate and the cations and anions are fully dissociated in water even at high concentrations. The curves for the nitrate salts clearly decline, showing the opposite effect, i.e., the formation of ion-pairs as the salt concentration increases.

Figure 4.4 compares the experimental (solid lines) and the calculated (filled circles) mean ion activity coefficients of some chloride, chlorate, and sulfate salts. For the chlorides and chlorates, the experimental values correspond well with the calculated values. The values for the sulfate salts agree less, but show the same trend as the nitrate salts in Figure 4.3; that the ion-pairing effect is significant. The calculated values were obtained by Monte-Carlo (MC) simulations (some of them from Abbas et al. (2009) [6]), and the experimental values were from Hamer & Wu (1972)

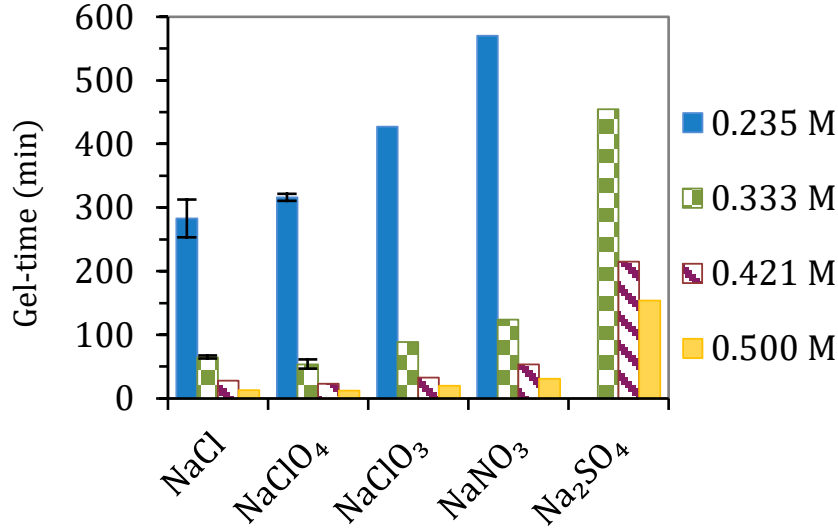


**Figure 4.2:** Gel-times of silica nanoparticles at 24-38 wt% and pH 8.2-8.8, depending on salt concentration. The given concentrations are with respect to the cation concentration. Standard deviations are given for NaCl and NaClO<sub>4</sub> to demonstrate the repeatability of the results. *Reprinted from Paper I [18] with permission from Elsevier.*

[102] and Goldberg (1981) [103].

In the MC simulations, the anion radius was kept at its crystallographic value, whereas the cation radius was adjusted to fit the experimental data. The fitted cation radii found by MC are in agreement with the theories of ion hydration; that is, small, highly charged ions are strongly hydrated compared to large, weakly hydrated ions. Therefore, the activity coefficients of strongly hydrated chloride salts, such as LiCl, are much higher compared to the weakly hydrated KCl. The cation hydration, in turn, determines the gel-time of the suspended silica particles. The extremely long gel-time in Na<sub>2</sub>SO<sub>4</sub> can be linked to the strong ion-pairing in this salt. The strong ion-pairing results in few counter-ions available for screening the silica surface charge compared to NaCl at the same concentration.

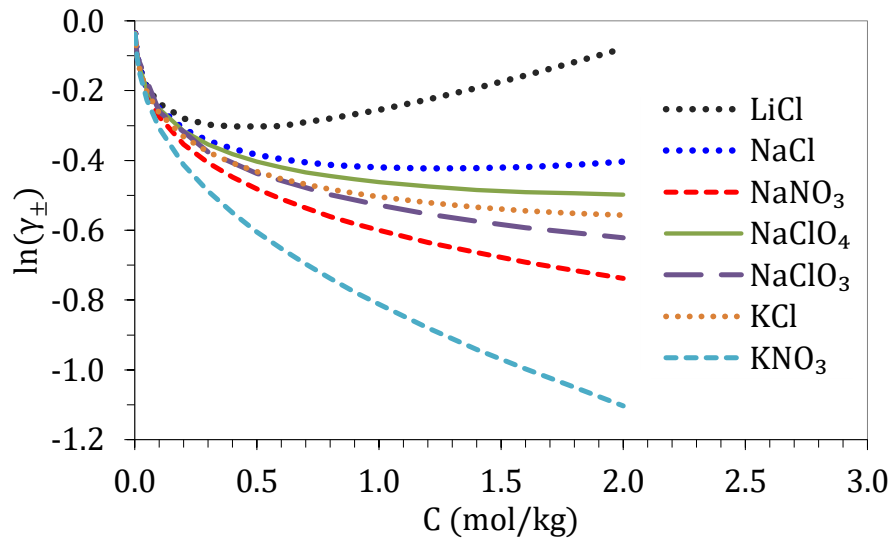


**Figure 4.3:** Experimental data of the natural logarithm of the mean ion-activity coefficients of different salts as a function of molality.

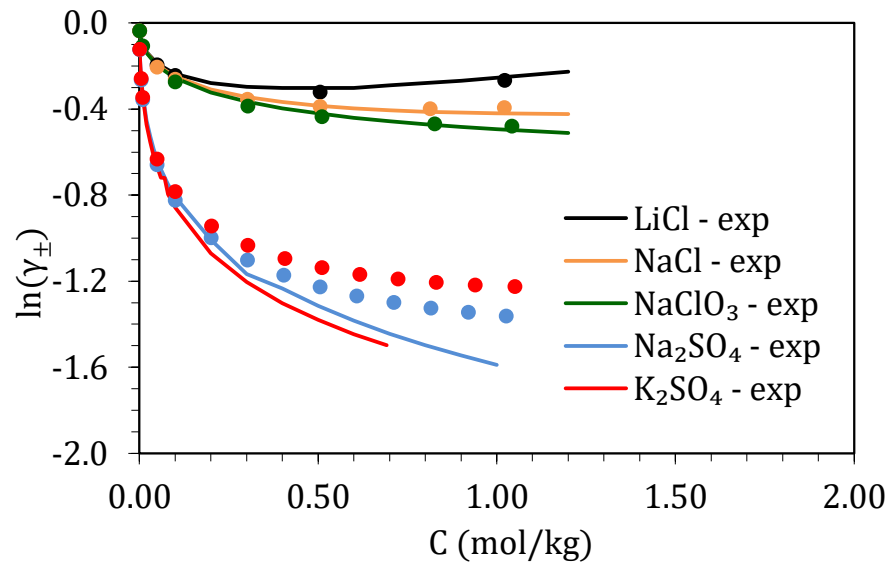


**Figure 4.4:** Calculated (filled circles) and experimental (solid lines) data of the natural logarithm of the mean ion-activity coefficients of different salts as a function of molality.

## 4.2 Paper II: Fe(III) TPA MOF synthesis

The extensive MOF synthesis work revealed that, when performing solvothermal synthesis of Fe(III) TPA MOFs, one single product is rarely formed. Instead, a mixture of MOF-235 and MIL-101 is formed. The former can be identified due to only having a strong diffraction peak in the 5-10°  $2\theta$  region (Figure 4.5) and a smaller surface area than the latter. The sources cited in Tables 3.1 and 3.2 display a large variation in measured surface area of their claimed phase-pure MOFs. For the standard solvothermal MOF-235 synthesis (3:5 Fe(III):TPA, 1:1 DMF:EtOH, 80°C, 24 h), the difference between the smallest (9.6 m<sup>2</sup>/g [66]) and largest (918 m<sup>2</sup>/g [70])  $S_{\text{BET}}$  presented is almost by a factor of 100. For MIL-101, the difference is not as dramatic: 601 m<sup>2</sup>/g [77] vs. 3200 m<sup>2</sup>/g [74], i.e., a factor of 5.3. Depending on the XRD analysis settings and data post-treatment, the diffraction peaks of MIL-101 and MOF-235 can be difficult to distinguish, especially the peaks at 9.0 and 9.4°. Both the fluorescence signal from iron and the background from the primary beam X-rays can conceal the MIL-101 peaks at lower  $2\theta$  angles.

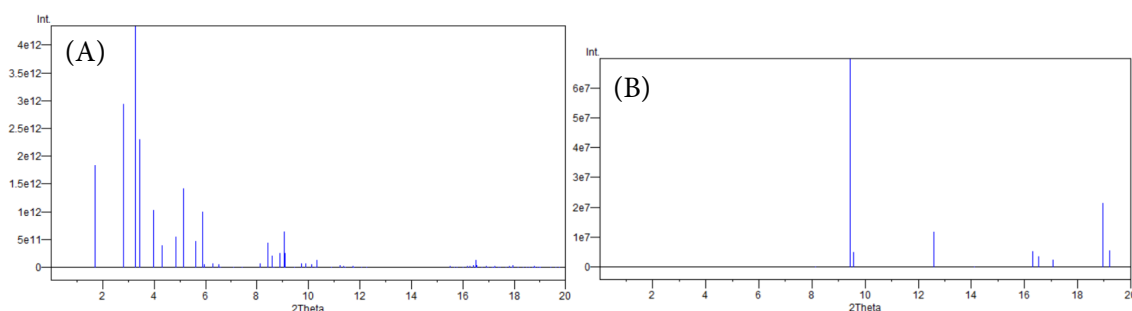


**Figure 4.5:** Diffraction pattern references of (A) MIL-101 [46] and (B) MOF-235 [40]. The graphs were made using the VESTA software [104] from the references' crystallographic information files.

Figure 4.6 shows the XRD peak height ratios of the MOF-235 peak at 9.4° and the MIL-101 peak at 9.0° for the synthesis products in Table 3.3. At a 1:1 DMF:EtOH solvent ratio, the main phase is usually MOF-235. Larger DMF:EtOH ratios lead to MIL-101 being the major product. It seems like a stoichiometric Fe(III):TPA ratio, i.e., 5:3, used in the ns2.X syntheses, favors a more phase-pure product.

It is clear that there is a distinct correlation between the surface areas and the MOF-235:MIL-101 ratios of the formed products (Figure 4.7). The lower MOF-235:MIL-101 ratio is, the larger the surface area. MOF-235 has got a smaller surface area due to its 2D channels, while MIL-101 has got a significantly larger surface area with its 3D cage-like pores. Another consequence of this is that the channels of MOF-235 are more easily clogged which limits the measured surface area.

The *in-situ* MAXS analyses (Figure 4.8) revealed the temperature-dependence

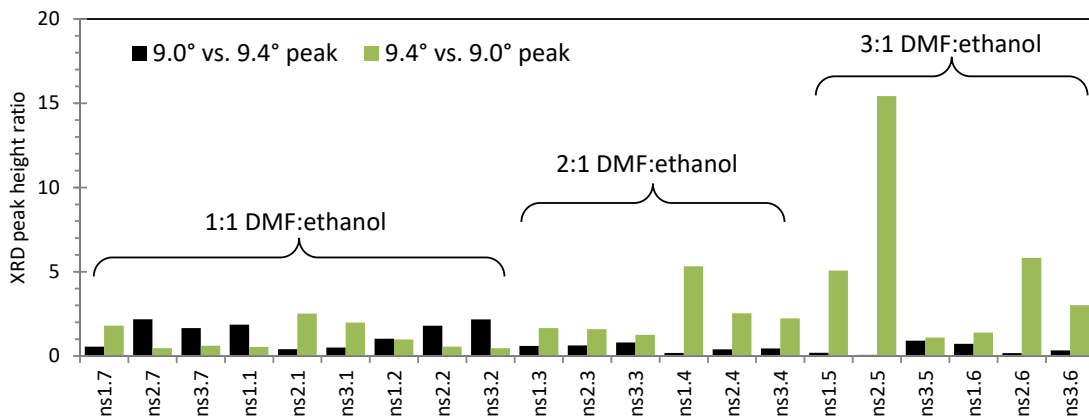


**Figure 4.6:** XRD peak height ratios of the synthesis products from Paper II.

of the MOF crystallization during the solvothermal synthesis; at 80°C, MOF-235 is formed, and at 85°C, MIL-101 is formed. The crystallization for both MOFs start after approximately 6 h. For MOF-235, the crystallization appears to occur in an inconsistent manner, since the intensity of the 9.4° peak changes seemingly arbitrarily. The MIL-101 phase, on the other hand, is formed rapidly in the initial stage, after which the overall peak intensity slowly increases with time during the entire analysis duration.

Another way to study the crystallization process of MOFs is through *ex-situ* XRD analyses (Figures 4.9 and 4.10). For the 1:1 DMF:etOH synthesis, using a conventional reagent ratio (ns3.2) yielded the least amount of crystalline product with the smallest surface area (Table 4.1). The two other reagent ratios yielded similar XRD patterns and surface areas. No strong MOF-235 diffraction peaks at 9.4° could be seen in any of the products, including the ones from the 3:1 DMF:etOH solvent

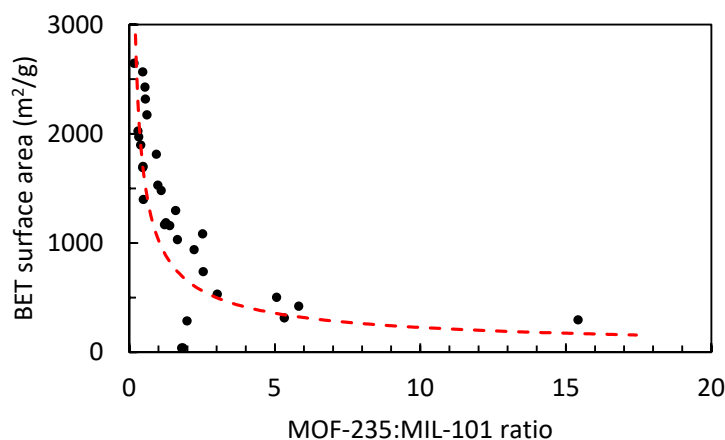


**Figure 4.7:** The relationship between  $SA_{\text{BET}}$  and XRD peak height ratio (MOF-235:MIL-101) of the synthesis products.

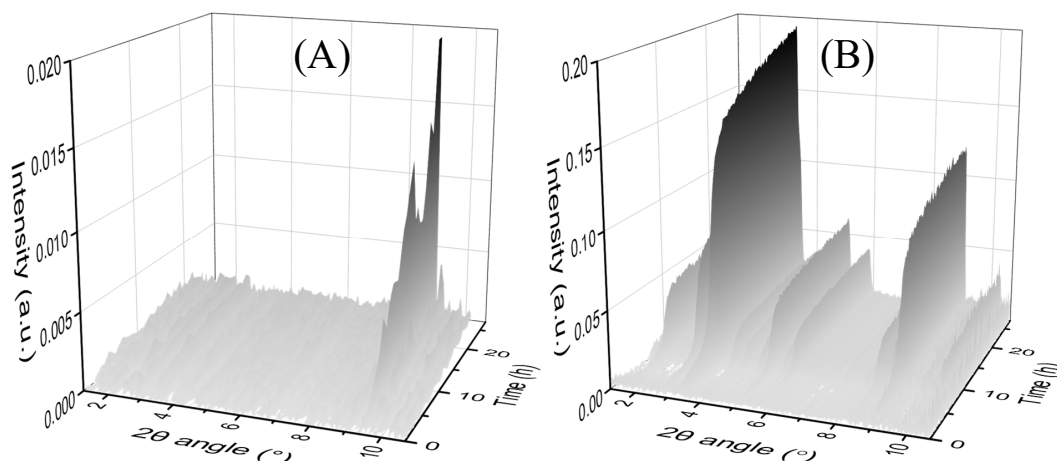


**Figure 4.8:** Results from the time-resolved *in-situ* MAXS analyses of the solvothermal synthesis with a 1:1 DMF:EtOH ratio and a 5:3 Fe(III):TPA ratio at (A) 80°C and (B) 85°C.

ratios, which produced a significant MOF-235 yield in the conventional syntheses. Unexpectedly, for ns1.2 and ns3.2, the surface areas decrease between 6 and 12 h. A similar occurrence was observed for the MOF-235 phase in the *in-situ* experiments (Figure 4.8), indicating a non-linear crystal growth of both MOF-235 and MIL-101 during their respective solvothermal synthesis. A potential cause for this could be the dissolution and subsequent recrystallization of the MOFs, i.e., Ostwald ripening. When extracting the MOF dispersion after 6, 12, and 24 h, the solvothermal treatment was temporarily stopped, and the vessels were opened. Since no MOF-235 peaks were detected with XRD, it could be hypothesized that the pressure buildup in the synthesis vessel is an important factor for MOF-235 to form.

It is known that the DMF decomposes into the Brønsted base dimethylamine (DMA) and carbon monoxide when heated [105]. The DMA is required for the linker molecule TPA to get deprotonated and bind to Fe(III) to form the MOFs. DMA has got a boiling point of 7°C [106], making it highly volatile. Since the first extraction is done before the MOF crystallization has been finalized, there is the risk of releasing the essential DMA molecules into the atmosphere when opening the vessel.

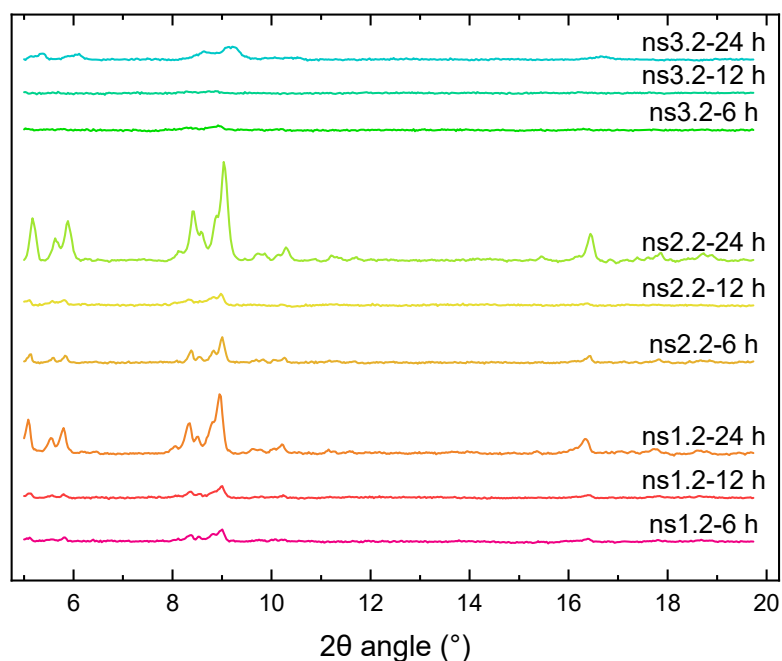


**Figure 4.9:** Results from the time-resolved *ex-situ* XRD analyses of the solvothermal syntheses with a 1:1 DMF:EtOH ratio and Fe(III):TPA ratios of 1:1 (ns1.2), 4:3 (ns2.2), and 3:5 (ns3.2).

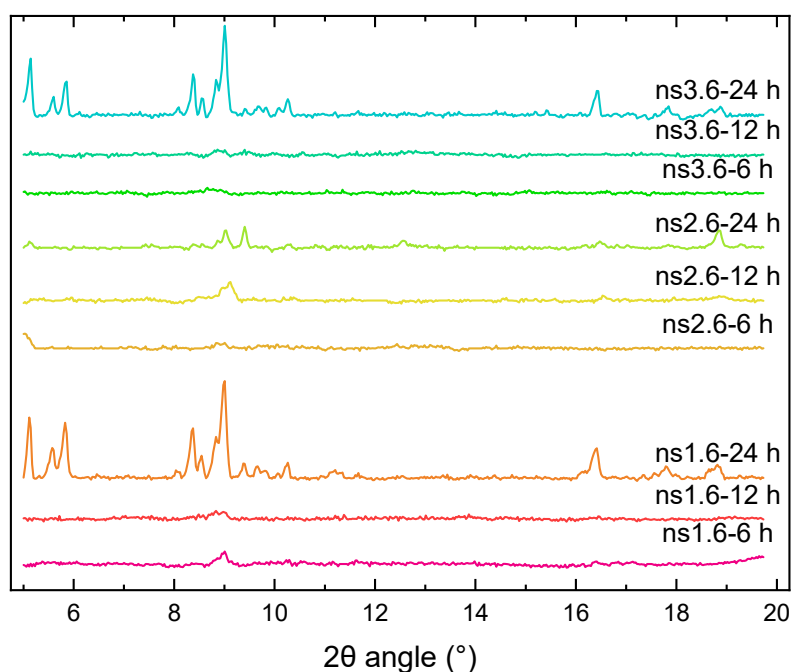


**Figure 4.10:** Results from the time-resolved *ex-situ* XRD analyses of the solvothermal syntheses with a 3:1 DMF:EtOH ratio and Fe(III):TPA ratios of 1:1 (ns1.6), 4:3 (ns2.6), and 3:5 (ns3.6).

**Table 4.1:** BET surface areas of the *ex-situ* MOF synthesis products.

<b>Product</b>	<b>SA<sub>BET</sub> (m<sup>2</sup>/g)</b>
ns3.2-24 h	1870
ns3.2-12 h	460
ns3.2-6 h	620
ns2.2-24 h	3280
ns2.2-12 h	2020
ns2.2-6 h	1640
ns1.2-24 h	3290
ns1.2-12 h	600
ns1.2-6 h	1140
ns3.6-24 h	510
ns3.6-12 h	507
ns3.6-6 h	1105
ns2.6-24 h	305
ns2.6-12 h	462
ns2.6-6 h	387
ns1.6-24 h	444
ns1.6-12 h	493
ns1.6-6 h	405

## 4.3 Paper III: p-Cresol adsorption on TiO<sub>2</sub>/AC composites

### 4.3.1 Material characterization

The commercial activated carbon, AC<sub>0</sub>, was successfully oxidized to AC<sub>ox</sub> by the HNO<sub>3</sub> treatment, as proven by the change in the surface properties of the AC. Both the mass titrations (Figure 4.11) and the ZP measurements (Figure 4.12) revealed that the oxidation of AC<sub>0</sub> to AC<sub>ox</sub> significantly increases the surface acidity of the material. The TiO<sub>2</sub> grafting altered the surface charge of the AC, as the ZP of the composites become positive below pH  $\approx$  4.5.

There is a clear discrepancy between the pH<sub>IEP</sub> and pH<sub>PZC</sub> of the AC<sub>0</sub> and AC<sub>ox</sub> materials (Table 4.2), indicating the interaction of potential-determining ions at the surface. The pH<sub>IEP</sub> is determined by acid and base additions, and the pH is adjusted by adding HNO<sub>3</sub> or NaOH. Therefore, either Na<sup>+</sup> or NO<sub>3</sub><sup>-</sup> can adsorb at the surface of the AC, depending on its charge. This specific adsorption of ions changes the measured values of the ZP. For AC<sub>0</sub>, the pH<sub>IEP</sub> < pH<sub>PZC</sub> due to NO<sub>3</sub><sup>-</sup> ions adsorbing to the positively charged surface when pH < pH<sub>PZC</sub>.

Since the ZP is determined at a distance from the external surface, any ions

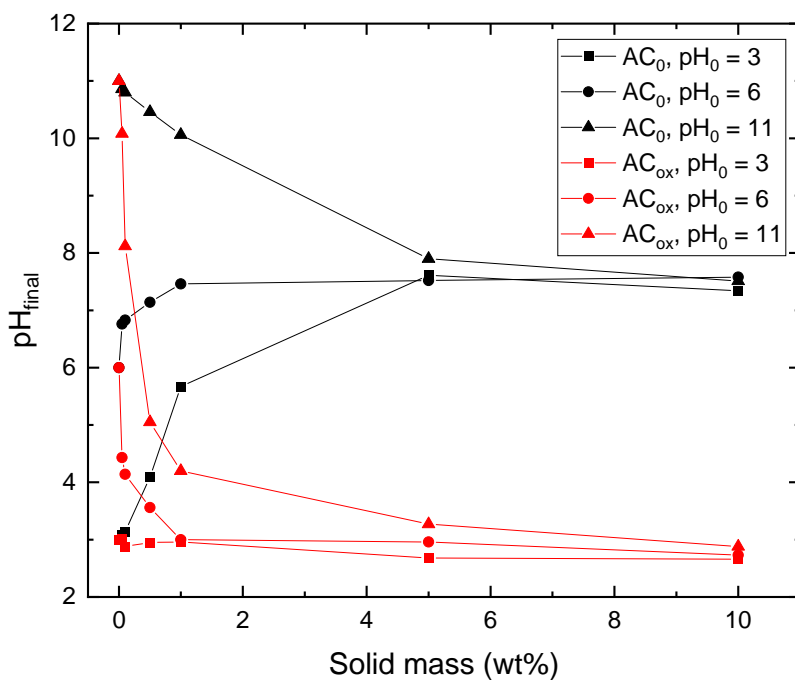


**Figure 4.11:** Mass titrations of AC<sub>0</sub> and AC<sub>ox</sub> with the final pH on the Y axis and AC mass concentration on the X axis.

located between the actual surface and the slip plane will affect the value of the ZP. It can therefore be considered that the  $\text{pH}_{\text{PZC}}$  is a more accurate representation of a charged surface's "zero-point". However, to obtain information on how the charge varies with pH, ZP measurements tend to be more convenient as it requires significantly less material and is over-all a more rapid method than potentiometric titrations, for example. Porous materials are notoriously difficult to perform potentiometric titrations on, since the large number of surface groups contribute to extensive pH buffering and the equilibration time after each acid and base addition can be several hours.

Both  $\text{AC}_0$  and  $\text{AC}_{\text{ox}}$  were grafted with  $\text{TiO}_2$  crystals using titanium(IV) tetraisopropoxide in isopropanol at room temperature (Section 3.4.2). According to the ZP measurements (colored symbols in Figure 4.12), the implementation of  $\text{TiO}_2$  crystals on the AC surface changes the electrostatic properties of the material. At acidic pH, the ZP is now positive for all composites as a result of the  $\text{TiO}_2$  grafting, as it has got a higher  $\text{pH}_{\text{IEP}}$  ( $\approx 5$ ) [107, 108] than the ACs.

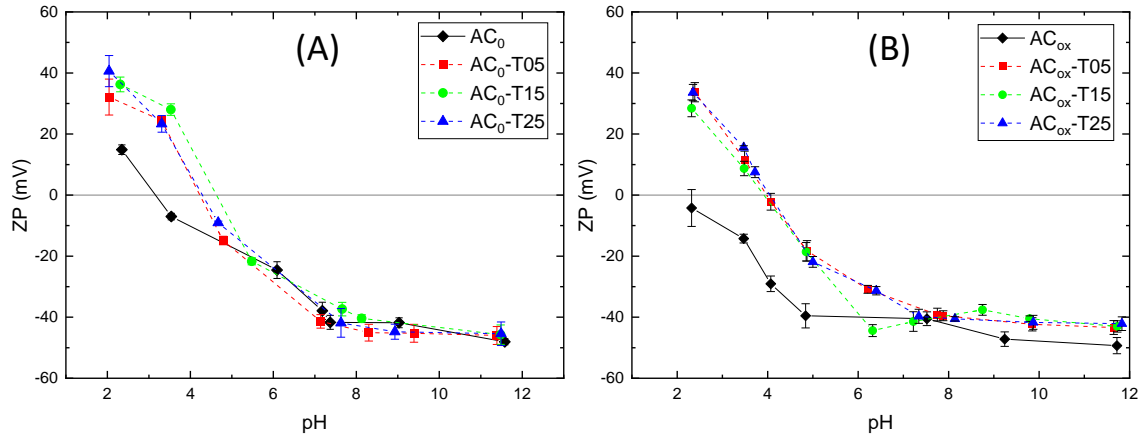


**Figure 4.12:** Zeta potentials as a function of pH of (A)  $\text{AC}_0$ , (B)  $\text{AC}_{\text{ox}}$ , and their respective  $\text{TiO}_2/\text{AC}$  composites.

**Table 4.2:** Estimated  $\text{pH}_{\text{IEP}}$  and  $\text{pH}_{\text{PZC}}$  of  $\text{AC}_0$ ,  $\text{AC}_{\text{ox}}$ , and their respective  $\text{TiO}_2$  composites.

Material	$\text{pH}_{\text{IEP}}$	$\text{pH}_{\text{PZC}}$
$\text{AC}_0$	3.5	7.5
$\text{AC}_0\text{-T05}$	4.2	-
$\text{AC}_0\text{-T15}$	4.6	-
$\text{AC}_0\text{-T25}$	4.2	4.7
$\text{AC}_{\text{ox}}$	< 2	2.8
$\text{AC}_{\text{ox}}\text{-T05}$	4.2	-
$\text{AC}_{\text{ox}}\text{-T15}$	4.2	-
$\text{AC}_{\text{ox}}\text{-T25}$	4.2	3.5

For the TiO<sub>2</sub>/AC composites, the grafting efficiency increases with increasing TTIP precursor vol% during the chemical treatment of AC at room temperature. This is evident when looking at the results from the elemental analyses performed using the XPS (Table 4.3) and XRF (Table 4.4) techniques. According to the XPS results, the Ti content saturates around 11-12 and 13-14 at% for the AC<sub>0</sub> and AC<sub>ox</sub> composites, respectively. However, the XRF analyses show that the wt% of Ti in the samples fairly consistently increases with TTIP concentration. There is a clear distinction between the two methods: XPS only penetrates the sample a few nm, i.e., it is a surface analysis technique, while the XRF technique analyses significantly more of the sample. It is not possible to compare the absolute values obtained by XRF and XPS with each other, as they have different lower limitations on the weight of the element that may be quantified. XRF can only detect sodium and heavier elements, while XPS detects all elements except hydrogen and helium. Yet, the results indicate that the external surface of the AC has a maximum capacity of TiO<sub>2</sub> crystals, and when the TTIP vol% is increased, the additional TiO<sub>2</sub> crystals are located inside of the AC pores.

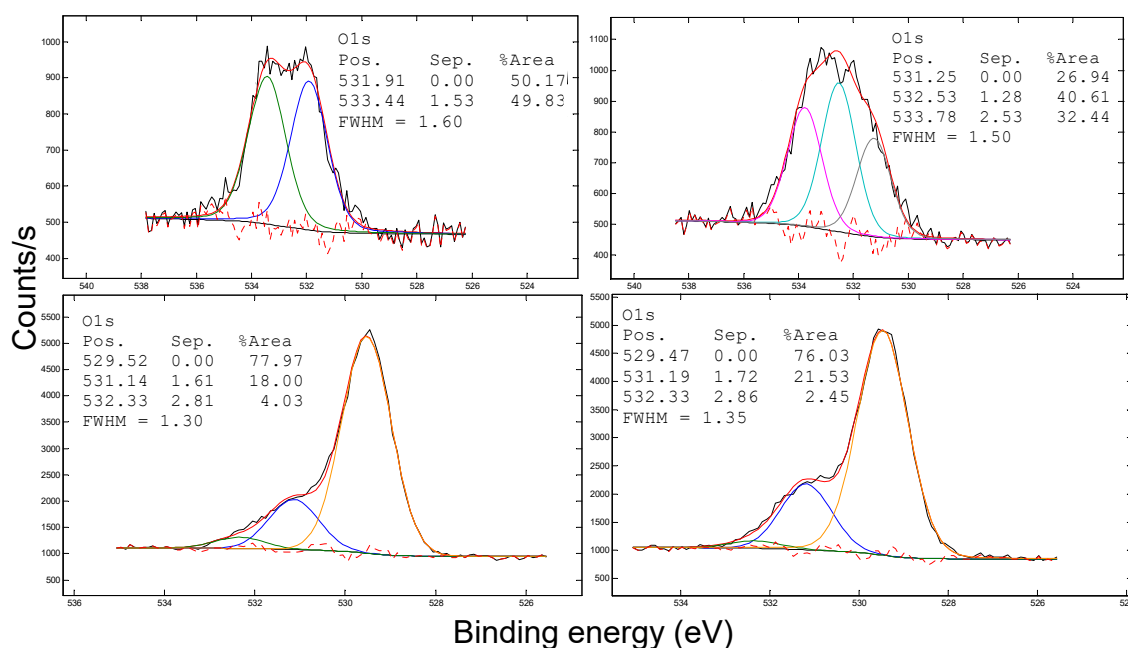


**Figure 4.13:** High-resolution XPS spectra of O 1s of (A) AC<sub>0</sub>, (B) AC<sub>ox</sub>, (C) AC<sub>0</sub>-T25, (D) AC<sub>ox</sub>-T25.

The grafting of TiO<sub>2</sub> on the surface of AC was found to be more efficient on AC<sub>ox</sub> than AC<sub>0</sub>, most likely due to the presence of more oxygen-containing surface groups on AC<sub>ox</sub>. This increases both the acidity, as seen by the surface charge experiments, and the hydrophilicity of the surface. A simple way to determine the hydrophilicity and hydrophobicity of a surface is through water contact angles (Figure 4.14). Both the HNO<sub>3</sub> oxidation and the TiO<sub>2</sub> grafting significantly decreases the water wetting

**Table 4.3:** XPS elemental content of AC<sub>0</sub>, AC<sub>ox</sub>, and their respective TiO<sub>2</sub> composites.

Sample	C (at%)	O (at%)	Ti (at%)
AC <sub>0</sub>	93	7.0	0.0
AC <sub>0</sub> -T05	78	18	4.5
AC <sub>0</sub> -T15	49	40	12
AC <sub>0</sub> -T25	56	33	11
AC <sub>ox</sub>	91	9.0	0.0
AC <sub>ox</sub> -T05	77	19	4.0
AC <sub>ox</sub> -T15	40	46	14
AC <sub>ox</sub> -T25	45	42	13

**Table 4.4:** XRF Ti content of the TiO<sub>2</sub>/AC composites.

Sample	Ti (wt%)
AC <sub>0</sub> -T05	11
AC <sub>0</sub> -T15	15
AC <sub>0</sub> -T25	18
AC <sub>ox</sub> -T05	9.3
AC <sub>ox</sub> -T15	18
AC <sub>ox</sub> -T25	23

angle of the AC. The smallest wetting angle was obtained by AC<sub>ox</sub>-T25, showing that it is strongly hydrophilic.

The XRD patterns of the AC<sub>0</sub>-T25 and AC<sub>ox</sub>-T25 (Figure 4.15) show strong and broad peaks around 25 and 44° from the graphite backbone in the activated carbon. The strong peak at 27° corresponds to the (1 1 0) plane of rutile TiO<sub>2</sub>, and the smaller peak at 42° originates from the (1 1 1) plane of the same crystal phase [109]. The reference from which the grafting procedure was taken[37], had a similar sharp peak near 26°, but the second most intense peak was at 38°, indicating that they had obtained the anatase phase on their activated carbon fibers (ACF). The differences between the two procedures were the AC and possibly the ultrasonication method. The reference used fibers with a larger surface area (1221 m<sup>2</sup>/g) than the powdered AC used in this study. The pore volume of the ACF was 0.52 cm<sup>3</sup>/g (as calculated by density functional theory from the N<sub>2</sub> isotherm), compared to 0.71 and 0.61 cm<sup>3</sup>/g for AC<sub>0</sub> and AC<sub>ox</sub> (using the BJH desorption method), respectively. This indicates that the ACF contains larger pores, possibly affecting whether anatase or rutile is the most stable phase of TiO<sub>2</sub>. The reference does not mention what kind of ultrasonicator that was used in their experiments, e.g., probe type and effect/amplitude. It was also not explained exactly how the calcination by ultrasonication was performed, only that it was done in water.

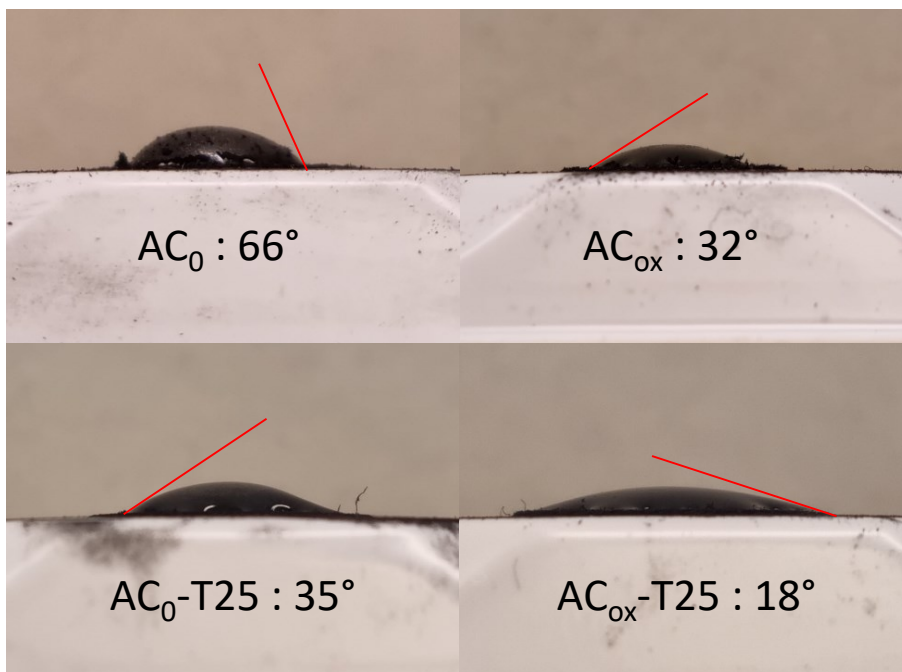


**Figure 4.14:** Water droplet contact angles of AC<sub>0</sub>, AC<sub>ox</sub>, AC<sub>0</sub>-T25, and AC<sub>ox</sub>-T25.

The surface area measurements revealed that mainly the internal area decreased, i.e., the micropore SA, upon TiO<sub>2</sub> grafting (Figure 4.16 and Table 4.5). This is probably due to pore blockage by TiO<sub>2</sub> crystals, either at the entrance of the pores or inside of them. The ultrasonication treatment slightly increased the SA by removing some of the TiO<sub>2</sub> crystals blocking the pores and washing away residual TTIP by-products from the grafting procedure [110]. The oxidation of AC<sub>0</sub> to AC<sub>ox</sub> also decreased the SA, which is a well-known effect of the formation of oxygen-containing chemical groups on the surface, which can be pore-blocking [111].

The SEM images of the materials (Figures 4.17 and 4.18) confirmed that the

**Table 4.5:** Surface areas and pore volumes of AC<sub>0</sub>, AC<sub>ox</sub>, and their TiO<sub>2</sub>/AC composites, obtained from N<sub>2</sub> adsorption isotherms.

Sample	BET surface area (m <sup>2</sup> /g)	BJH adsorption pore volume (cm <sup>3</sup> /g)
AC <sub>0</sub>	897	0.712
AC <sub>0</sub> -T05	843	0.641
AC <sub>0</sub> -T15	817	0.618
AC <sub>0</sub> -T25	750	0.559
AC <sub>ox</sub>	795	0.614
AC <sub>ox</sub> -T05	682	0.532
AC <sub>ox</sub> -T15	663	0.502
AC <sub>ox</sub> -T25	660	0.486

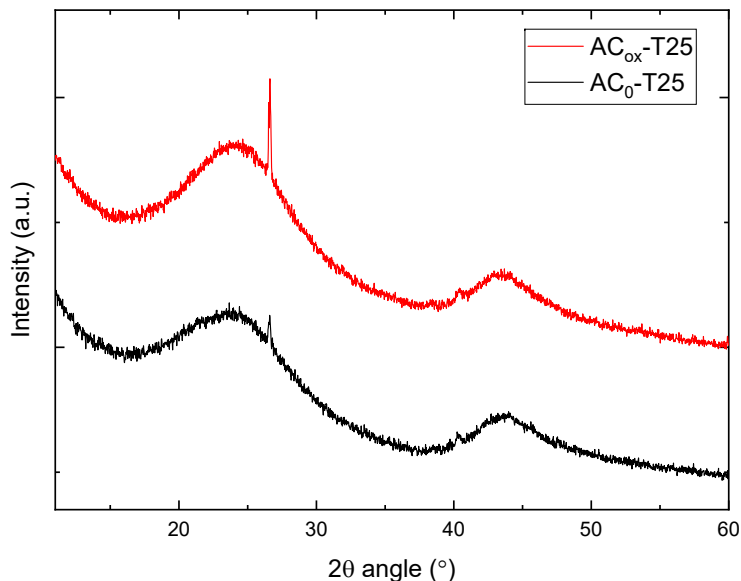


**Figure 4.15:** XRD patterns of the  $\text{AC}_0\text{-T25}$  and  $\text{AC}_{\text{ox}}\text{-T25}$  composites.

$\text{TiO}_2$  grafting becomes more efficient with larger TTIP volume fractions during the chemical treatment of AC. The AC itself consists of chunks that are between 20 and 200  $\mu\text{m}$  in diameter. The  $\text{TiO}_2$  crystals are roughly 100-500 nm in diameter, and they are aggregates of much smaller primary crystals. The reference obtained crystals that were significantly larger:  $\approx 5 \mu\text{m}$  in diameter. The difference could be due to the different shape and size of their ACF compared to our PAC; the former's more uniformly shaped fibers seem to enable more extensive aggregation of the primary  $\text{TiO}_2$  crystals. Comparing the two T25 composites, it is also possible to visually verify that there are more  $\text{TiO}_2$  crystals on the  $\text{AC}_{\text{ox}}$  surface than the  $\text{AC}_0$  surface.

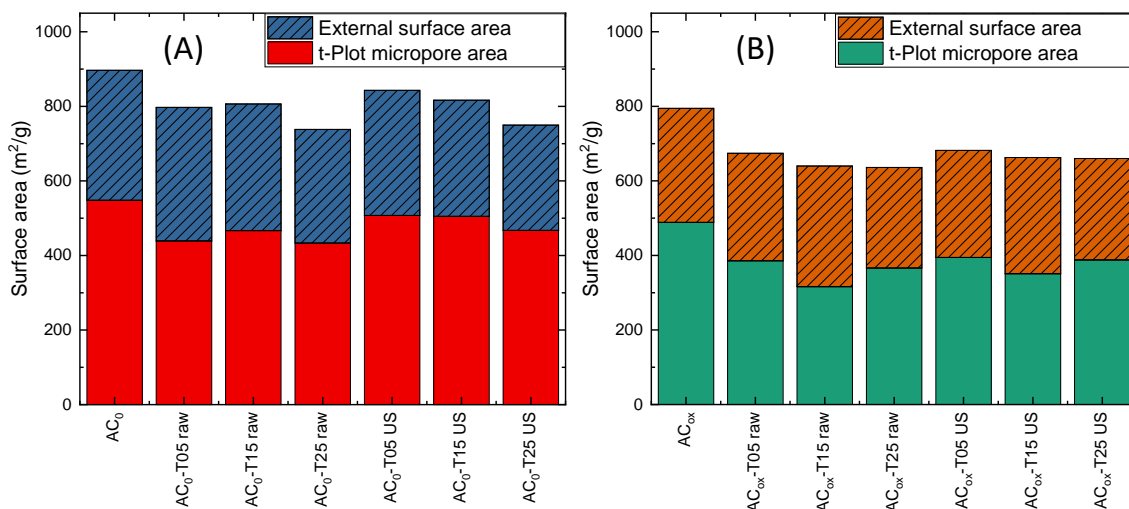


**Figure 4.16:** External and internal surface areas of  $\text{AC}_0$ ,  $\text{AC}_{\text{ox}}$ , and their composites. "Raw" denotes the materials before the ultrasonication treatment.

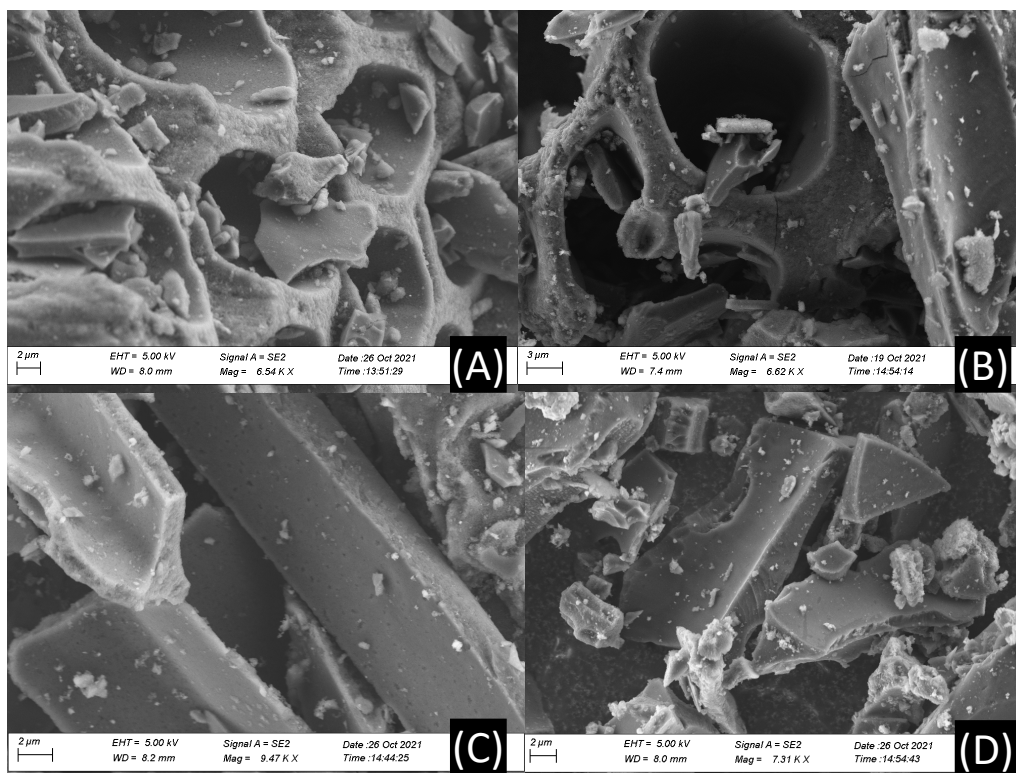


Figure 4.17: SEM images of (A) AC<sub>0</sub>, (B) AC<sub>0</sub>-T05, (C) AC<sub>0</sub>-T15, and (D) AC<sub>0</sub>-T25.

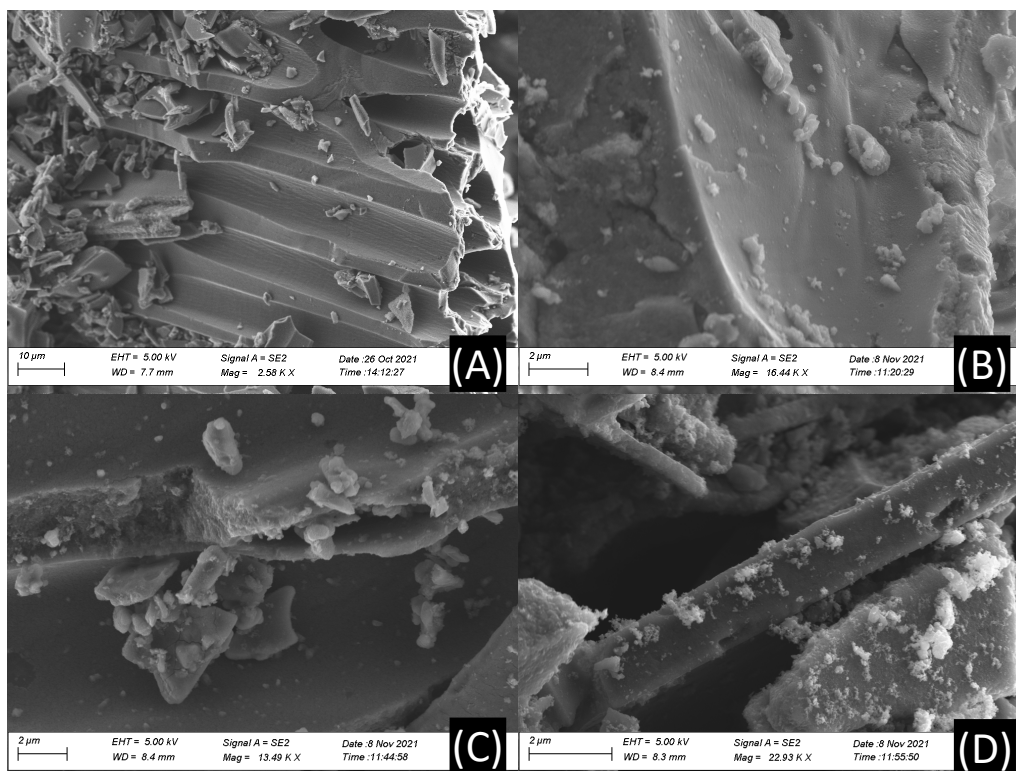


Figure 4.18: SEM images of (A) AC<sub>ox</sub>, (B) AC<sub>ox</sub>-T05, (C) AC<sub>ox</sub>-T15, and (D) AC<sub>ox</sub>-T25.

### 4.3.2 p-Cresol adsorption

The p-cresol adsorption isotherms obtained for the four different adsorbents  $\text{AC}_0$ ,  $\text{AC}_{\text{ox}}$ ,  $\text{AC}_0\text{-T25}$ , and  $\text{AC}_{\text{ox}}\text{-T25}$  are shown in Figure 4.19. Included in the graphs are the experimental adsorption data and the fitted data points from the Freundlich and Langmuir isotherm models.

In MQ water, the adsorption follows the Langmuir model for  $\text{AC}_0$  and  $\text{AC}_0\text{-T25}$  ((A) and (B) in Figure 4.19), according to the fitting  $R^2$  values in Tables 4.7 and 4.8. For  $\text{AC}_{\text{ox}}$  and  $\text{AC}_{\text{ox}}\text{-T25}$ , the Freundlich model gets a slightly better fit. This change in adsorption isotherm model would be expected since the Freundlich isotherm often is the best fit for heterogeneous surfaces, as both the introduction of oxygen chemical groups and  $\text{TiO}_2$  crystals make the AC surface less homogeneous.

The adsorption process in synthetic urine ((C) and (D) in Figure 4.19) is slightly different from in MQ water. Both  $\text{AC}_0$  and  $\text{AC}_{\text{ox}}$  now follow the Freundlich isotherm

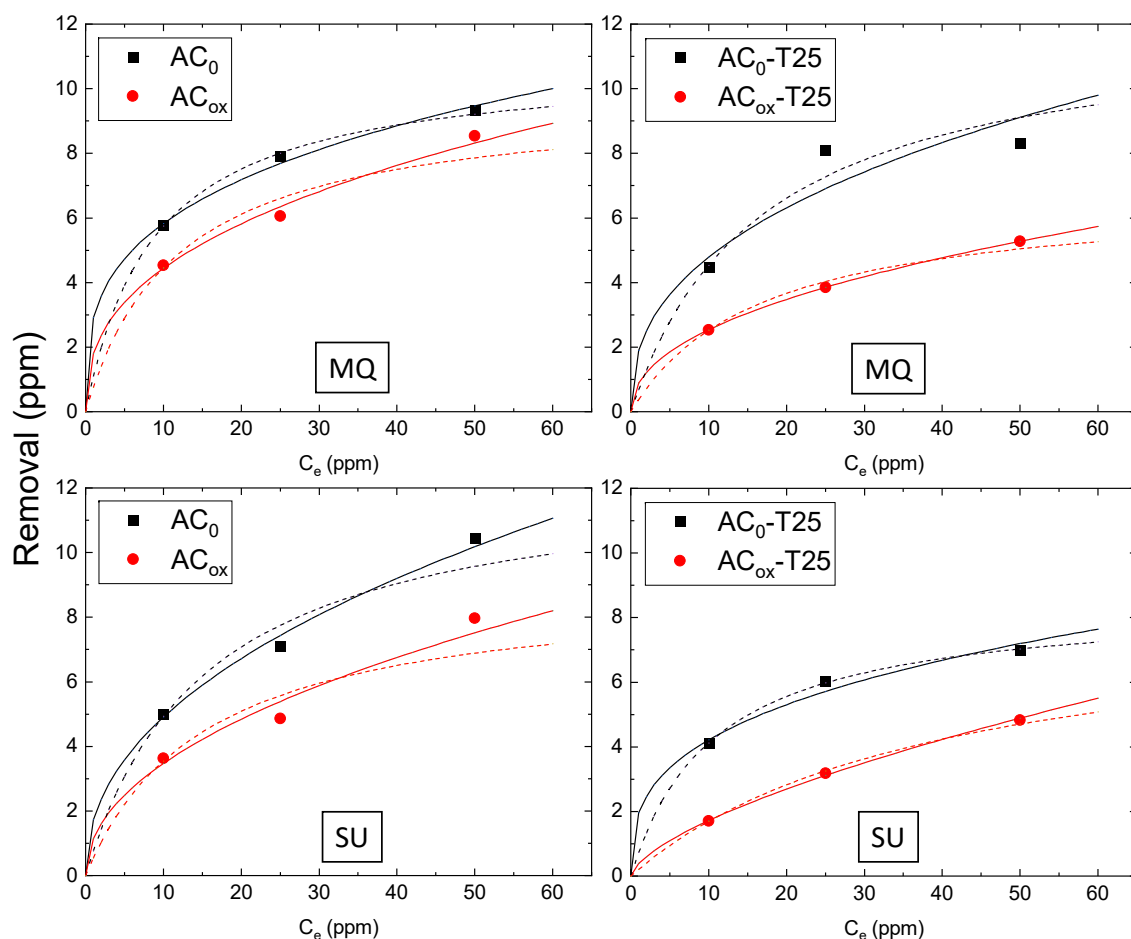


**Figure 4.19:** p-Cresol adsorption isotherms on (A)  $\text{AC}_0$  and  $\text{AC}_{\text{ox}}$  in MQ water, (B)  $\text{AC}_0\text{-T25}$  and  $\text{AC}_{\text{ox}}\text{-T25}$  in MQ water, (C)  $\text{AC}_0$  and  $\text{AC}_{\text{ox}}$  in SU, and (D)  $\text{AC}_0\text{-T25}$  and  $\text{AC}_{\text{ox}}\text{-T25}$  in SU. Filled symbols display experimental data point, while solid and dashed lines show data points from the linear fitting of the Freundlich and Langmuir models, respectively.

model more accurately. However,  $\text{AC}_0\text{-T25}$  strictly follows the Langmuir model ( $R^2 = 0.999$ ), while  $\text{AC}_{\text{ox}}\text{-T25}$  has got an  $R^2$  of 0.999 for both models. An interesting finding is that the adsorption of p-cresol is higher in SU than in MQ water for  $\text{AC}_0$ . Since the difference in pH between the  $\text{AC}_0$  dispersed in water and SU is small (5.9 vs. 6.1, see Table 4.7), this is likely not an effect of pH. The ZP of  $\text{AC}_0$  in water is -22 mV, while it is -10 mV in SU (Table 4.6), which also does not explain the enhanced p-cresol adsorption in SU relative to in water. Instead, it can be attributed to the salting out effect of the ions and urea in SU.

A consequence of the presence of ions and urea in SU is the phenomena of "salting in" and "salting out" of chemical species in water. Ions and molecules can be categorized according to their effect on the surrounding water structure, and for ions this can be related to the Hofmeister series covered in Subsection 2.1. Structure making ions and urea are known to cause salting-out of organic molecules, decreasing their solubility in water [112, 113]. This effect is more prominent in the presence of hydrophobic surfaces and leads to an increased adsorption capacity. Since  $\text{AC}_0$  is the most hydrophobic material in this study, it exhibits the strongest salting out effect.

**Table 4.6:** Zeta potentials of the adsorbents at the pH of adsorption (see Table 4.7).

Sample	ZP in water (mV)	ZP in SU (mV)
$\text{AC}_0$	-22	-10
$\text{AC}_0\text{-T25}$	-22	-10
$\text{AC}_{\text{ox}}$	-40	-11
$\text{AC}_{\text{ox}}\text{-T25}$	-22	-11

**Table 4.7:** Langmuir parameters for the adsorption of p-cresol in MQ water and synthetic urine with the experimental conditions:  $c_m = 0.1$  mg/mL,  $T = 37^\circ\text{C}$ ,  $t = 1$  h, 250 rpm. The pH values given were measured post-adsorption and are also valid for the Freundlich parameters.

Adsorbent	$q_{\text{max}}$ (ppm)	MQ water		
		$\bar{K}_L$ (1/ppm)	$R^2$	pH
$\text{AC}_0$	10.8	0.113	0.998	5.9
$\text{AC}_0\text{-T25}$	12.2	0.059	0.955	5.9
$\text{AC}_{\text{ox}}$	9.71	0.085	0.945	5.4
$\text{AC}_{\text{ox}}\text{-T25}$	6.72	0.060	0.989	5.0
		Synthetic urine		
$\text{AC}_0$	12.5	0.065	0.959	6.1
$\text{AC}_0\text{-T25}$	8.53	0.093	0.999	6.0
$\text{AC}_{\text{ox}}$	9.01	0.065	0.901	6.1
$\text{AC}_{\text{ox}}\text{-T25}$	8.45	0.025	0.999	6.0

**Table 4.8:** Freundlich parameters for the adsorption of p-cresol in MQ water and synthetic urine with the experimental conditions:  $c_m = 0.1$  mg/mL,  $T = 37^\circ\text{C}$ ,  $t = 1$  h, 250 rpm. The unit for the Freundlich constant is  $\text{ppm}^*(\text{ppm}^{-1})^{1/n}$ .

Adsorbent	MQ water		
	1/n	K <sub>F</sub>	R <sup>2</sup>
AC <sub>0</sub>	0.301	2.91	0.990
AC <sub>0</sub> -T25	0.400	1.90	0.846
AC <sub>ox</sub>	0.390	1.81	0.984
AC <sub>ox</sub> -T25	0.455	0.890	0.999
Synthetic urine			
AC <sub>0</sub>	0.454	1.73	0.987
AC <sub>0</sub> -T25	0.333	1.96	0.971
AC <sub>ox</sub>	0.480	1.15	0.950
AC <sub>ox</sub> -T25	0.650	0.383	0.999

Similar results were presented by Huang et al. (2009) [114], where the adsorption of phenol on a polystyrene polymer functionalized with formaldehyde carbonyl groups was tested in water containing NaCl or CdCl<sub>2</sub>. The large and monocharged Na<sup>+</sup> ion is considered a structure maker and was found to increase the adsorption of phenol by 52% (from 115 to 175 mg/g). Cd<sup>2+</sup>, on the other hand, decreased the phenol adsorption by 15% (from 121 to 103 mg/g). Cd<sup>2+</sup> is smaller than Na<sup>+</sup> [115] and carries two charges, and could therefore be considered a structure breaker ion. Usually, divalent ions, such as Mg<sup>2+</sup> are stronger structure maker ions than monovalent alkali metal ions (see Section 2.2). However, in the case of transition metals, due to the presence of d electrons, the charge of the ion does not solely determine its hydration structure. It is well known that the pK<sub>a</sub> of water around divalent transition metal ions decreases considerably, which might have a profound effect on the hydration structure.

Principal component analysis was used to investigate what surface and material properties govern the adsorption of p-cresol in MQ water (Figure 4.20) and synthetic urine (Figure 4.21). The maximum adsorption capacity,  $q_{\max}$ , as determined from the Langmuir model, is marked in red in both graphs. The PC coordinates of  $q_{\max}$  in both graphs are different, indicating that there is a significant difference between the adsorption in water and SU.

In MQ water, there is a strong dependence on solution pH, wetting angle, and  $\text{pH}_{\text{PZC}}$ , i.e., the optimal material would be hydrophobic with a slightly elevated  $\text{pH}_{\text{PZC}}$ . In SU, the surface area properties are more important than the surface charge properties. This could be due to the prevalence of ions in synthetic urine, which screen the surface charge of the adsorbent. In fact, Table 4.6 shows that the ZP of all four adsorbents in SU is 10-11 mV, while in water, the difference is larger.

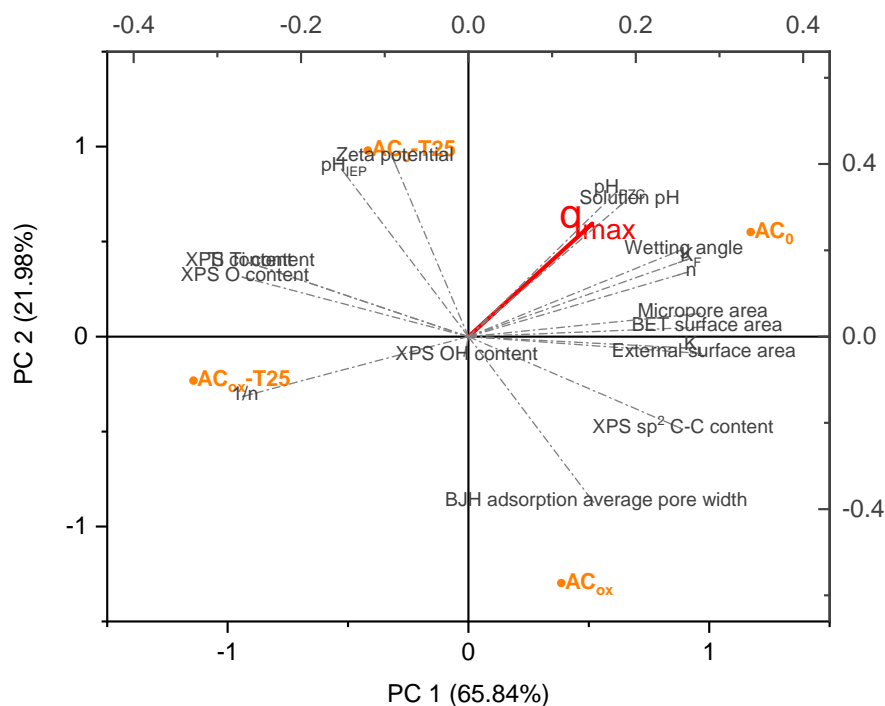


**Figure 4.20:** Loading plot of the PCA in MQ water showing the correlation between adsorbent properties and  $q_{\max}$ .

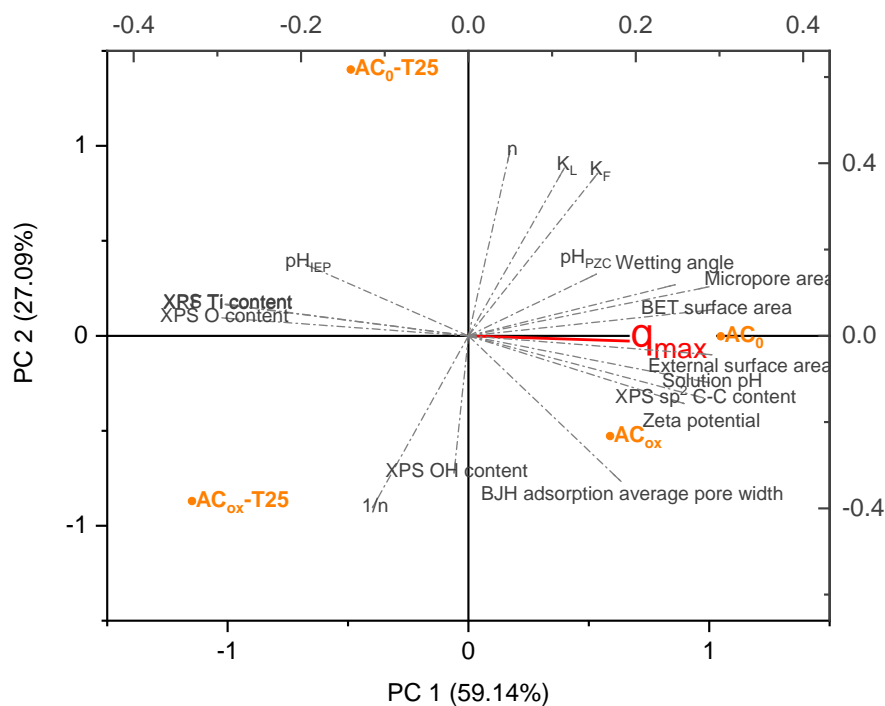


**Figure 4.21:** Loading plot of the PCA in synthetic urine showing the correlation between adsorbent properties and  $q_{\max}$ .

## 4.4 Paper IV: Surface characterization of SCNC

The potentiometric and conductometric titrations of the sulfate-functionalized crystalline nanocellulose revealed that the surface of the SCNC is negatively charged already at pH 3 (Figure 4.22). The high-SCNC carries almost exactly twice the negative charge as the low-SCNC does. Between pH 11 and 12, the SCD starts to increase sharply, indicating that a more weakly acidic type of surface group is getting deprotonated around that pH. This could either be less accessible sulfate groups or a hydroxyl group belonging to the nanocellulose's glucose units (Figure 4.23).

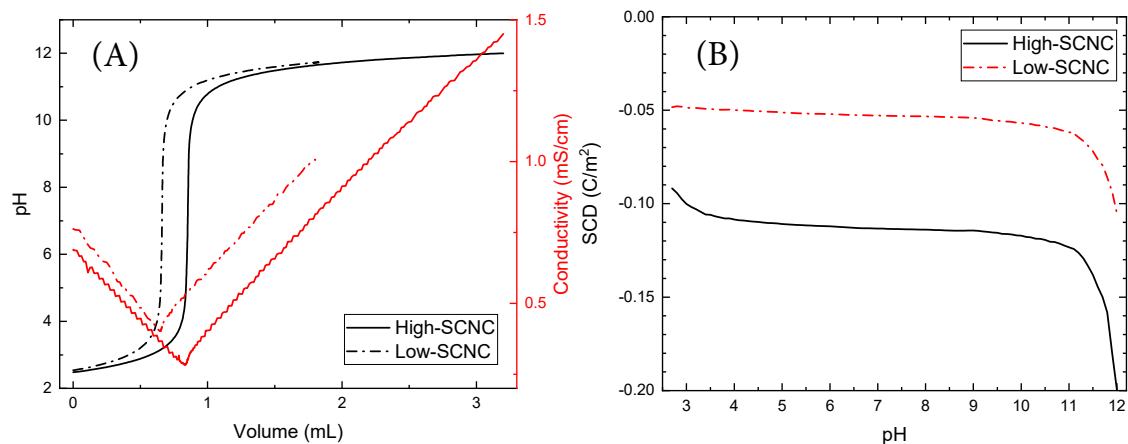


**Figure 4.22:** (A) Demonstration of the simultaneous potentiometric and conductometric titrations performed on 0.6 wt% low- and high-SCNC in 1 mM KCl and 2.5 mM HCl to pH 12. (B) Calculated surface charge densities from the titration data in (A).

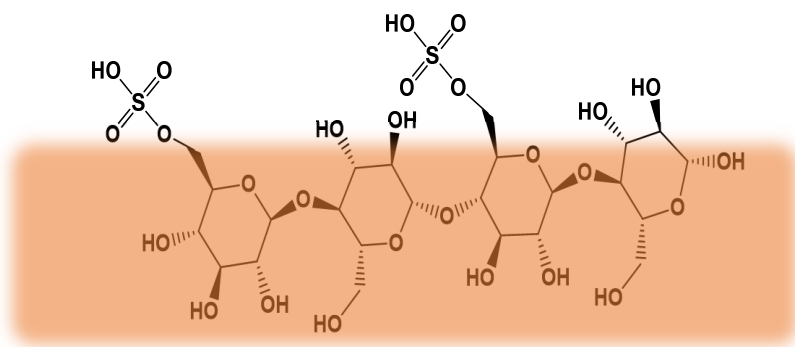


**Figure 4.23:** Schematic image of the SCNC surface, showing the different surface groups.

From the potentiometric titration data, SCDs were calculated, and the average values for each salt concentration, all of whom were run in triplicate, are shown in Figure 4.24. Similarly to the silica nanoparticles in section 4.1, the trend follows the direct Hofmeister series, i.e., the SCD increases in the order:  $\text{Li}^+ < \text{Na}^+ < \text{K}^+$ . However, a significant difference between  $\text{SiO}_2$  and SCNC titration results is that a lower concentration of salt is required to see these ion-specific effects on the SCNC. At higher salt concentrations ( $\geq 10$  mM), the SCNC gelled, which interfered with the pH measurements, and therefore no data from those titrations are presented here.

At lower pH, the SCD in the presence of  $\text{Li}^+$  strongly deviates from the other two counter-ions, and the SCD becomes much less negative. For  $\text{Na}^+$  and  $\text{K}^+$ , the difference in SCD is less explicit, and the curves occasionally overlap. Worth noting is that the titration of SCNC dispersions is difficult due to the rapid gelling of the needle-shaped crystals even at low ionic strengths, and this inevitably affects the measurement output. Despite this, it can be said with certainty that there is an apparent specific ion effect on the surface charge behavior of the SCNC.

The FTIR results (Figure 4.25) also show the difference in surface sulfate content between the high- and low-SCNC, as the C-O-S symmetric stretching peak at  $811\text{ cm}^{-1}$  [116] is more intense for the former. The other FTIR peaks are characteristic for nanocellulose and correspond well with the microcrystalline cellulose (MCC) reference, such as the water peak at  $1650\text{ cm}^{-1}$ , C-H stretching at  $2996\text{ cm}^{-1}$ , glucose ring vibration at  $1052\text{ cm}^{-1}$ , C-OH stretching at  $1161\text{ cm}^{-1}$ , C-O-C vibrations at  $898\text{ cm}^{-1}$ , and C-O vibrations at  $983\text{ cm}^{-1}$ .

TGA was performed on microcrystalline cellulose, high-SCNC, and low-SCNC that had dried without any addition of base to alter the pH. To investigate whether

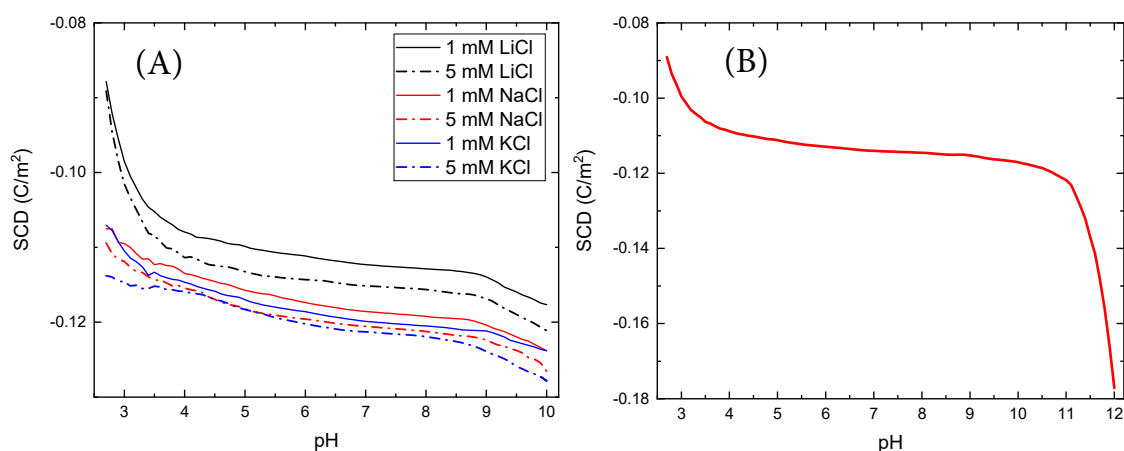


**Figure 4.24:** (A) Calculated SCDs of 0.6 wt% high-SCNC in various salts and 2.5 mM HCl. (B) SCD of 0.6 wt% high-SCNC in 1 mM NaCl and 2.5 mM HCl to pH 12.

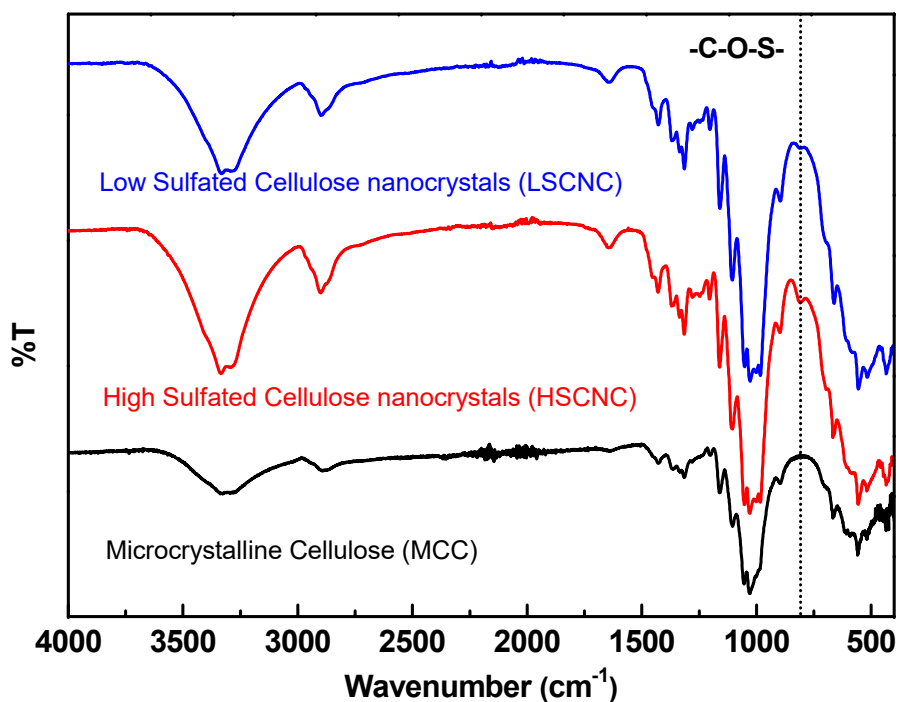


**Figure 4.25:** FTIR spectra of the low-SCNC, high-SCNC and MCC.

the presence of counter-ions, such as  $\text{Na}^+$ , can affect the thermal stability of nanocellulose, NaOH was added to the SCNC dispersion before drying and TGA analysis. The results are shown in Figure 4.26. The MCC reference has one sharp decomposition step at  $338^\circ\text{C}$ , while the high- and low-SCNC decompose over a larger range of temperature, starting around  $174$  and  $178^\circ\text{C}$ , respectively.

The difference in decomposition temperature between the MCC and SCNC indicates that the introduction of sulfate surface groups has a destabilizing effect on the nanocellulose, which others have also observed [116]. This effect is partially inhibited upon the addition of  $\text{Na}^+$  counter-ions and increasing the pH before freeze-drying the SCNC. The replacement of protons with sodium ions to make  $\text{CNC-OSO}_3\text{-Na}$  functional groups appears to have a stabilizing effect on the SCNC. Wang et al. (2007) [117] explained a similar finding that the  $\text{Na}^+$  ions inhibit the dehydration reaction that is catalyzed by sulfuric acid. They confirmed their theory by measuring the amount of char in the SCNCs with and without added NaOH after TGA measurements to  $500^\circ\text{C}$ . The NaOH-treated SCNC contained a smaller amount of char, although the difference was only 1 % for the CNC treated with 1 w/w% NaOH. The 10 w/w% NaOH gave a more considerable difference of 10 %.

During the drying process, all water is eliminated, and any salt added to the dispersion will precipitate on the SCNC surface. The consequence of this can be seen in the XPS results (Table 4.9); there is a significant amount of  $\text{Na}_2\text{SO}_4$  at the surface of the pH 12 samples. To these dispersions, NaOH has been added before drying. The presence of  $\text{Na}_2\text{SO}_2$  indicates that the added  $\text{Na}^+$  ions directly interact

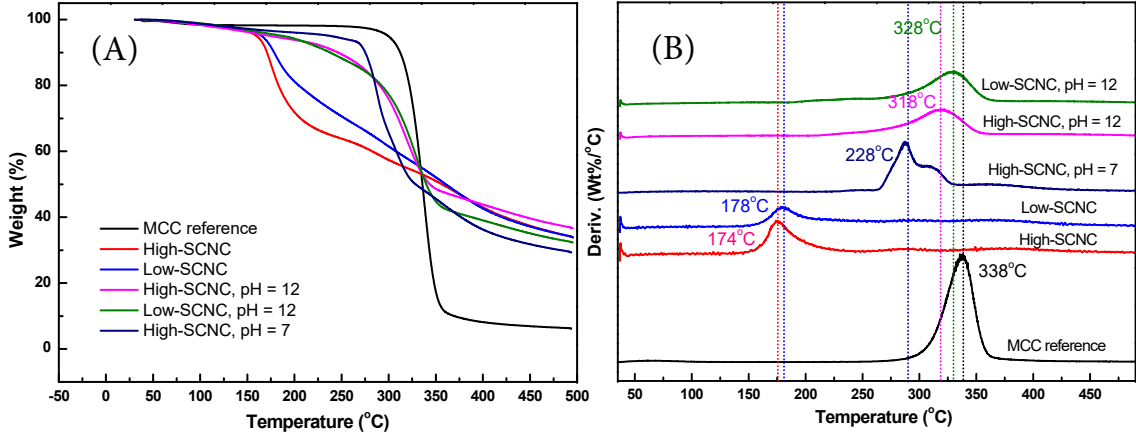


**Figure 4.26:** (A) TGA results of the MCC, high-SCNC, and low-SCNC. (B) Differential TGA results for the same samples.

with the sulfate on the SCNC surface. To test whether any free sulfate exists in the SCNC dispersions at alkaline pH, the SCNC was kept at pH 12 overnight, after which the SCNC was filtered off using a syringe filter. The filtrate was tested for sulfate by adding aqueous barium nitrate. If an alkaline hydrolysis reaction of the sulfate groups on the SCNC had occurred, the liberated  $\text{SO}_4^{2-}$  ions would form a strong, insoluble salt with  $\text{Ba}^{2+}$ . However, no white  $\text{BaSO}_4$  precipitate was observed.

Zeta potentials were determined for the SCNC dispersions at unadjusted pH ( $\text{pH}_0 \approx 3$ ), pH 7, and pH 10 containing up to 25 mM of either NaCl or LiCl (Figure 4.27). For the unadjusted pH, the addition of salt initially screens the surface charge, resulting in a reduction in ZP. At an ionic strength of 25 mM, the ZP has drastically become more negative. This has previously been observed in some systems, where it is attributed to "overcharging" of the surface. However, this is more common for divalent and trivalent co-ions and not likely to occur with  $\text{Cl}^-$  ions. The same increase in ZP at 25 mM salt concentration is shown for neutral and alkaline pH, although the effect is slightly smaller.

**Table 4.9:** Results from the XPS analyses of high- and low-SCNC for sulfur and sodium, in the form of at%. For the pH 12 samples, NaOH has been added to increase the pH.

Peak	S 2p <sub>3/2</sub>	Na 1s
Binding energy (eV)	> 167.0	1071.2
Chemical State	S(VI)	Na <sub>2</sub> SO <sub>4</sub>
High-SCNC	0.3%	-
High-SCNC, pH 12	0.2%	10%
Low-SCNC	0.1%	-
Low-SCNC, pH 12	0.1%	3%

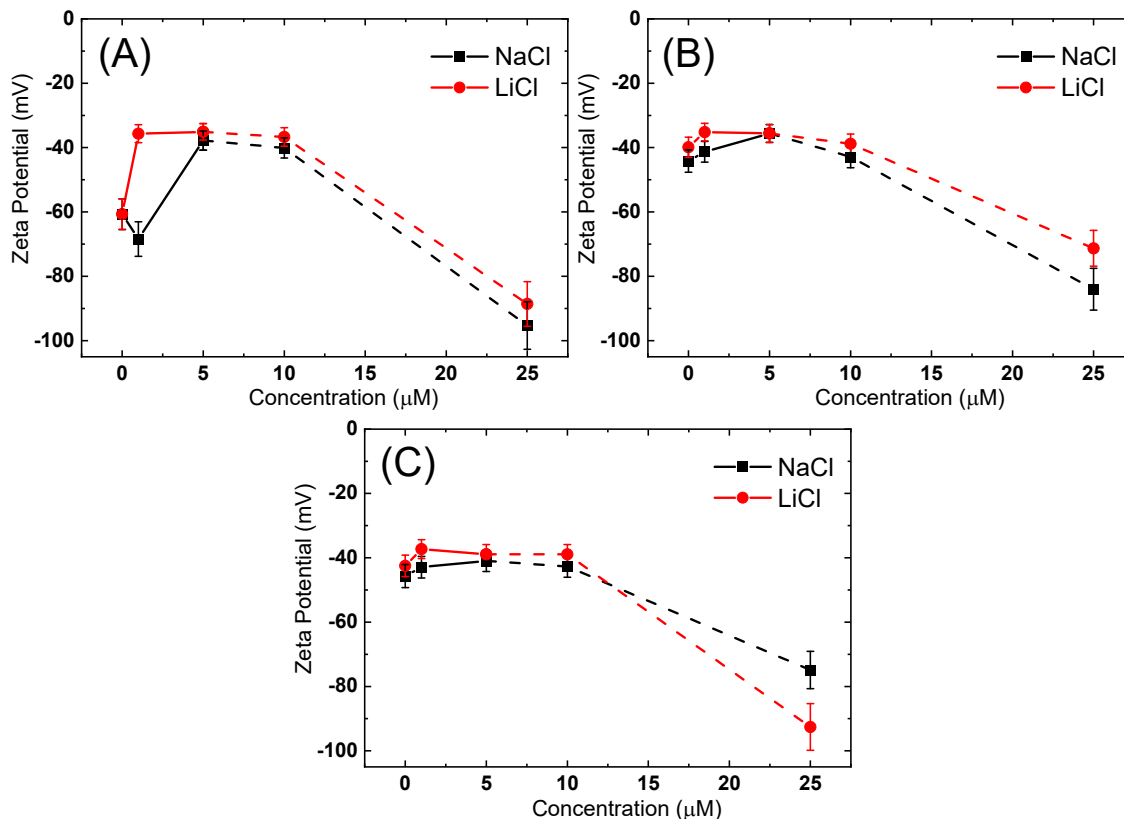


**Figure 4.27:** Zeta potentials of 0.2 wt% SCNC at pH (A) 3, (B) 7, (C) 10, adjusted using NaOH. The error bars show the standard deviations of the triplicate measurements. The dashed lines indicate salt concentrations that are known for causing significant gelling of the SCNC.

The most dramatic discovery of the ZP measurements is the trend reversal found at pH 10 (Figure 4.27 (C)), where LiCl infers a stronger negative charge than NaCl. Since  $\text{Li}^+$  is more hydrated than  $\text{Na}^+$ , it is usually inhibited from approaching and shielding hydrophilic negatively charged surfaces by the water molecules strongly bound to the ion. A similar phenomenon has been observed previously with silica nanoparticles and the even more hydrated cation  $\text{Mg}^{2+}$  [118]. At pH  $> 9$ ,  $\text{Mg}^{2+}$  screened the surface charge and caused gelling of the  $\text{SiO}_2$  nanoparticles more efficiently than  $\text{Ca}^{2+}$ . This finding contradicts the consensus for the silica surface that less hydrated cations exhibit stronger charge screening than more hydrated cations, as demonstrated by the direct Hofmeister series (Section 2.1). Below pH 9, the direct Hofmeister series governed the degree of charge screening, as observed by others for monovalent cations [18]. A plausible explanation for this unusual phenomenon can be sought in Collins' theory [119] of ion pair formation between two ions with similar water structure behavior. Recently, it has been shown by experiments and simulations that  $\text{Li}^+$  ions interact more strongly with a highly charged monolayer of deprotonated carboxylic groups, compared to a weakly charged monolayer [120]. They also observed a trend reversal for the counter-ion adsorption on

the monolayer at  $\text{pH} > 6$ , where  $\text{Li}^+$  was preferentially adsorbed over  $\text{Na}^+$  and  $\text{Cs}^+$ .

## 4.5 Paper V: *In-silico* studies on p-cresol adsorption in synthetic urine

Molecular dynamics simulations were performed by modelling the carbon surface as a graphene sheet. Three types of graphene surfaces were modelled: Pristine graphene, and two types of graphene oxide sheets, containing carboxylic, epoxy, and hydroxyl groups, with 50/60% and 100% deprotonated surfaces. p-Cresol and synthetic urine with the corresponding ion and urea concentrations as given in Table 3.5 were included in the simulations.

Radial distribution functions (RDFs) in the presence of four different graphene sheets were obtained from the molecular dynamic simulations to investigate the adsorption of p-cresol in synthetic urine. Figure 4.28 shows the probability ( $g(r)$ ) of finding the molecule of interest at a distance  $r$  from the sheet in the direction perpendicular to the sheet's plane. The concentrations of the ions and urea in the SU correspond to the synthetic urine used in the adsorption experiments in section 4.3, see Table 3.5. The p-cresol molecules adsorb the closest to the unmodified graphene sheet (black line) and with the highest probability by a factor of 2 compared to the fully protonated hydroxyl- and carboxyl-functionalized graphene (red line). For the partially (blue line) and fully deprotonated (purple line) hydroxyl- and carboxyl-functionalized graphene, the adsorption of p-cresol is significantly lower. The RDFs of urea (Figure 4.28 (B)) show a less dramatic difference between the different sheets, with the highest affinity for the partially deprotonated graphene sheet, and the lowest affinity for the fully deprotonated version.

In order to further investigate the environment around the graphene sheets, RDFs of the ions in SU were obtained (Figure 4.29). There is almost no difference between the pristine graphene (A) and the uncharged graphene with protonated

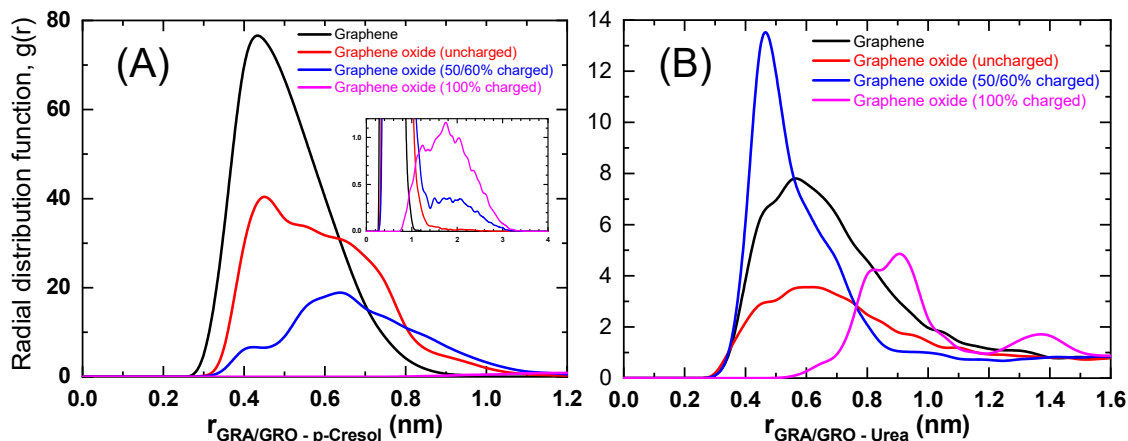


**Figure 4.28:** RDFs obtained from MD simulations of (A) p-cresol and (B) urea on the four different graphene sheets in SU.

hydroxyl and carboxyl groups (B). The charged surfaces, i.e., the partially (C) and fully (D) deprotonated carboxyl and hydroxyl functionalized graphene sheets, have the highest affinities for both the cations and the anions; the ions adsorb closer to the surface and with higher density function values. The trend, however, differs between the two charged cases. The partially deprotonated surface (C) attracts  $\text{NH}_4^+$  the strongest, while the more simple cations  $\text{Na}^+$  and  $\text{K}^+$  adsorb further away from the sheet and to a lesser degree. The fully deprotonated surface (D) adsorbs the least hydrated cation ( $\text{K}^+$ ) the strongest. The difference between the  $\text{K}^+$  adsorption between the two charged sheets is significant, and is most likely due to the charge difference.

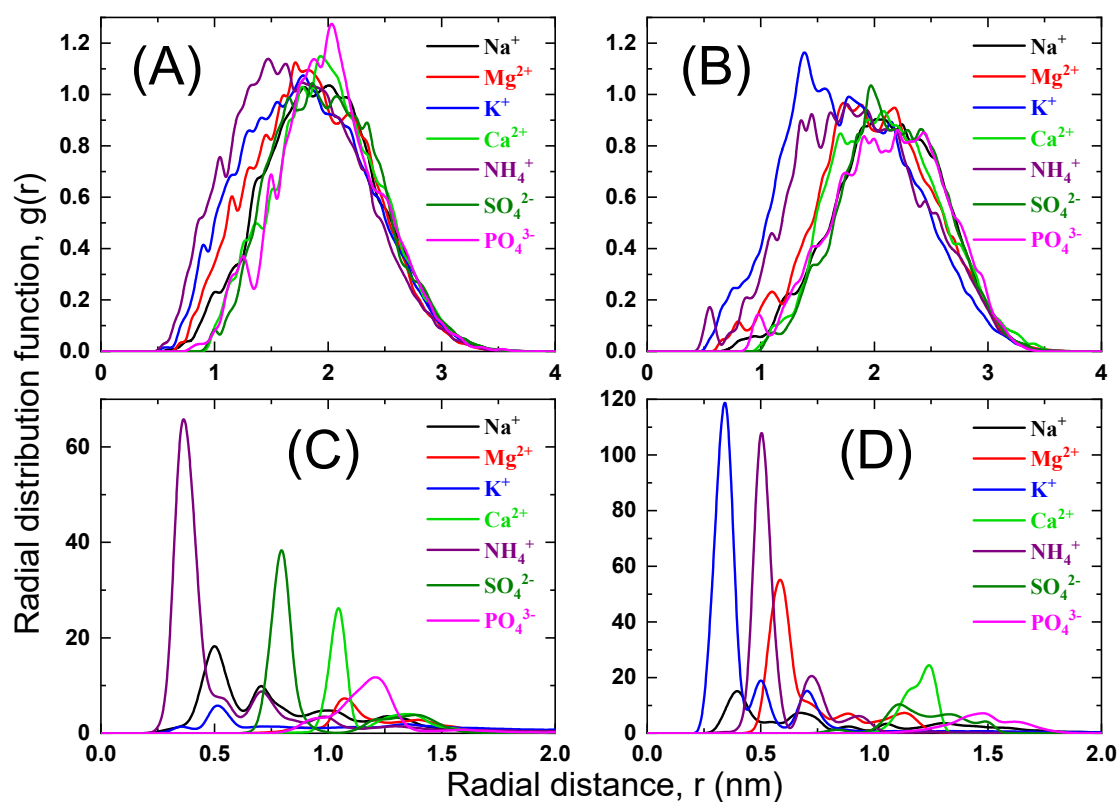


**Figure 4.29:** RDFs obtained from MD simulations of the ions in SU near a sheet of (A) graphene, and graphene with hydroxyl and carboxyl groups that are (B) fully protonated, (C) partially deprotonated, and (D) fully deprotonated. Note the differences in scale of both the Y and X axes. The RDF values have been normalized with respect to ion concentration.

Two concentrations of p-cresol were tested; 3 (solid line) and 6 (dashed line) molecules per sheet, as shown in Figure 4.30. These concentrations correspond to 50 and 100 ppm, respectively. For the uncharged surfaces, (A) and (B), a lower p-cresol concentration favors closer adsorption than a higher concentration. This could be due to increased crowdedness around the sheet as it is approached by more p-cresol molecules. The two charged surfaces, (C) and (D), do not exhibit the same

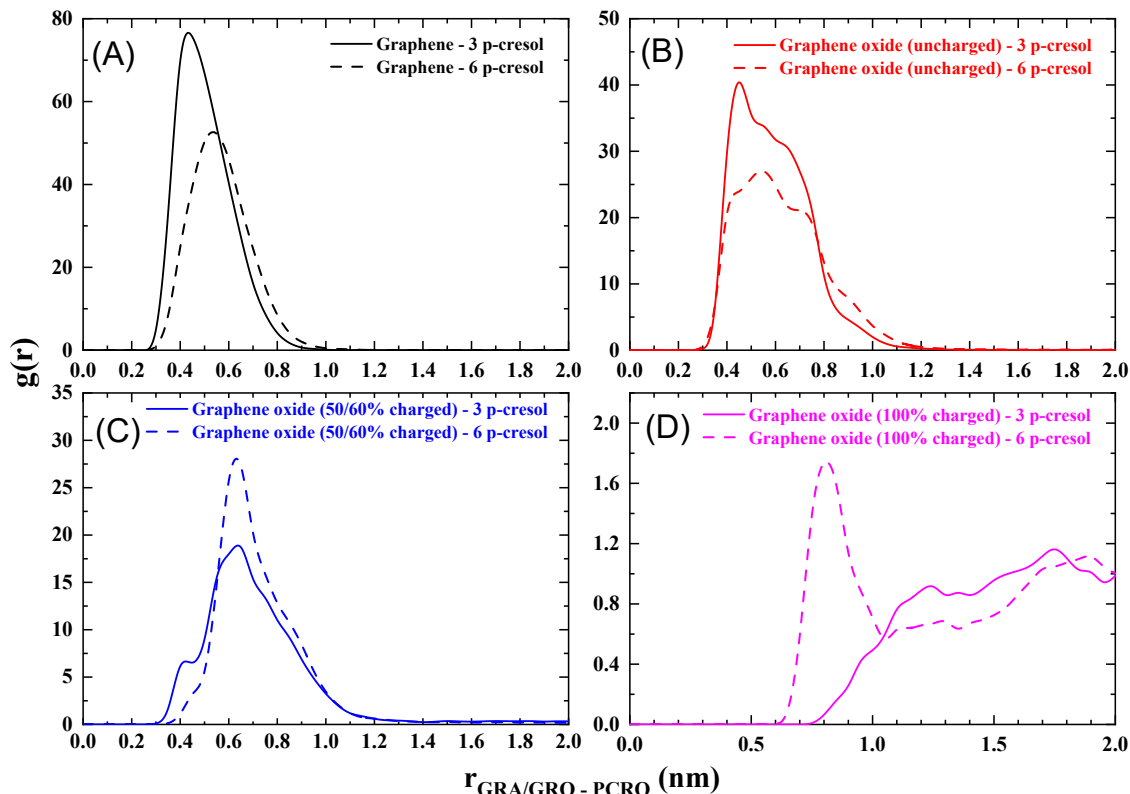


**Figure 4.30:** RDFs for two different concentrations of p-cresol with respect to the surface of (A) graphene, and graphene oxide with hydroxyl and carboxyl groups that are (B) fully protonated, (C) partially deprotonated, and (D) fully deprotonated. Note the difference in scale of the Y- and X-axes.

inhibition of p-cresol adsorption as the number of molecules is doubled. Instead, the density is increased, and, in the case of the fully deprotonated surface, the p-cresol adsorbs closer to the sheet, although at a significantly lower density probability.

Figure 4.31 (A) demonstrates the orientation of the p-cresol molecules when they are physically adsorbed to the graphene sheet in SU. The inset displays the alignment of the benzene ring of the p-cresol with the benzene rings in the graphene. This attractive force between aromatic rings is called  $\pi - \pi$  stacking and has been observed in similar systems before, for example, polycyclic aromatic hydrocarbons on graphene and graphene oxide [121, 122, 123]. The importance of  $\pi - \pi$  stacking in the adsorption of p-cresol on graphene oxide has been previously mentioned in literature [124]. The lack of water molecules in-between the sheet and p-cresol indicates a direct interaction between the adsorbate and the sheet.

Comparing the adsorption on graphene with the fully charged graphene oxide (Figure 4.31 (B)), the p-cresol molecules do not align in the same orientation in the latter case. No  $\pi - \pi$  stacking is observed, and the water molecules seem to be able to move freely between the sheet and p-cresol, i.e., the opposite case to the graphene sheet.

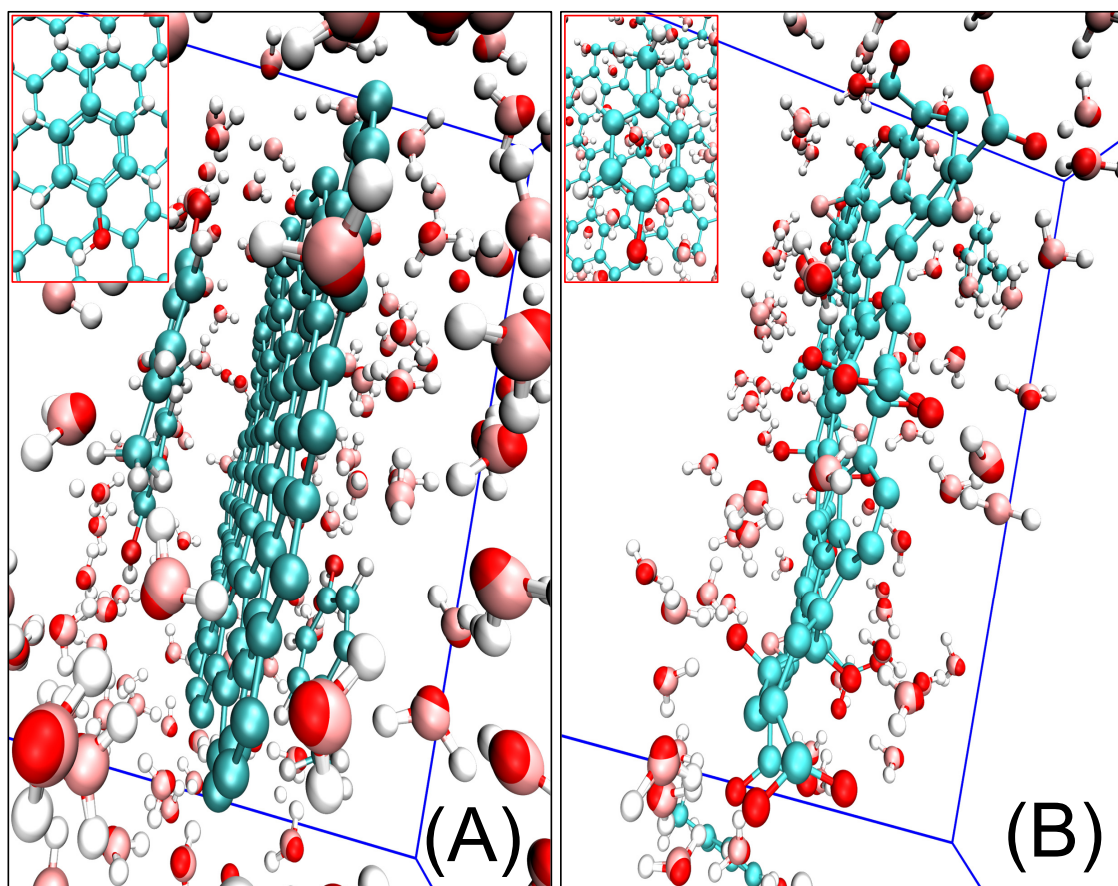


**Figure 4.31:** Snapshot from the MD simulations of (A) graphene and (B) fully deprotonated graphene oxide, showing the preferred location and orientation of the p-cresol molecules. Only p-cresol and water have been included in the images for clarity. The insets display examples of the highly probable alignments of p-cresol near the respective sheets.

### 4.5.1 ICP-OES ion adsorption study

The ion adsorption experiments presented in Figure 4.32 were performed to see whether the results in section 4.5 could be confirmed by experimental means.  $AC_0$  contains oxygen surface groups (Table 4.3, but has got a  $pH_{PZC}$  of 7.5 (Table 4.2), and can therefore be considered to correspond well with the uncharged graphene sheet with protonated hydroxyl and carboxyl groups ((B) in Figure 4.29).  $AC_{ox}$  is more acidic with a  $pH_{PZC}$  of 2.8 (Table 4.2), so it can be compared to the fully deprotonated functionalized graphene sheet ((D) in Figure 4.29).

The  $Na^+$  removal is 65% larger for  $AC_0$  than  $AC_{ox}$  in synthetic urine. This contradicts the results from the MD simulations, where it was found that  $Na^+$  adsorbs to a greater extent to the negatively charged surfaces. The same conclusion can be drawn for the other ions, except for the divalent cations  $Ca^{2+}$  and  $Mg^{2+}$ . The reason for this discrepancy between simulated and experimental results is most likely due to the difference in scale and system setup. The MD simulations used a flat sheet composed of 5 x 8 benzene rings as the solid-liquid interface, resulting in a square with dimensions  $1.7 \times 1.3 \text{ nm}^2$ . The adsorption experiments used powdered AC with micropores of 1.7 and 1.6 nm in diameter for  $AC_0$  and  $AC_{ox}$ , respectively. Since the internal surface area of  $AC_0$  and  $AC_{ox}$  constitutes 61% of the total surface area, simulating their interface using a flat sheet will not always be completely accurate. However, it is a step in the right direction towards understanding the adsorption behavior and ion effects near interfaces of real systems.

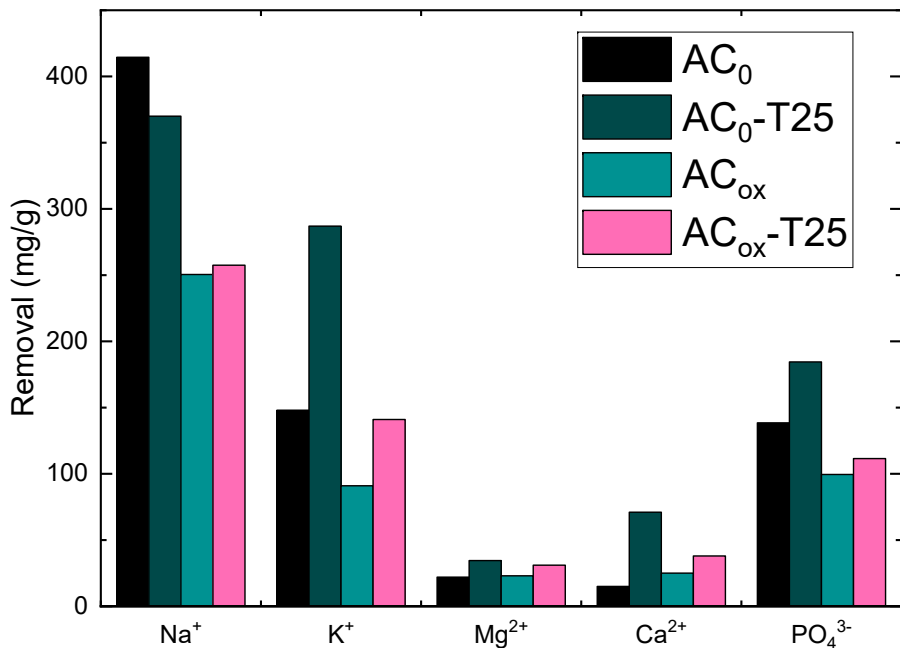


**Figure 4.32:** Results from the adsorption of the ions in synthetic urine using two different activated carbons and their  $TiO_2/AC$  composites. The ion concentrations were determined using ICP-OES.

# Chapter 5

## Concluding Discussion and Outlook

The overall goal of this thesis work was to find an efficient adsorbent for odor control, which can be used in incontinence products. The adsorption of odor molecules from an aqueous salt mixture such as urine will be significantly determined by ion interactions with the solid surface. To gain a fundamental understanding of these interactions with different surfaces, we started the work with the silica surface (paper I) as a model of a negatively charged surface. Nanocellulose is another interesting material for odor adsorption; therefore, we investigated in detail how negatively charged cellulose can have specific ion interactions (paper IV). For efficient adsorption, the surface area, pore structure, and complexing sites on the material are essential, and MOFs are an example of such material. We synthesized environmentally friendly MOFs (paper II) and thoroughly investigated their synthesis process and surface properties. Since active carbon is an economically friendly and widely used adsorbent, we evaluated the efficiency of activated carbon as an adsorbent for p-cresol in synthetic urine by modifying its surface properties through oxidation and doping with  $\text{TiO}_2$  (paper III). We performed MD simulations of neutral and charged graphene sheets in synthetic urine containing p-cresol to gain information at the atomic scale about the ionic and p-cresol interactions with these surfaces (paper V).

## 5.1 Ion interactions

One of the main takeaways from this project is that there is more to ions than one might think. Their complexity stems from the large number of interactions they can take part in, depending on concentration, temperature, solvent, the nature of surface they are interacting with, and more. For example, they can interact with:

- (i) the surrounding solvent, creating hydration shells,
- (ii) oppositely charged ions, forming ion-pairs,
- (iii) molecules, affecting their solubilities, and
- (iv) interfaces, significantly altering their physicochemical properties.

The small scale of ions, water molecules, and nanoparticles makes it challenging to directly study their properties and interactions. In papers I and IV, the interactions of ions with two popular negatively charged nanomaterials, silica nanoparticles and crystalline nanocellulose, were investigated by potentiometric titrations yielding surface charge densities. For both materials, the less hydrated cations induced a stronger surface charge by adsorbing nearer the 0-plane than the more hydrated cations. There was also an observable effect on the type of co-ion present during the silica titrations; Nitrate and sulfate evoke a weaker surface charge than chloride. We could attribute this co-ion effect to the formation of ion-pairs in solution, i.e., there are strong interactions of  $\text{Na}^+$  and  $\text{K}^+$  with  $\text{NO}_3^-$  and  $\text{SO}_4^{2-}$ , limiting the number of available counter-ions that can adsorb to the surface.

To complement the titration results, gel-times of silica sols were measured, which included more types of co-ions ( $\text{Cl}^-$ ,  $\text{ClO}_4^-$ ,  $\text{ClO}_3^-$ ,  $\text{NO}_3^-$ ,  $\text{SO}_4^{2-}$ ) at higher mass and ion concentrations, revealing a more distinct co-ion effect than the titrations. The ion distribution and concentration around the charged surface will be different from the bulk due to the electric double layer. It is challenging to know the exact salt concentration in the EDL, but the strong evidence of ion-pairing indicates that it is significantly larger than in the bulk.

Another discovery from the titration experiments is the surface charge behavior of nanocellulose containing sulfate surface groups. Previous studies have presented conductometric or potentiometric titrations in the form of equivalent charges and only titrated up to pH 10. By converting the titration data to surface charge densities, with units of Coulomb per  $\text{m}^2$  surface area, more comparable results were obtained with respect to the surface charge behavior. The titrations to pH 12 revealed the presence of another type of weakly acidic surface group on the CNC, which has not been shown with titrations before, to the authors' knowledge. Other groups have observed that the total sulfur content of SCNCs, as measured by ICP-OES [125] and XRF [126] are larger than what the conductometric titrations to  $\text{pH} < 10$  have shown. Specific ion effects have only before been investigated by

coagulation experiments [127, 128]. Our results confirmed that there is a distinct influence of the type of counter-ion on the SCD of the SCNCs even at lower salt concentrations.

The molecular dynamics simulations of neutral and negatively charged graphene and graphene oxide sheets in artificial urine (Paper V) revealed that there are significant complexation interactions between the  $\text{PO}_4^{3-}$ ,  $\text{SO}_4^{2-}$ ,  $\text{Ca}^{2+}$ , and  $\text{Na}^+$  ions, which get stronger as the  $\text{Na}^+$  concentration increases.

## 5.2 Odor capture in synthetic urine

The adsorption of molecules in their natural environment is an important research area to understand the process and for the development of new adsorbents. For the liquid-phase adsorption of odorants originating from urine, this is no exception. Since urine may contain several thousands of various chemical substances, it is more convenient to use synthetic urine for these kinds of adsorption studies.

While activated carbon is a popular choice of adsorbent due to its large surface area from its pores, benefitting physisorption, it has got limited chemisorption potential as it only contains carbon and, in some cases, oxygen groups on its surface. By incorporating another type of material onto its surface, a material with the potential for both chemisorption and physisorption can be obtained. In addition, the addition of certain materials will alter the electrostatic properties of the AC, possibly promoting odor capture through increasing the attractive forces between the adsorbent and the adsorbate.

The doping of  $\text{TiO}_2$  on  $\text{AC}_0$  and  $\text{AC}_{\text{ox}}$  gave a more amphoteric and hydrophilic surface without a significant reduction in surface area and porosity. Having a chemically stable material with a large and porous surface that is positively charged below pH 5 can be beneficial in many applications in aqueous environment.  $\text{TiO}_2$  is a well-known photocatalyst, further broadening its usability.

For the adsorption of p-cresol in water and SU (Paper III), the  $\text{TiO}_2$  doping of AC gave mixed results. For  $\text{AC}_{\text{ox}}$ , the adsorption decreased in both solvents, and made the isotherms more Langmuir-type, indicating a more homogeneous surface. The doping significantly increased the hydrophilicity, as determined by wetting angles, and XPS measurements revealed that the oxygen content of the surface increased from 9 at% to >40 at%. The maximum Ti(IV) content obtained was 14 at% and SEM images confirmed the presence of  $\text{TiO}_2$  nanocrystals on the AC surface.

The Langmuir adsorption isotherm yields  $q_{\text{max}}$ , a quantity representing the theoretical maximum adsorption capacity of a specific adsorbent-adsorbate-solvent combination. The  $q_{\text{max}}$  of  $\text{AC}_0$  in water increased from 10.8 to 12.2 ppm upon  $\text{TiO}_2$ -doping, but the corresponding  $R^2$  value decreased from 0.998 to 0.955, indicating that the Langmuir model might not be an optimal fit for this system.

In synthetic urine, the adsorption on  $\text{AC}_0$  improved relative to in water, and the adsorption type changed from Langmuir to Freundlich. This is attributed to the salting out effect of some of the ions and the urea in SU, which is stronger for more hydrophobic molecules and surfaces.

To rationalize our experimental results, we performed molecular dynamics simulations of the p-cresol adsorption in synthetic urine. Four surfaces were tested: Regular graphene and three graphene oxide sheets containing hydroxyl and car-

boxyl groups with varying degrees of deprotonation, to simulate different surface charges. The MD showed that the p-cresol adsorption in SU increased in the order: GO (fully charged) < GO (50/60 % charged) < GO (uncharged) < graphene. Snapshots from the simulations established that strong  $\pi - \pi$  interactions facilitated the adsorption of p-cresol on graphene. These interactions were not present in the fully charged graphene oxide system. The MD simulations also revealed that, due to the presence of counter-ions near the 100% charged surface, the interaction of p-cresol with the surface weakened. This is in accordance with the experimental adsorption results presented in paper III showing decreased adsorption of p-cresol in synthetic urine compared to water for the AC<sub>ox</sub> material.

## 5.3 The iron(III) TPA MOF synthesis enigma

The bottom-up syntheses of novel nanomaterials for all kinds of applications have boomed in the last couple of decades, especially for MOFs, which can be tailor-made into a nearly endless number of different types due to the vast amount of combinations of linker molecules and metal ions available. This can be both a blessing and a curse; while looking for the next best MOF for various applications to help improve the world, it is easy to forget to research the fundamentals around the syntheses and applications of the materials.

MOF-235(Fe) and MIL-101(Fe) are two chemically similar MOFs that have been intensely studied by materials scientists for many years and are possibly the most economically and environmentally friendly MOFs. Despite the attention they have received, there are many question marks around their formation during their solvothermal syntheses and their subsequent applications as adsorbents and catalysts. For one, both MOFs show remarkably different surface areas and diffraction patterns in literature, despite the authors using the same synthesis protocols. In addition, some studies using MOF-235 as an aqueous phase adsorbent present excellent adsorption capacities for adsorbates that are significantly larger than the hexagonal channels of MOF-235. There is also the question of whether the MOFs are chemically stable in water, which arguably is one of the most important properties of a material to be used in water.

In preparation of paper III, we tested the conventional synthesis route of MOF-235(Fe) a seemingly endless number of times, without being able to reproduce the obtained surface areas and XRD patterns of the source of the synthesis protocol. We purchased new reagents, tried using completely water-free solvents, performed the heat-treatment in different vessels, tried other temperatures, all without notable success. Instead of the one sharp diffraction peak at  $9.4^\circ$ , characteristic of MOF-235, several smaller and wider peaks in the  $5\text{-}6^\circ$  region and around  $9^\circ$  showed up in the XRD analyses. Finally, a MOF-235 product was obtained by increasing the DMF:ethanol solvent ratio from 1:1 to 3:1. By testing different Fe(III):TPA reagent ratios, we could also synthesize a pure MIL-101 product with a large surface area at lower temperatures than what previously has been done.

The *ex-situ* and *in-situ* X-ray analyses during the solvothermal synthesis of the MOFs revealed two things: (1) No simultaneous formation of both phases was occurring, and (2) pausing the heat treatment and opening the synthesis vessel promoted MIL-101 formation. However, the XRD and surface area results show that both MOF-235 and MIL-101 can be present in the same sample when performing the conventional solvothermal synthesis in batches of 45-60 mL. The *in-situ* syntheses were done in narrow glass capillaries with room for less than 0.1 mL of reagent

solution, while the *ex-situ* syntheses were done in glass bottles containing 150 mL of solution. There is the possibility that the volume of reagent solution affects the formation of the MOFs since the mixed phase product was only found in the intermediate synthesis volumes. Another factor could be the type of synthesis vessel, as the intermediate volume synthesis was performed in stainless steel PTFE autoclaves with significantly thicker outer walls than both the other synthesis vessels. The vessels' wall thickness and material affect the heat transfer into the solution, which could be considered a key factor due to the need for heat to decompose the DMF and subsequently deprotonate the TPA linkers. Another role of the temperature is to stir the solution by Brownian motion by diffusion, a property directly dependent on T.

Since MOF-235 is the primary product at lower synthesis temperatures according to the *in-situ* syntheses, it is implied that it is the kinetic product, i.e., the fastest forming phase. Somehow, the thermodynamic product, MIL-101, can be formed at conditions at which MOF-235 usually is formed. Further studies, e.g. *in-situ* synchrotron SAXS analyses during the MOF formation, providing better time-resolutions and signal-to-noise ratios, could give more detailed information on the crystallization process at different conditions.

It can be debated whether MOF-235(Fe) and MIL-101(Fe) are suitable for aqueous phase adsorption. Despite that they both show excellent dye adsorption properties (Paper II), they both start to dissolve almost immediately when dispersed in water (Paper III). More extensive studies are required to determine the dissolution rate of the frameworks and the implication on the porosity and biocompatibility before they can be judged safe for usage in aqueous applications.

# Acknowledgements

It is safe to say that I would not be here if it were not for my supervisor, Zareen Abbas. I started my journey in his group in 2016, when I did my Bachelor's project, and I truly felt welcome from the first day. Besides being an outstanding researcher, he is also a phenomenal person, and I am endlessly thankful for having him as my supervisor and friend. Thank you for always showing support and giving me free reins to follow my instincts, grow, and learn from my mistakes.

I would also like to thank my Ph.D. examiner Professor Leif Eriksson, my Licentiate opponent Professor Gunnar Westman, and my Ph.D. opponent Professor Vadim Kessler from the Swedish University of Agricultural Sciences for taking their time to help me on my journey towards being a Dr. Many thanks to the other members of the grading committee: Professor Julianne M. Gibbs from the University of Alberta, Professor Niklas Hedin from Stockholm University, Associate Professor Romain Bordes from Chalmers University of Technology, and Professor Gergely Katona from the University of Gothenburg.

For the fruitful collaborations on several of the papers included in my thesis work, I would like to thank Mark Rambaran from Umeå University and Eric Tam, Amit Kumar Sonker, and Gunnar Westman from Chalmers University of Technology. In addition, I would like to thank the following people for the help with various instruments and analyses: Michal Strach, Stefan Gustafsson, Anne Wendel, Andreas Schäfer, and Stellan Holgersson.

The support from the staff and students at the University of Gothenburg, both in the form of friends and colleagues, has doubtlessly contributed to keeping my sanity and well-being intact during these five years. I want to give a special thanks to my fellow Ph.D. colleague and silica enjoyer, Christian Sögaard. An honorable mention to the other current and former members of the Electrochemistry Group: Adriano Gomes, Gert Göransson, Elisabet Ahlberg, Patrik Larses, Alberto Visibile, Krzysztof Kolman, Cedrik Wiberg, Khalid Elamin, Moira Andrén, Andy Waterbury, Prasad Rama, Alice Kent, Anna Stedt, and Julian Scheer. Non-members, but not any less important, include Jürgen Gräfenstein, Anders Lennartsson, Camilla Forsman, and Dasha Jones.

**These five years certainly flew by, all thanks to you all!**

# Bibliography

- [1] Gunnar Hall, Susanne Alenljung, and Ulla Forsgren-Brusk. “Identification of key odorants in used disposable absorbent incontinence products”. In: *Journal of Wound, Ostomy, and Continence Nursing* 44.3 (2017), p. 269.
- [2] Irving Langmuir. “The adsorption of gases on plane surfaces of glass, mica and platinum.” In: *Journal of the American Chemical Society* 40.9 (1918), pp. 1361–1403.
- [3] Robert J Hunter. *Zeta potential in colloid science: principles and applications*. Vol. 2. Academic press, 2013.
- [4] John C Berg. *An introduction to interfaces & colloids: The bridge to nanoscience*. World Scientific, 2010.
- [5] Franz Hofmeister. “About the science of the effects of salts: About the water withdrawing effect of the salts”. In: *Arch. Exp. Pathol. Pharmacol.* 24 (1888), pp. 247–260.
- [6] Zareen Abbas, Elisabet Ahlberg, and Sture Nordholm. “Monte Carlo simulations of salt solutions: exploring the validity of primitive models”. In: *The Journal of Physical Chemistry B* 113.17 (2009), pp. 5905–5916.
- [7] Manuel Quesada-Pérez et al. “Overcharging in colloids: beyond the Poisson–Boltzmann approach”. In: *ChemPhysChem* 4.3 (2003), pp. 234–248.
- [8] Johannes Lützenkirchen et al. “Potentiometric titrations as a tool for surface charge determination”. In: *Croatica chemica acta* 85.4 (2012), pp. 391–417.
- [9] Ann-Cathrin JH Johnsson, M Caterina Camerani, and Zareen Abbas. “Combined electrospray-SMPS and SR-SAXS investigation of colloidal silica aggregation. Part I. Influence of starting material on gel morphology”. In: *The Journal of Physical Chemistry B* 115.5 (2011), pp. 765–775.
- [10] Yizhak Marcus. “Effect of ions on the structure of water: structure making and breaking”. In: *Chemical reviews* 109.3 (2009), pp. 1346–1370.
- [11] Grinnell Jones and Malcolm Dole. “The viscosity of aqueous solutions of strong electrolytes with special reference to barium chloride”. In: *Journal of the American Chemical Society* 51.10 (1929), pp. 2950–2964.

- [12] WM Cox and JH Wolfenden. “The viscosity of strong electrolytes measured by a differential method”. In: *Proceedings of the Royal Society of London. Series A, Containing Papers of a Mathematical and Physical Character* 145.855 (1934), pp. 475–488.
- [13] Ronald Wilfrid Gurney and Ronald W Gurney. *Ionic processes in solution*. Vol. 5. McGraw-Hill New York, 1953.
- [14] Richard Buchner. “What can be learnt from dielectric relaxation spectroscopy about ion solvation and association?” In: *Pure and Applied Chemistry* 80.6 (2008), pp. 1239–1252.
- [15] Yizhak Marcus and Glenn Hefter. “Ion pairing”. In: *Chemical reviews* 106.11 (2006), pp. 4585–4621.
- [16] Robert A Robinson and Donald A Sinclair. “The activity coefficients of the alkali chlorides and of lithium iodide in aqueous solution from vapor pressure measurements”. In: *Journal of the American Chemical Society* 56.9 (1934), pp. 1830–1835.
- [17] Zareen Abbas and Elisabet Ahlberg. “Activity Coefficients of Concentrated Salt Solutions: A Monte Carlo Investigation”. In: *Journal of Solution Chemistry* 48.8-9 (2019), pp. 1222–1243.
- [18] Isabelle Simonsson et al. “The specific co-ion effect on gelling and surface charging of silica nanoparticles: Speculation or reality?” In: *Colloids and Surfaces A: Physicochemical and Engineering Aspects* 559 (2018), pp. 334–341.
- [19] Ram M Adar, Tomer Markovich, and David Andelman. “Bjerrum pairs in ionic solutions: A Poisson-Boltzmann approach”. In: *The Journal of Chemical Physics* 146.19 (2017), p. 194904.
- [20] Douglas M Ruthven. *Principles of adsorption and adsorption processes*. John Wiley & Sons, 1984.
- [21] Robert J Hunter. *Foundations of colloid science*. Oxford university press, 2001.
- [22] H Freundlich and HS Hatfield. “Colloid and capillary chemistry, Methuen and Co”. In: *Ltd., London* (1926), pp. 110–114.
- [23] Fumiaki Kano et al. “Fractal model for adsorption on activated carbon surfaces: Langmuir and Freundlich adsorption”. In: *Surface Science* 467.1-3 (2000), pp. 131–138.
- [24] Arthur W Adamson, Alice Petry Gast, et al. *Physical chemistry of surfaces*. Vol. 150. Interscience publishers New York, 1967.

- [25] Marek Kosmulski. “Isoelectric points and points of zero charge of metal (hydr)oxides: 50 years after Parks’ review”. In: *Advances in Colloid and Interface Science* 238 (2016), pp. 1–61.
- [26] Borislav Zdravkov et al. “Pore classification in the characterization of porous materials: A perspective”. In: *Open Chemistry* 5.2 (2007), pp. 385–395.
- [27] Hailian Li et al. “Design and synthesis of an exceptionally stable and highly porous metal-organic framework”. In: *Nature* 402.6759 (1999), pp. 276–279.
- [28] Maria Kathrina B Gratio et al. “Production of activated carbon from coconut shell: Optimization using response surface methodology”. In: *Biore-source Technology* 99.11 (2008), pp. 4887–4895.
- [29] C Srinivasakannan and Mohamad Zailani Abu Bakar. “Production of activated carbon from rubber wood sawdust”. In: *Biomass and Bioenergy* 27.1 (2004), pp. 89–96.
- [30] Jianfeng Ma et al. “Adsorption of methylene blue and Orange II pollutants on activated carbon prepared from banana peel”. In: *Journal of Porous Materials* 22.2 (2015), pp. 301–311.
- [31] Nasrin R Khalili et al. “Production of micro-and mesoporous activated carbon from paper mill sludge: I. Effect of zinc chloride activation”. In: *Carbon* 38.14 (2000), pp. 1905–1915.
- [32] Tamer M Alslaibi et al. “A review: production of activated carbon from agricultural byproducts via conventional and microwave heating”. In: *Journal of Chemical Technology & Biotechnology* 88.7 (2013), pp. 1183–1190.
- [33] Hanns Peter Boehm. “Surface oxides on carbon and their analysis: a critical assessment”. In: *Carbon* 40.2 (2002), pp. 145–149.
- [34] Song-Woo Lee, Wan Mohd Ashri Wan Daud, and Min-Gyu Lee. “Adsorption characteristics of methyl mercaptan, dimethyl disulfide, and trimethylamine on coconut-based activated carbons modified with acid and base”. In: *Journal of Industrial and Engineering Chemistry* 16.6 (2010), pp. 973–977.
- [35] Ljubisa R Radovic. “Adsorption of organics from aqueous solution on surface-modified active carbons: A critical review”. In: *Tanso* 1998.185 (1998), pp. 326–331.
- [36] C Casagrande et al. ““Janus beads”: realization and behaviour at water/oil interfaces”. In: *EPL (Europhysics Letters)* 9.3 (1989), p. 251.
- [37] Da Hee Kang et al. “Anatase TiO<sub>2</sub>-doped activated carbon fibers prepared by ultrasonication and their capacitive deionization characteristics”. In: *Carbon letters* 27 (2018), pp. 64–71.

- [38] Yanhui Ao et al. “Low temperature preparation of anatase TiO<sub>2</sub>-coated activated carbon”. In: *Colloids and Surfaces A: Physicochemical and Engineering Aspects* 312.2-3 (2008), pp. 125–130.
- [39] Jian-Rong Li et al. “Selective Gas Adsorption and Unique Structural Topology of a Highly Stable Guest-Free Zeolite-Type MOF Material with N-rich Chiral Open Channels”. In: *Chemistry-A European Journal* 14.9 (2008), pp. 2771–2776.
- [40] Andrea C Sudik, Adrien P Côté, and Omar M Yaghi. “Metal-organic frameworks based on trigonal prismatic building blocks and the new acs topology”. In: *Inorganic chemistry* 44.9 (2005), pp. 2998–3000.
- [41] Yingjie Li et al. “Facile synthesis of MOF 235 and its superior photocatalytic capability under visible light irradiation”. In: *RSC Advances* 6.20 (2016), pp. 16395–16403.
- [42] Enamul Haque, Jong Won Jun, and Sung Hwa Jung. “Adsorptive removal of methyl orange and methylene blue from aqueous solution with a metal-organic framework material, iron terephthalate (MOF-235)”. In: *Journal of Hazardous materials* 185.1 (2011), pp. 507–511.
- [43] Isabelle Simonsson et al. “Experimental investigations into the irregular synthesis of iron(iii) terephthalate metal-organic frameworks MOF-235 and MIL-101”. In: *Dalton Transactions* 50.14 (2021), pp. 4976–4985.
- [44] YF Chen et al. “Metal-organic framework MIL-101 for adsorption and effect of terminal water molecules: from quantum mechanics to molecular simulation”. In: *Langmuir* 26.11 (2010), pp. 8743–8750.
- [45] Jia Tang et al. “Heterogeneous Fe-MIL-101 catalysts for efficient one-pot four-component coupling synthesis of highly substituted pyrroles”. In: *New Journal of Chemistry* 39.6 (2015), pp. 4919–4923.
- [46] OI Lebedev et al. “First direct imaging of giant pores of the metal-organic framework MIL-101”. In: *Chemistry of materials* 17.26 (2005), pp. 6525–6527.
- [47] André DS Barbosa et al. “Catalytic performance and electrochemical behaviour of Metal-organic frameworks: MIL-101 (Fe) versus NH<sub>2</sub>-MIL-101 (Fe)”. In: *Polyhedron* 127 (2017), pp. 464–470.
- [48] Ronald L Crawford et al. *Lignin biodegradation and transformation*. John Wiley and Sons., 1981.

- [49] H Staudinger. “Viscosity investigations for the examination of the constitution of natural products of high molecular weight and of rubber and cellulose”. In: *Transactions of the Faraday Society* 29.140 (1933), pp. 18–32.
- [50] Albin F Turbak, Fred W Snyder, Karen R Sandberg, et al. “Microfibrillated cellulose, a new cellulose product: properties, uses, and commercial potential”. In: *J Appl Polym Sci Appl Polym Symp*. Vol. 37. 9. 1983, pp. 815–827.
- [51] Dieter Klemm et al. “Nanocelluloses: a new family of nature-based materials”. In: *Angewandte Chemie International Edition* 50.24 (2011), pp. 5438–5466.
- [52] Krzysztof Kolman et al. “Combined nanocellulose/nanosilica approach for multiscale consolidation of painting canvases”. In: *ACS Applied Nano Materials* 1.5 (2018), pp. 2036–2040.
- [53] Zhijun Shi, Glyn O Phillips, and Guang Yang. “Nanocellulose electroconductive composites”. In: *Nanoscale* 5.8 (2013), pp. 3194–3201.
- [54] Narges Naseri et al. “Nanocellulose-based interpenetrating polymer network (IPN) hydrogels for cartilage applications”. In: *Biomacromolecules* 17.11 (2016), pp. 3714–3723.
- [55] Chunlin Xu et al. “3D printing of nanocellulose hydrogel scaffolds with tunable mechanical strength towards wound healing application”. In: *Journal of Materials Chemistry B* 6.43 (2018), pp. 7066–7075.
- [56] Liangbing Hu et al. “Transparent and conductive paper from nanocellulose fibers”. In: *Energy & Environmental Science* 6.2 (2013), pp. 513–518.
- [57] Reza Iranpour et al. “Literature review of air pollution control biofilters and biotrickling filters for odor and volatile organic compound removal”. In: *Environmental Progress* 24.3 (2005), pp. 254–267.
- [58] Yong-Chao Wang et al. “Emissions, measurement, and control of odor in livestock farms: A review”. In: *Science of The Total Environment* 776 (2021), p. 145735.
- [59] Yoshio Nagata, N Takeuchi, et al. “Measurement of odor threshold by triangle odor bag method”. In: *Odor measurement review* 118 (2003), pp. 118–127.
- [60] Hajime Tamon and Morio Okazaki. “Desorption characteristics of aromatic compounds in aqueous solution on solid adsorbents”. In: *Journal of colloid and interface science* 179.1 (1996), pp. 181–187.
- [61] Souhaila Bouatra et al. “The human urine metabolome”. In: *PloS one* 8.9 (2013), e73076.

- [62] Neslihan Sarigul, Filiz Korkmaz, and İlhan Kurultak. “A new artificial urine protocol to better imitate human urine”. In: *Scientific reports* 9.1 (2019), pp. 1–11.
- [63] Hannah Ray, Daniella Saetta, and Treavor H Boyer. “Characterization of urea hydrolysis in fresh human urine and inhibition by chemical addition”. In: *Environmental Science: Water Research & Technology* 4.1 (2018), pp. 87–98.
- [64] Karthik R Peddireddy et al. “Stabilization of water-in-water emulsions by nanorods”. In: *ACS Macro Letters* 5.3 (2016), pp. 283–286.
- [65] Aref Abbasi Moud et al. “Colloidal behavior of cellulose nanocrystals in presence of sodium chloride”. In: *ChemistrySelect* 3.17 (2018), pp. 4969–4978.
- [66] Huixiao Duo et al. “Synthesis of magnetic metal–organic framework composites, Fe<sub>3</sub>O<sub>4</sub>-NH<sub>2</sub>@ MOF-235, for the magnetic solid-phase extraction of benzoylurea insecticides from honey, fruit juice and tap water samples”. In: *New Journal of Chemistry* 43.32 (2019), pp. 12563–12569.
- [67] Mansoor Anbia, Vahid Hoseini, and Sara Sheykhi. “Sorption of methane, hydrogen and carbon dioxide on metal-organic framework, iron terephthalate (MOF-235)”. In: *Journal of Industrial and Engineering Chemistry* 18.3 (2012), pp. 1149–1152.
- [68] Thuan D Le et al. “1, 5-Benzodiazepine synthesis via cyclocondensation of 1, 2-diamines with ketones using iron-based metal–organic framework MOF-235 as an efficient heterogeneous catalyst”. In: *Journal of catalysis* 333 (2016), pp. 94–101.
- [69] Caroline De Smedt et al. “Comparison of different solid adsorbents for the removal of mobile pesticides from aqueous solutions”. In: *Adsorption* 21.3 (2015), pp. 243–254.
- [70] Saihua Wang et al. “Rapid determination of small molecule pollutants using metal-organic frameworks as adsorbent and matrix of MALDI-TOF-MS”. In: *Microporous and Mesoporous Materials* 239 (2017), pp. 390–395.
- [71] Utku Bulut Simsek, Cihan Gecgel, and Meral Turabik. “Different Iron Based Metal Organic Frameworks Synthesis, Characterization and Using for Amoxicillin Removal from Aqueous Solutions”. In: ().
- [72] Jinlong Ge et al. “An Effective Microwave-Assisted Synthesis of MOF235 with Excellent Adsorption of Acid Chrome Blue K”. In: *Journal of Nanomaterials* 2019 (2019).

- [73] Kathryn ML Taylor-Pashow et al. "Postsynthetic modifications of iron carboxylate nanoscale metal-organic frameworks for imaging and drug delivery". In: *Journal of the American Chemical Society* 131.40 (2009), pp. 14261–14263.
- [74] Nataliya V Maksimchuk et al. "Cyclohexane selective oxidation over metal-organic frameworks of MIL-101 family: superior catalytic activity and selectivity". In: *Chemical Communications* 48.54 (2012), pp. 6812–6814.
- [75] Bin Wu et al. "A novel route for preparing highly proton conductive membrane materials with metal-organic frameworks". In: *Chemical Communications* 49.2 (2013), pp. 143–145.
- [76] Qiyang Xie et al. "Effective adsorption and removal of phosphate from aqueous solutions and eutrophic water by Fe-based MOFs of MIL-101". In: *Scientific reports* 7.1 (2017), pp. 1–15.
- [77] Lei He et al. "A novel magnetic MIL-101 (Fe)/TiO<sub>2</sub> composite for photo degradation of tetracycline under solar light". In: *Journal of hazardous materials* 361 (2019), pp. 85–94.
- [78] Cihan Gecgel et al. "Comparison of MIL-101 (Fe) and amine-functionalized MIL-101 (Fe) as photocatalysts for the removal of imidacloprid in aqueous solution". In: *Journal of the Iranian Chemical Society* 16.8 (2019), pp. 1735–1748.
- [79] Zongchen Li et al. "Adsorption behavior of arsenicals on MIL-101 (Fe): the role of arsenic chemical structures". In: *Journal of colloid and interface science* 554 (2019), pp. 692–704.
- [80] Joong S Noh and James A Schwarz. "Effect of HNO<sub>3</sub> treatment on the surface acidity of activated carbons". In: *Carbon* 28.5 (1990), pp. 675–682.
- [81] J L Figueiredo et al. "Modification of the surface chemistry of activated carbons". In: *carbon* 37.9 (1999), pp. 1379–1389.
- [82] A van Bondi. "van der Waals volumes and radii". In: *The Journal of physical chemistry* 68.3 (1964), pp. 441–451.
- [83] Stephen Brunauer, Paul Hugh Emmett, and Edward Teller. "Adsorption of gases in multimolecular layers". In: *Journal of the American chemical society* 60.2 (1938), pp. 309–319.
- [84] Elliott P Barrett, Leslie G Joyner, and Paul P Halenda. "The determination of pore volume and area distributions in porous substances. I. Computations from nitrogen isotherms". In: *Journal of the American Chemical society* 73.1 (1951), pp. 373–380.

- [85] JH De Boer et al. “The t-curve of multimolecular N<sub>2</sub>-adsorption”. In: *Journal of Colloid and Interface Science* 21.4 (1966), pp. 405–414.
- [86] George Jura and William D Harkins. “Surfaces of Solids. XI. Determination of the decrease ( $\pi$ ) of free surface energy of a solid by an adsorbed film”. In: *Journal of the American Chemical Society* 66.8 (1944), pp. 1356–1362.
- [87] Anne Galarneau et al. “Validity of the t-plot method to assess microporosity in hierarchical micro/mesoporous materials”. In: *Langmuir* 30.44 (2014), pp. 13266–13274.
- [88] Mark Weller et al. *Inorganic chemistry*. Oxford University Press, USA, 2014.
- [89] Burkhard Beckhoff et al. *Handbook of practical X-ray fluorescence analysis*. Springer Science & Business Media, 2007.
- [90] Kai Siegbahn et al. “Angular distribution of electrons in ESCA spectra from a single crystal”. In: *Physica Scripta* 1.5-6 (1970), p. 272.
- [91] Kai Siegbahn. “Electron spectroscopy for atoms, molecules, and condensed matter”. In: *Reviews of Modern Physics* 54.3 (1982), p. 709.
- [92] CS Fadley and DA Shirley. “Electronic densities of states from X-ray photoelectron spectroscopy”. In: *Journal of Research of the National Bureau of Standards. Section A, Physics and Chemistry* 74.4 (1970), p. 543.
- [93] Hiroyuki Ohshima. “A simple expression for Henry’s function for the retardation effect in electrophoresis of spherical colloidal particles”. In: *Journal of Colloid and Interface Science* 168.1 (1994), pp. 269–271.
- [94] Thomas J Manning and William R Grow. “Inductively coupled plasma-atomic emission spectrometry”. In: *The chemical educator* 2.1 (1997), pp. 1–19.
- [95] Ian T Joliffe and BJT Morgan. “Principal component analysis and exploratory factor analysis”. In: *Statistical methods in medical research* 1.1 (1992), pp. 69–95.
- [96] OriginLab Corporation. *OriginPro*. 2021.
- [97] CP Lawrence and JL Skinner. “Flexible TIP4P model for molecular dynamics simulation of liquid water”. In: *Chemical physics letters* 372.5-6 (2003), pp. 842–847.
- [98] Henk Bekker et al. “Gromacs-a parallel computer for molecular-dynamics simulations”. In: *4th International Conference on Computational Physics (PC 92)*. World Scientific Publishing. 1993, pp. 252–256.

- [99] Bernard R Brooks et al. "CHARMM: a program for macromolecular energy, minimization, and dynamics calculations". In: *Journal of computational chemistry* 4.2 (1983), pp. 187–217.
- [100] Seonghoon Kim et al. *CHARMM-GUI ligand reader and modeler for CHARMM force field generation of small molecules*. 2017.
- [101] Sunhwan Jo et al. "CHARMM-GUI: a web-based graphical user interface for CHARMM". In: *Journal of computational chemistry* 29.11 (2008), pp. 1859–1865.
- [102] Walter J Hamer and Yung-Chi Wu. "Osmotic coefficients and mean activity coefficients of uni-univalent electrolytes in water at 25° C". In: *Journal of Physical and Chemical Reference Data* 1.4 (1972), pp. 1047–1100.
- [103] Robert N Goldberg. "Evaluated activity and osmotic coefficients for aqueous solutions: thirty-six uni-bivalent electrolytes". In: *Journal of Physical and Chemical Reference Data* 10.3 (1981), pp. 671–764.
- [104] Koichi Momma and Fujio Izumi. "VESTA 3 for three-dimensional visualization of crystal, volumetric and morphology data". In: *Journal of applied crystallography* 44.6 (2011), pp. 1272–1276.
- [105] John A Marsella and Updated by Staff. "Dimethylformamide". In: *Kirk-Othmer Encyclopedia of Chemical Technology* (2000), pp. 1–9.
- [106] William M Haynes, David R Lide, and Thomas J Bruno. *CRC handbook of chemistry and physics*. CRC press, 2016.
- [107] Jan Gustafsson et al. "The influence of pH and NaCl on the Zeta potential and rheology of anatase dispersions". In: *Colloids and Surfaces A: Physico-chemical and Engineering Aspects* 175.3 (2000), pp. 349–359.
- [108] V Bolis et al. "Hydrophilic/hydrophobic features of TiO<sub>2</sub> nanoparticles as a function of crystal phase, surface area and coating, in relation to their potential toxicity in peripheral nervous system". In: *Journal of colloid and interface science* 369.1 (2012), pp. 28–39.
- [109] Kheamrutai Thamaphat, Pichet Limsuwan, and Boonlaer Ngotawornchai. "Phase characterization of TiO<sub>2</sub> powder by XRD and TEM". In: *Agriculture and Natural Resources* 42.5 (2008), pp. 357–361.
- [110] Gianluca Li Puma et al. "Preparation of titanium dioxide photocatalyst loaded onto activated carbon support using chemical vapor deposition: a review paper". In: *Journal of hazardous Materials* 157.2-3 (2008), pp. 209–219.

- [111] A Contescu et al. “Surface acidity of carbons characterized by their continuous pK distribution and Boehm titration”. In: *Carbon* 35.1 (1997), pp. 83–94.
- [112] Andrew Turner and M Carl Rawling. “The influence of salting out on the sorption of neutral organic compounds in estuaries”. In: *Water research* 35.18 (2001), pp. 4379–4389.
- [113] JC Means. “Influence of salinity upon sediment-water partitioning of aromatic hydrocarbons”. In: *Marine Chemistry* 51.1 (1995), pp. 3–16.
- [114] Ruey-Shin Juang, Wen-Ching Huang, and Ya-Han Hsu. “Treatment of phenol in synthetic saline wastewater by solvent extraction and two-phase membrane biodegradation”. In: *Journal of hazardous materials* 164.1 (2009), pp. 46–52.
- [115] LT Bugaenko, SM Ryabykh, and AL Bugaenko. “A nearly complete system of average crystallographic ionic radii and its use for determining ionization potentials”. In: *Moscow University Chemistry Bulletin* 63.6 (2008), pp. 303–317.
- [116] Mikaela Börjesson et al. “Increased thermal stability of nanocellulose composites by functionalization of the sulfate groups on cellulose nanocrystals with azetidinium ions”. In: *Journal of Applied Polymer Science* 135.10 (2018), p. 45963.
- [117] Neng Wang, Enyong Ding, and Rongshi Cheng. “Thermal degradation behaviors of spherical cellulose nanocrystals with sulfate groups”. In: *Polymer* 48.12 (2007), pp. 3486–3493.
- [118] Christian Sögaard et al. “Hofmeister effects in the gelling of silica nanoparticles in mixed salt solutions”. In: *Colloids and Surfaces A: Physicochemical and Engineering Aspects* 611 (2021), p. 125872.
- [119] Kim D Collins. “Charge density-dependent strength of hydration and biological structure”. In: *Biophysical journal* 72.1 (1997), pp. 65–76.
- [120] Adrien Sthoer et al. “Molecular insight into carboxylic acid–alkali metal cations interactions: Reversed affinities and ion-pair formation revealed by non-linear optics and simulations”. In: *Physical Chemistry Chemical Physics* 21.21 (2019), pp. 11329–11344.
- [121] Jonas Björk et al. “Adsorption of aromatic and anti-aromatic systems on graphene through  $\pi$ - $\pi$  stacking”. In: *The Journal of Physical Chemistry Letters* 1.23 (2010), pp. 3407–3412.

- [122] Jun Wang, Zaiming Chen, and Baoliang Chen. “Adsorption of polycyclic aromatic hydrocarbons by graphene and graphene oxide nanosheets”. In: *Environmental science & technology* 48.9 (2014), pp. 4817–4825.
- [123] TS Sreeprasad and Vikas Berry. “How do the electrical properties of graphene change with its functionalization?” In: *small* 9.3 (2013), pp. 341–350.
- [124] Ajay Jha et al. “Reduced graphene oxide composite with oxidizable manganese/cobalt mixed oxide for p-cresol oxidation by using molecular oxygen”. In: *ChemPlusChem* 80.7 (2015), pp. 1164–1169.
- [125] Linda J Johnston et al. “Determination of sulfur and sulfate half-ester content in cellulose nanocrystals: An interlaboratory comparison”. In: *Metrologia* 55.6 (2018), p. 872.
- [126] Jun Araki et al. “Influence of surface charge on viscosity behavior of cellulose microcrystal suspension”. In: *Journal of wood science* 45.3 (1999), pp. 258–261.
- [127] Hayaka Fukuzumi et al. “Dispersion stability and aggregation behavior of TEMPO-oxidized cellulose nanofibrils in water as a function of salt addition”. In: *Cellulose* 21.3 (2014), pp. 1553–1559.
- [128] Stanka Kratochvil, Gilbert E Janauer, and Egon Matijević. “Coagulation of microcrystalline cellulose dispersions”. In: *Journal of colloid and interface science* 29.2 (1969), pp. 187–193.